Effects of Surface Condition on the Corrosion Performance of Stainless Steel Rebar

By

Bradley P. Bergsma

A thesis
presented to the University of Waterloo
in fulfilment of the
thesis requirement for the degree of
Master of Applied Science
in
Mechanical Engineering

Waterloo, Ontario, Canada, 2009

I hereby declare that I am the sole author of this thesis. This is a true copy of the thesis, including any required final revisions, as accepted by my examiners.

I understand that my thesis may be made electronically available to the public.

Bradley P. Bergsma

Abstract

Corrosion of carbon (black) steel reinforcing bars (rebar) is the major cause of damage and deterioration of reinforced concrete structures in maritime regions and in climates where de-icing salts are used. The cause of the corrosion is diffusion of chloride ions to the steel surface through the concrete in which it is placed. The bars are naturally passivated by the high pH of concrete interstitial pore fluid, and will not corrode in chloride-free concrete. Chloride ions break down the passive film, allowing dissolution of the steel. Corrosion of reinforcing steel drastically reduces the service lives of concrete structures.

Where chlorides can not be avoided, stainless steel is becoming increasingly popular as an alternative reinforcing material. Stainless steel is able to withstand greater concentrations of chlorides, extending the service lives of structure in which they are placed. Due to high initial cost, stainless steel is often avoided in the design of new structures. In order to reduce the cost of stainless rebar, it has been proposed that the standard process of abrasive blasting and pickling of the steels not be performed, as these steps are mainly used to restore a bright and shiny surface, a quality not required for steels embedded in concrete.

AISI 304LN, AISI 316LN and 2205 duplex stainless steels were tested with pickled surfaces as well as with mill-scale intact (as-rolled) in order to determine the affect of pickling vs. not pickling on the corrosion behaviour of the steels. Steels were tested in solutions simulating concrete interstitial pore fluid containing from 0 to 16% Cl^- by mass of solution, simulating cement paste with 0 to 7.5% Cl^- by mass of cement, which is near the solubility limit of Cl^- in pore fluid. Steels were also tested in thin mortar shells, with Cl^- ions being rapidly diffused to the surface due to an applied potential gradient.

The microcell corrosion performance of the as-rolled steels was slightly worse than that of pickled steels; however, the corrosion rates of the as-rolled steels at 16% Cl^- in pore fluid are near 3 μm/year, while black steel is normally observed to be actively corroding at 10 μm/year in cement containing as low as 0.1% Cl^- by mass of cement, or 0.2% Cl^- by mass of solution.

No significant difference was observed between different grades of stainless steel in either the as-rolled or pickled conditions.

As-rolled stainless steels exhibited poor pitting resistance when an anodic potential is applied, but the corrosion occurs at potentials much higher than experienced in service and at Cl^- concentrations far greater than that needed to initiate corrosion on black steel; the time required to reach these higher Cl^- levels would allow for maintenance free service long enough to justify the cost of as-rolled stainless steel over black steel.

The Canadian Highway Bridge Design Code, CSA S6-06, specifies that reinforced concrete bridges should meet a service life of 75 years. It is concluded that, given the time required for concentrated chlorides to accumulate at the steel, the stainless steel rebar in the as-rolled condition would allow reinforced concrete structures to reach the specified service life, as long as care is taken to avoid contamination of the steel/surface by black steel from handling, or by secondary phases within the steel, $Cr_{23}C_6$ and MnS in particular.

Acknowledgements

I would like to express my immeasurable appreciation to my supervisor, Dr. Carolyn Hansson, for allowing me the honour of working with her, and for her invaluable guidance, support, and patience throughout the course of this research project and in completing this dissertation. She showed unwavering interest both in the research at hand and my success within and outside of the academic domain, and provided an example of what I aspire to be in both my professional and personal life.

This project would not have been possible without the help of my colleagues and friends; Dr. Laura Mammoliti, Dr. Amir Poursaee, Dr. Shahzma Jaffer, Ramtin Movassaghi, Khanh Tran, Irene Wijoyo, Quan Tan, Kyle Anders, Ken Su, and Katherine Olsen. I would like to give special thanks to Dr. Amir Poursaee and Dr. Shahzma Jaffer for their invaluable assistance with operating the electrical equipment used in this project and understanding the electrochemical interactions which they involve.

I would like to thank Dr. Xiaogang Li from the Department of Mechanical and Mechatronics Engineering for his assistance with powder x-ray diffraction analysis. I also appreciate the efforts of Norval Wilhelm and John Potzold for their assistance in the design and preparation of test specimens, and Dr. Yuquan Ding for his assistance with optical and scanning electron microscopy.

Thanks also to the Ministry of Transportation of Ontario, the Nickel Institute and Valbruna Canada for providing their financial support and test materials.

I would also like to thank Dr. Mary Wells and Dr. Steve Lambert for their time and effort in reading and critiquing my thesis and seminar.

Finally, I would like to thank my parents, who endured this long process with me, giving me strength and financial assistance when I needed it. Lastly, I truly and especially appreciate the phenomenal patience and dedication of my partner Lisa, for bearing with me through the stress and frustration, and for supporting me when my own confidence was failing me.

Table of Contents

List of Figures

List of Tables

1 Introduction

In our ever expanding network of infrastructure, there are more and more steel reinforced concrete structures being used. These include critical structures such as bridges, highway overpasses and highway safety barrier walls, which can be difficult, dangerous and inconvenient to service. It is desirable to achieve long service lives of these structures, so concrete is a reasonable choice, being very strong (in compression) and highly durable; however, many bridges and overpasses fail to meet the 75 year service live specified in the Canadian Highway Bridge Design Code, or require extensive amounts of maintenance and repair in order to meet it. The predominant cause of damage is corrosion of the steel reinforcing due to chlorides from de-icing salt or maritime environments.

1.1 Traditional Steel Reinforced Concrete Structures

Typical reinforced concrete structures contain carbon (black) steel reinforcing bar (rebar) in Ordinary Portland Cement (OPC) concrete. Concrete protects the rebar from corrosion in two ways: the thickness of concrete between the steel and the atmosphere (the concrete cover) provides a physical barrier from the environment, and cement paste pore solution has a very high pH, which passivates the iron, suppressing dissolution.

Hydrated OPC is a mixture of porous gel and crystalline phases as well as interstitial pore solution, the by-products of the reaction and hydration of the cement. The pore solution has a high concentration of OH^- ions, resulting in a pH of around 13.5 [1,2]. This pore solution is in direct contact with the reinforcing steel and its high pH passivates the steel.

The E/pH diagram for iron (Figure 1-1) at a pH of 13.5 indicates that the steel should be immune to corrosion at potentials below about -900 mV vs. a standard hydrogen electrode (SHE), and should form a protective passive film of Fe_3O_4 above about -875 mV vs. SHE, or Fe_2O_3 above about -635 mV vs. SHE. In sound concrete without chlorides present, the potential of steel rebar is about -100 mV vs. SHE, which is well into the passive region. Under these conditions the steel will still oxidize, but instead of simple dissolution at the surface, the iron reacts with water in several possible ways,

$$3Fe + 4H_2O \rightarrow Fe_3O_4 + 8H^+ + 8e^- \quad (1a)$$

$$2Fe + 3H_2O \rightarrow Fe_2O_3 + 6H^+ + 6e^- \quad (1b)$$

building up an oxide layer [2,3]. In this state corrosion is negligible and structures will sustain very little damage.

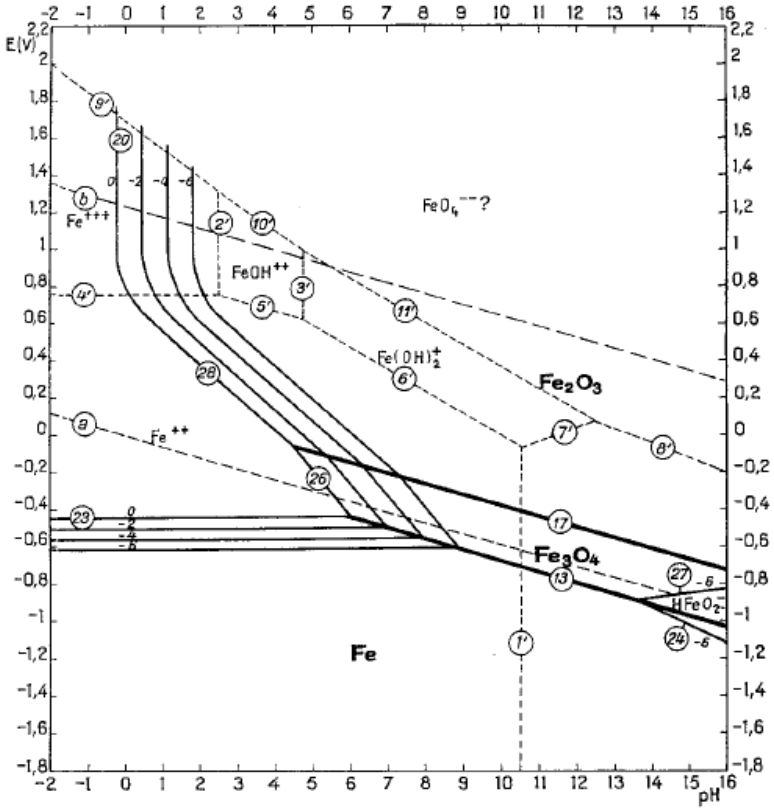

Figure 1-1: E/pH Diagram for Iron [4]

1.2 Deterioration of Reinforced Concrete Structures

A structure made with sound concrete can last centuries if the concrete is not subject to freeze-thaw damage or chemical attack of cement paste or aggregates and the steel remains passive. Freeze-thaw damage and chemical attack can be minimized or avoided by using an appropriately designed concrete. The steel remains passive until CO_2 reduces the pH of the concrete pore solution (a process known as carbonation), or until chloride ions reach the surface of the steel. Carbonation reduces the pore solution pH to near neutral levels, where iron is no longer passive; this attack on the concrete is generally very slow and is rarely the cause of damage in the Canadian climate.

In maritime regions with salt water, and northern climates where de-icing salts are used to clear paved roadways, chloride ions are readily available to diffuse into concrete structures. Chlorides can diffuse through the concrete cover to the reinforcing steel due to the porous structure of the cement paste, a process which is accelerated by the presence of cracks in the concrete and which can occur in less than a decade in some poorly designed or constructed structures. Poorly designed structures may allow slush or water runoff saturated with chlorides to pool and sit, allowing chloride ions to diffuse into the concrete more rapidly than it should. Poorly constructed structures could have problems such as exposed steel at expansion joints or inadequate concrete cover over the bars. Chloride ions locally disrupt the passive film on the steel, allowing the steel to corrode more rapidly. They also prevent the passive film from reforming, so corrosion may continue and more importantly, a pit may be initiated. The danger of pitting is that the corrosion is limited to a small area and will reduce the rebar cross-section much more quickly than general corrosion (corrosive attack of the whole surface at a uniform rate).

Corrosion of reinforcing steel is the most common cause of damage to these structures, as the destruction of the concrete cover usually follows. The corrosion products occupy a larger space than the original steel. Figure 1-2 shows Fe_2O_3 and Fe_3O_4 having a relative volume more than twice that of the base steel [5]. The corrosion products create tensile stresses within the concrete, which can eventually crack and spall the concrete cover over the rebar. Both the reduction in rebar cross-section and the cracking and loss of the concrete reduce the strength of the structure and its lifespan, often necessitating costly, inconvenient remediation and maintenance.

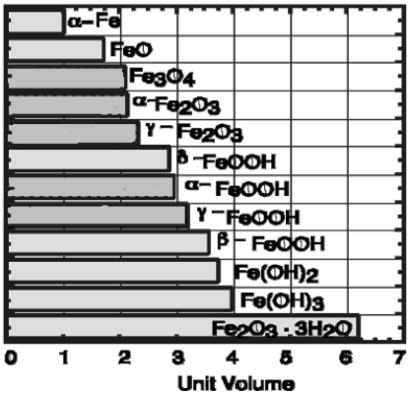

Figure 1-2: Relative volume of iron corrosion products [5]

1.3 Corrosion Resistant Reinforcing Bars

Alternatives to black steel reinforcement include galvanized and epoxy coated black steel, as well as advanced materials such as composites and stainless steels. The use of

zinc or epoxy to protect carbon steel reinforcement is beneficial in that they provide an extra barrier against chlorides and, in the case of galvanizing, a sacrificial anode [6]; however, these benefits may be negated by damage to or imperfections in the coating, and at best, simply delay the corrosion of the substrate steel. Epoxy also tends to absorb moisture and deteriorate, and may well be ineffective by the time chloride ions reach the rebar [7].

A more effective solution to the corrosion of rebar is the use of stainless steel instead of black steel. Although it is more expensive, stainless steel provides significantly superior resistance to corrosion, whether in carbonated concrete or in the presence of chlorides. The high chromium content of these steels causes a protective Cr_2O_3 film to form, which inhibits corrosion even though it is very thin [8].

The high initial cost of stainless rebar, or other corrosion resistant rebar types for that matter, is generally expected to be covered by a longer service life with reduced maintenance costs. Whether black steel, epoxy-coated black steel, galvanized steel or stainless steel rebar are used, corrosion is inevitable when sufficient amounts of chloride ions reach the steel. A much higher chloride threshold for the corrosion of stainless steel rebar compared to black steel suggests that in the time required for stainless steel to corrode, a structure built with black steel would require extensive maintenance and/or repairs, possibly even full replacement, more than accounting for initial cost of the stainless steel [9].

1.4 Use and Limitations of Stainless Steel Reinforcing

Evidence of the exceptional corrosion resistance of stainless steel rebar is available in a pier in Progresso, Mexico [10]. This pier was constructed in the late 1930s using AISI type 304 stainless steel. A neighbouring pier was constructed in the 1960s using plain carbon reinforcement. A 1999 inspection of the original pier revealed little or no deterioration of the structure after approximately 60 years, although it was emphasized that poor quality concrete was used. The warm climate and high salinity of seawater have destroyed the newer pier; the expansion of corroding black rebar resulted in the crumbling of its concrete pilings. The mere survival of the original pier is a testament to

the durability of the type 304 reinforcing, but the authors of the report project another 30 years of service.

The example of the pier in Progresso indicates a service life of around 90 years, but the success experienced in Mexico may not be replicated in Ontario. In northern climates, freeze-thaw damage can deteriorate concrete and de-icing salts can provide high chloride concentrations (up to 16% by weight in concrete interstitial pore solution), so poor quality concrete would not protect the steel as well as in Mexico, which rests in seawater, which typically has about 3.5% total salts by weight.

Type 304 stainless steel was used in several field trials beginning in the 1980s. An interstate highway bridge near Detroit was repaired using solid stainless bars for four lanes, while in 1983/84 in New Jersey, another interstate bridge was built using 304 stainless clad rebar [11]. High levels of chlorides, supplied through de-icing salts, caused black rebar in both locations to corrode. Cores taken from the bridges showed no corrosion of stainless rebar after nine years, although exposed black steel at the end of a clad bar did show minor corrosion.

The expected durability of high performance concrete (concrete with low water/cement ratio to give a very strong concrete with low porosity) would allow service lives exceeding 100 years if not for the corrosion of reinforcement. For example, along the US Pacific coast, carbon steel reinforced structures have experienced structural failure in as few as 17 years. Based on information available on the corrosion performance of stainless steel reinforcement, bridge designers are projecting impressive service lives of modern stainless reinforced structures; in the United States, bridge designers are currently projecting service lives of 100 to 120 years for structures using UNS S31803 (2205 duplex) in marine environments with increased seismic activity [12] or extreme traffic conditions [13]. A report by the US Federal Highway Administration in 1998 indicated that service lives of 75-100 years could be expected of structures using 316LN [9].

Stainless steel, although effective, is often too expensive to be justified in the initial costs for use in place of the other alternatives. The cost of stainless steel is high predominantly due to alloying elements used, but also due to post-rolling abrasive blasting and pickling.

The pickling step raises the cost of the steel significantly, as extensive measures must be taken for the safety of personnel and the environment when nitric and hydrofluoric acids are used. These steps are generally performed on stainless steels as an aesthetic operation, to give a bright and clean surface, although some consider this step necessary for the corrosion resistance of the steel; it has been hypothesized that a region of chromium depletion exists under the mill scale, leaving the steel susceptible to corrosion. If it could be shown that it is unnecessary to blast and pickle stainless rebar, the cost of processing could be reduced, possibly to a level that would fit into tight construction budgets. Removal of the pickling stage could reduce the cost of stainless steel rebar by $500/ton, and with black steel rebar costing $1000/ton compared to $5500/ton for stainless rebar as of 2007, this cost saving could be significant where justifying the extra cost of stainless steel is concerned.

1.5 Research Objectives

Literature reveals that little work has been done to determine the corrosion resistance of stainless steel with its mill-scale intact. Several researchers state that a chromium depleted region exists below the mill scale, and that it is essential to remove it in order to restore the corrosion resistance of the steel; however, no actual experimental work is presented or referenced proving this. The objective of this research was to compare the corrosion performance of stainless steel rebar in the blasted and pickled condition with that of the same steel in the as-rolled condition, to determine if the removal of mill-scale and any chromium depletion is truly necessary. Several grades of steel in both pickled and as-rolled conditions were tested electrochemically, observing microcell corrosion response of bars in synthetic pore solution using a) discrete increments of chloride content, and b) rapid diffusion of chloride through a thin mortar shell. The results are interpreted in terms of the thermodynamic and kinetic behaviour of these alloys in high pH environments.

2 Literature Review

2.1 Corrosion Resistant Reinforcing Materials

Where black steel rebar is deemed inadequate as reinforcing material, options for corrosion resistance include epoxy coated and galvanized black steel, as well as stainless steel. Several convenient methods are employed for comparing a material's corrosion resistance to the well studied black steel rebar; determination of its chloride (Cl^-) threshold for corrosion initiation by $\%Cl^-$ by weight of cement [6,14,15] or by chloride/hydroxide ratio ($[Cl^-]/[OH^-]$) in pore solution [14,15,16,17,18], or by measuring pitting potential vs. Cl^- concentration.

For black steel rebar in sound OPC concrete, the threshold for corrosion initiation is generally between 0.01 and 0.1% Cl^- by mass of cement or $[Cl^-]/[OH^-]$ of 0.04 to 0.20 [1,6,14]. Epoxy coated rebar has the same Cl^- threshold as the base metal used, with the added protection of the physical barrier provided by the epoxy. Under ideal conditions, the epoxy will prevent Cl^- ions from reaching the steel, extending the time before corrosion initiates [6,19]. However, if the epoxy coating has imperfections present (such as pinholes) or is damaged prior to concrete being cast, corrosion in the presence of Cl^- will occur beneath the epoxy, destroying the coating and allowing for further surface to corrode [19]; if corrosion remains restricted to a small area, it may be far more severe than corrosion of a bare steel bar, causing local reduction in the rebar cross-section.

Another problem with epoxy coated bars is that epoxies will absorb moisture and slowly deteriorate when exposed to aqueous solutions, such as pore fluid in concrete. Moisture, which can collect at the rebar surface after passing through the epoxy, creates a peeling stress and surface oxidation which disbonds the coating, creating an ineffective barrier by the time Cl^- ions diffuse through the concrete to the bar [7]. Cl^- can then diffuse into the moisture between the bar and disbonded epoxy, initiating corrosion.

Galvanized steel rebar offers advantages over epoxy coated bars in that zinc acts as a sacrificial anode to the steel, corroding preferentially to the steel, and may remain passive to a pH below 10 [6]. Testing performed by Yeomans [6] showed the galvanized rebar to

have a chloride threshold approximately 2.5 times greater than that of black steel or epoxy coated black steel; the resulting time required for initiation of corrosion was 4-5 times that of the black steel. The galvanized coating was also shown to be effective in protecting any exposed substrate steel within about 8 mm of the zinc.

Despite the advantages provided by galvanizing the steel, corrosion is still inevitable in high chloride conditions; the coating thickness of zinc is typically on the order of 100 μm [6], and if cracks in the concrete allows Cl^- directly to the galvanized surface, corrosion will deplete the zinc coating and continue into the substrate steel.

Stainless steel rebar is truly corrosion resistant, not depending on the integrity of a coating, as the self healing chromium oxide (Cr_2O_3) surface film protects the substrate steel. Work by Mammoliti and Hansson [20] demonstrated that for typical stainless steels used for rebar, surfaces which were intentionally mechanically abraded in alkaline solutions containing 18% Cl^- repassivate in less than 20 seconds.

Hurley and Scully [16] compared the critical $[Cl^-]/[OH^-]$ ratio between black steel and several grades of corrosion resistant and stainless steels. They reported a critical $[Cl^-]/[OH^-] < 1$ for black steel, 4.9 for pickled Fe-9%Cr and 316L clad black steel, 9.7 for pickled 2101, and 20 for pickled 316LN.

2.1.i Nature of Stainless Steels

Due to the chromium content of these steels they form a passive film composed mainly of Cr_2O_3, which drastically reduces the corrosion rate even though it is typically less than 10 μm thick [8,21,22].

Typical metal oxide passive films form in the presence of oxygen (atmospheric or in oxidizing solutions or those containing dissolved oxygen). In aqueous solutions, a passive film can form on surfaces (or regions of a surface) exhibiting an anodic potential; Hoar [3] proposed that an H_2O molecule will align the oxygen (cathodic) end of the dipole structure to the anodic metal, the hydrogen atoms (protons) are driven off by the potential of the surface, and the metal oxide forms.

In the case of stainless steels, the passive Cr_2O_3 film is highly thermodynamically stable and forms almost instantly in the presence of dissolved oxygen under atmospheric conditions. In concrete (pH 13.5), Cr_2O_3 is stable below about 0 V vs. a standard hydrogen electrode (SHE) (-250 mV vs. saturated calomel electrode (SCE)) [4], which is lower than typical potentials of passive iron in concrete; if Cl^- ions cause the iron to corrode, the potential will decrease, at which point Cr_2O_3 will form and become protective.

2.1.ii Types of Stainless Steel Rebar

In a report on the condition of bridges along U.S. Route 101, the Coast Highway in Oregon, the suitability of different families of stainless steels for rebar are summarized. Ferritic and martensitic steels are deemed inadequate for reinforcement due to poorer corrosion resistance than other types of stainless steel and poor ductility [23]. Ferritic stainless steels require high Cr to have good corrosion resistance, and the lack of nickel makes them more prone to pitting than other grades. Martensitic grades require carbon, which tends to form $Cr_{23}C_6$ carbides, which promotes local Cr depletion and can allow intergranular corrosion.

Austenitic and duplex steels are strong, tough steels with can have high work hardening and have very good corrosion resistance and are therefore recommended for use as rebar. Austenitic steel gets its strength and toughness from the ductile austenitic structure, present due to the addition of Ni, which allows austenite to exist at temperatures typically experienced in reinforced concrete structures. The strength of austenitic stainless steel is highly dependant on dislocations within grains of the steel, giving these steels high work hardenability. Duplex steels contain ferritic and austenitic phases due to a lower Ni content; their high strength is attributed to a lamellar structure of austenitic and ferritic phases, ferrite being hard and strong, and austenite providing ductility to prevent brittle fracture [24].

The most widely used stainless steel grades for reinforcement are 304, 316, Nitronic 33 and Nitronic 50 austenitic and 2205 duplex stainless steels [11,23], the compositions of which are given in Table 2-1. These steels have high levels of Cr and Ni, which give

them excellent corrosion resistance. The lower Ni content of 2205 is supplemented by higher Cr content. Type 316, Nitronic 50 and 2205 benefit from the addition of Mo, which increases pitting resistance, making them especially well suited for high Cl^- environments [25]. The Nitronic grades have significant amounts of Mn; Mn can have an effect similar to Ni when used in stainless steel. Type 304 was used as rebar as early as the 1930s, but wider use began in the 1980s. Type 316, Nitronic 33 and 2205 gained popularity in the mid-1990s, with combinations of these with 304 being used in certain extremely corrosive environments [11].

Table 2-1: Nominal compositions of rebar grades, wt% [26]

	Cr	Ni	Mo	Mn	Si	N	C
AISI 304LN	18.4	8.5	0.4	1.4	0.7	0.14	0.015
AISI 316LN	16.5	11.5	2.1	1.4	0.7	0.14	0.015
AISI 240 (Nitronic 33)	17.5	2.8	0.5	11.0	0.7	0.26	0.04
AISI 209 (Nitronic 50)	21.4	12.2	2.1	5.0	0.8	0.28	0.02
AISI 318 (Alloy 2205)	22.2	5.1	2.9	2.0	0.7	0.18	0.015

Austenitic and duplex stainless steels featuring low carbon (denoted by L, e.g. 304L) are becoming increasingly popular for rebar; these grades are tougher, can be welded when necessary and are not prone to intergranular corrosion [27]. Regular stainless steels can experience excessive formation of $Cr_{23}C_6$ precipitates, which form by diffusion of carbon and chromium to grain boundaries; diffusion is slow at lower temperatures, so this phenomenon is generally only a problem for applications where welding is performed or elevated temperatures are required. When $Cr_{23}C_6$ precipitates form, the adjacent alloy becomes depleted of Cr, losing the stainless properties locally and creating a galvanic couple with the base steel, allowing intergranular corrosion.

Nitrogen is also added to some grades in order to provide solid solution strengthening (denoted by N, e.g. 304N); nitrogen occupies interstitial sites in the alloy matrix, increasing the stress required for slip to occur within the grains.

2.1.iii Economics of Stainless Steel Rebar

The primary reason stainless steel rebar is not chosen for structures subject to high Cl^- is cost. The price of stainless steel is inflated by both the cost of the alloying elements, but also the cost of pickling.

Iron is inexpensive compared to most other metals, especially those used for alloying in stainless steels. As of 2008, finished steel costs about $1000 Canadian dollars per metric ton (CAD/mt) [28], making black steel rebar quite cheap. Chromium is the cheapest of the major alloys used in austenitic and duplex grades, but is the largest portion; in 2005, the price of ferrochrome containing 65% Cr was near $2600 CAD/mt [29]. The next major alloying element is nickel, which cost approximately $20 000 CAD/mt in 2008. Molybdenum, although only used in small amounts (2-3%), is currently $75 000 CAD/mt. The price of nickel spiked to $60 000 CAD/mt in 2007, in 2005 molybdenum reached $125 000 CAD/mt, and the long term trends for the prices of these metals show steady increases [30,31]. Using 2008 prices with the composition of 304 stainless, the least alloyed of those previously discussed, the cost of a metric tonne in material alone rises from $1000 to over $3000 CAD/mt.

To further raise the price of the steel, the typical treatment of hot rolling, then blasting the steel with stainless steel chips and pickling in nitric (HNO_3) and hydrofluoric (HF) acids to remove the mill scale and restore the stainless surface [32] is estimated by the MTO to add $500 per tonne [20], resulting in a cost of around $5000/ton for finished stainless rebar. A 2007 cost comparison of the installed cost of black steel rebar with epoxy-coated black steel and stainless grades showed stainless steel to cost 5.5 to 7 times more black steel [33].

In a 1995 analysis of the cost of using different rebar types for several projects by an Illinois general contractor, stainless steel was priced at 6 times the cost of black steel, but the total costs of the projects increased only 6 to 16% [11] when costs of labour and other materials are factored in. In a similar, 2006 analysis of the budgets for two projects by the Oregon Department of Transportation, in which stainless steel was used selectively in

high Cl^- areas, the installed price of stainless was over 3 times the cost of black steel; the total costs for each bridge increased by 15% due to the stainless rebar [23].

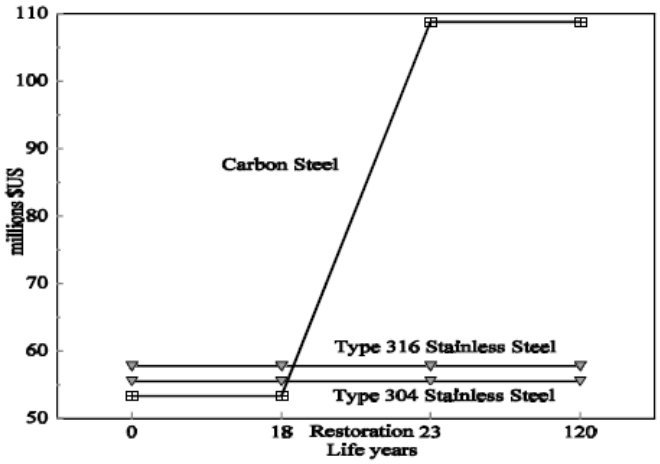

Figure 2-1: Approximate life-cycle costs of structure featuring stainless steels compared to carbon steel [34]

If those responsible for the budgeting of new structures consider initial costs of construction to be more important than life cycle costs, using stainless steel rebar can be too expensive to justify. However, until recently, not enough information on the performance of stainless rebars in real structures was available, so a realistic life cycle cost could not be estimated.

Figure 2-1 gives the approximate life-cycle costs of structures using black (carbon) steel, AISI 304 and 316 stainless steels. The cost of the structure with black steel more than doubles over its lifespan due to damage directly attributed to corrosion of the black steel, costs not experienced with either of the stainless steels. When savings over 3 or more decades is considered, black steel seems to be an obviously bad choice.

2.2 Preparation of Stainless Rebar

Stainless steel rebar is either hot or cold rolled to a desired size from a larger diameter bar. Cold rolling is not as common as hot rolling, but often follows it, because strain hardening limits the possible reduction for a given starting diameter; cold rolling occurs below the steel's recrystallization temperature, so deformation raises the dislocation density of the steel and hardens it [27].

Most stainless rebar is hot rolled at temperatures between 900 and 1200°C [35,36], hot enough to allow continuous recrystallization during deformation [27] but cool enough to avoid any incipient melting.

Hot rolling produces a Cr-rich mill scale on the surface of the rebar (containing Cr and Fe oxides) and Cr depletion is expected to exist in the steel adjacent to it; these are removed by abrasive blasting and pickling following the rolling process. The first step is to blast the bars with stainless steel wire chips; the mill scale, which is well adhered and dense compared to that of black steel, is disrupted and damaged, which will allow pickling solution(s) greater access to the base metal, so the entire surface of a bar can be dissolved and the mill scale removed evenly and efficiently [37]. Early abrasive blasting procedures used carbon steel chips, but this was believed to reduce the corrosion resistance of the steel by leaving small carbon steel particles embedded through the protective oxide layer, creating initiation sites for corrosion [32,38].

Pickling usually takes place in a mixture of HNO_3 and HF [32,36]. Stainless steels passivate in simple HNO_3 solutions, which is why HF is added; fluoride ions (F^-) destroy passive films (not mill scale) and allow the dissolution of the underlying steel [37]. It is generally agreed that the steel adjacent to the mill scale is dissolved; the mill scale itself is not dissolved but detached by the removal of steel it formed on. With the mill scale and underlying steel removed, the stainless steel has a clean, shiny surface.

2.2.i Chromium Depletion in Stainless Steels

Since the surface appearance is irrelevant when the reinforcing bars are being buried in concrete, the usefulness of pickling is to remove any Cr depletion. The only conclusive evidence of a Cr-depleted region on heat treated or hot-rolled stainless steel found in a literature search comes from research observing stainless steels exposed to high heat for long periods of time. Oxidation tests of 20% Cr-25% Ni at 850°C in CO_2 showed Cr depletion after 6000 hours (h), but none after 1000 h [39]. Oxidation of Fe-14.1% Cr stainless steel at 1200°C in O_2 for 1 h showed Cr depletion to a depth of about 5 μm [40], but this is an extreme environment, more oxygen-rich than in any hot-rolling procedure.

Extensive work by G C Wood and D P Whittle and Bombara, Tamba and Azzerri suggest that, in long term, high temperature oxidation tests, oxide scale forms in alternating layers of Cr-rich and Fe-rich oxides [36,41,42].

The hypothesis is that the Cr_2O_3-rich oxide begins to form and thicken, being thermodynamically favoured at base alloy compositions. This depletes the adjacent substrate steel of Cr. Stresses on the growing Cr-rich oxide cause it to crack, after which the Cr-depleted layer oxidizes into Fe-rich oxides; at this point the steel at the metal/oxide interface begins to form a new Cr-rich oxide, similar to the first (Fig. 2-2), with this cyclic growth slowing at a parabolic rate.

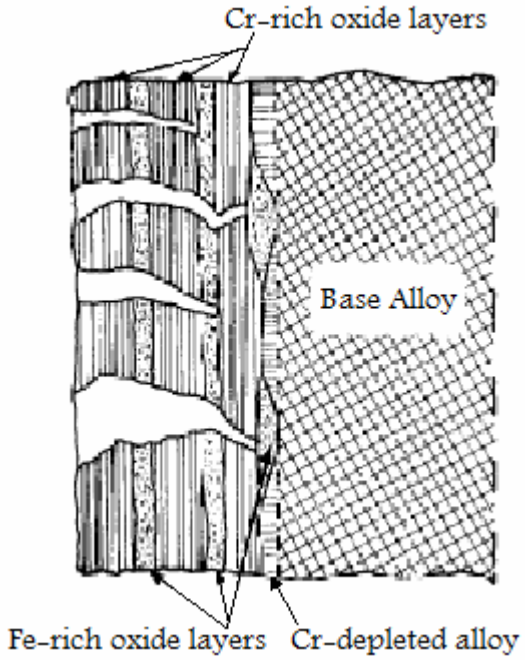

Figure 2-2: Long term oxide growth on stainless steel [36]

Wood and Whittle based this hypothesis on composition profiles of scales formed on stainless steels in long term, high temperature oxidation tests. Figure 2-3 shows the profile of Fe and Cr on Fe-16.4% Cr stainless steel held at 1100°C in air for 5 h, obtained by X-ray spectrometry. The alternating Cr-rich and Fe-rich oxides are clear. This oxide formed at very high temperature, and yet only one cycle of Fe and Cr-rich oxides formed. A similar profile for a 20 h test showed successive Fe and Cr-rich layers forming.

The order of the oxides is different in Figures 2-2 and 2-3, with Cr-depletion at the metal/oxide interface in Figure 2-2, but a Cr-rich oxide at the metal/oxide interface in Figure 2-3. This difference is only a result of the oxides being at different points of the cyclic oxide formation, but the

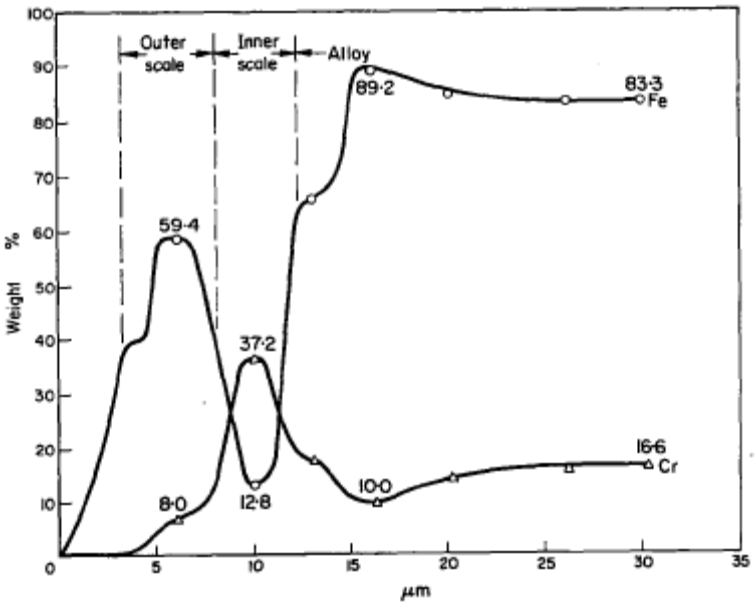

Figure 2-3: Composition of oxides formed on Fe-16.4% Cr steel [41]

mechanism by which they have formed is the same.

It may not be realistic to assume that Cr-depletion in stainless steels, as studied, is experienced in the production of stainless steel rebar. The stainless bars will be rolled at temperatures similar to those used by Wood and Whittle for the profile in Figure 2-3 [35], but the rolling process will have the bars at high temperature for less than an hour, while the Cr-depletion in Figure 2-3 was developed after 5 hours. The oxide scales studied were also formed on smooth, undamaged surfaces, while hot rolling plastically deforms the surface at high temperature. Studies of friction stir welds in type 304 (not low carbon) show that plastic deformation of the stainless at temperatures of 500 to 800°C causes recrystallization, breaking down oxide particles and allowing rapid diffusion of elements within the steel [43]; under these conditions Cr-rich oxides may form on the rebar during hot rolling, but the formation of a Cr-depleted region may not be necessary to facilitate it.

2.3 Corrosion Testing of Stainless Rebar

Corrosion testing of stainless steel rebar and reinforced concrete structures using them is modelled after testing performed on black steel. To date, most corrosion testing on stainless steel rebar is performed in synthetic pore solution, allowing high chloride concentrations to reach the steel in short periods of time; the biggest advantage of testing in solution is the ability to precisely control the Cl^- concentrations at the steel, allowing accurate determination of critical Cl^- thresholds and corrosion rates for specific Cl^- levels. Fewer results are available for testing in concrete or mortar, as many years may be required for diffusion to supply critical Cl^- thresholds for stainless steels in traditional tests for black steel.

The most commonly used methods of measuring corrosion in the literature reviewed include potentiodynamic and potentiostatic polarization scanning, macrocell current monitoring and AC electrochemical impedance spectroscopy (EIS). Most of these methods of corrosion testing have been performed on bars that were blasted and pickled or polished specifically for testing, and may not be useful in testing steels with mill scale intact.

2.3.i Corrosion Testing in Alkaline and Synthetic Pore Solutions

In testing of several stainless steels, including black steel with and without mill scale, Hurley and Scully [16] used potentiodynamic cyclic polarization (CP) scans, described in Chapter 3, to identify critical Cl^- thresholds; the critical Cl^- threshold for a steel was defined as the Cl^- concentration at which pitting was detected at potentials more negative than +200 mV vs. SCE in CP scans. Pitting is identified in these scans as a rapid increase in the measured corrosion rate during the CP scan. Tests were performed in a saturated calcium hydroxide ($Ca(OH)_2$) solution (often used to approximate pore solution due to pH of 12.5), and scans were performed 24 hours after adding NaCl to the cells so results could be attained in a short period.

316LN had a critical $[Cl^-]/[OH^-]$ ratio of 20; 316L clad black steel had a critical $[Cl^-]/[OH^-]$ ratio of 4.9, while black steel had a critical $[Cl^-]/[OH^-]$ ratio no higher than 0.34. The 316LN with mill scale had a critical $[Cl^-]/[OH^-]$ ratio of 0.5, much lower than the pickled 316LN, and only slightly higher than carbon steel. For LDX 2101, the critical $[Cl^-]/[OH^-]$ ratio drops from 2.5 for the pickled steel to 0.34 with mill scale. For Fe-9%Cr, critical $[Cl^-]/[OH^-]$ ratio drops from 4.9 for pickled to 0.2 with mill scale.

Hurley and Scully suggest that the corrosion resistance of stainless steels with mill scale intact is not better than black steel; however, this study did not address the materials tendency to repassivate, or how easily the conditions for pitting can be established locally on the surface under normal conditions. This work demonstrates that potentiodynamic cyclic polarization is a useful technique for comparing the corrosion performance of steels with and without mill scale.

In testing undertaken by G Blanco et al. [44], pickled bars of grades 304, 316L and 204Cu austenitic stainless steels and 2205 duplex stainless steel were subjected to CP and electrochemical impedance spectroscopy (EIS) in order to determine polarization resistance and approximate corrosion rates in the presence of Cl^-; chloride thresholds were not found in this work, rather, saturated $Ca(OH)_2$ solutions with 0 to 5 wt % Cl^- were used to test differences in corrosion performance in the presence of Cl^-. The results, although of a more qualitative nature, indicate 2205 performed the best, followed by

316L and 304, then 204Cu. The steels showed similar corrosion rates, within an order of magnitude of each other, but the 304 and 204Cu steels showed poor repassivation behaviour in polarization tests compared to that of the 2205 and 316L steels..

EIS involves applying a potential as an AC waveform, with variable frequency typically ranging from mHz to MHz, while recording the resultant current response [45]. Resistive and inductive/capacitive properties of the steel interface can then be estimated by fitting recorded current values to equivalent circuits. Equivalent circuits are electrical circuits which model the specific ionic/current transactions in the corrosion system using combinations of resistors and capacitors. By varying the input values of the resistance and inductance/capacitance values in the equivalent circuit, the frequency response can be altered to fit the experimental data.

Material interfaces, such as that between the surface of the rebar and pore fluid, provide a resistance to current flow as well as a double layer capacitance. This is modelled in EIS using what is referred to as a resistance/capacitance (RC) pair, where a resistive element and a capacitive element exist in parallel [45]. The two elements, in parallel, represent the different simultaneous interactions occurring at the surface. For rebar in pore solution, the resistance represents polarization resistance, R_P (refer to Chapter 3, Equation 6), which is a measure of the tendency of the steel to corrode in response to an applied potential, while the capacitive element, C_{dl}, represents the double layer capacitance at the surface [46].

Blanco also addressed the presence of sulphur (S) in stainless steel. Two samples of 316L were tested, one with 0.002wt% S, the other with 0.006wt% S. The pitting potential of the higher S steel, determined by CP, was 150 mV more negative than that of the low S steel. Analysis by scanning electron microscope (described in Chapter 3) revealed MnS precipitates up to 3 μm long. MnS inclusions are known to act as initiation sites for pitting [47], and are credited for reducing the pitting resistance of stainless steels with higher S content. This suggests that attention must be paid to the S content of stainless rebar, as the high S reduced the pitting potential by 150 mV, much larger an effect than changing the grade of stainless. Some caution must be exercised in

interpreting these results, however, because the steels tested were cold rolled to different diameters, so there may be an effect of work hardening on the corrosion behaviour of the steel, i.e. the MnS inclusions may be altered by different processing.

Although Blanco identified pitting potentials for different grades [44], no attention was paid to the difference in the repassivation behaviour of the steels. This is an aspect of pitting that should be given attention, as the differences in the pitting potentials of the steels was minor, but the potentials at which the steels repassivated after pitting varied by 500 mV between different grades. This is an indication of how easily the steel will repassivate; steel that cannot repassivate easily is not useful for rebar. In terms of repassivating, the 2205, which never pitted, performed best. 316L repassivated approximately 400 mV below the pitting potential, the easiest of those which pitted. 304 repassivated 700 mV below the pitting potential. 204Cu appeared to be repassivating 900 mV below the pitting potential.

Extensive EIS has been performed on 316 rebar in $Ca(OH)_2$ solutions in order to determine the electrochemical nature of the passive film formed on pickled or polished steel when cast into concrete. Several different equivalent circuits have been proposed to fit these data. Abreu et al. [46] found that an equivalent circuit of three RC pairs, one pair within another, within another (Figure 2-4) matched their experimental data.

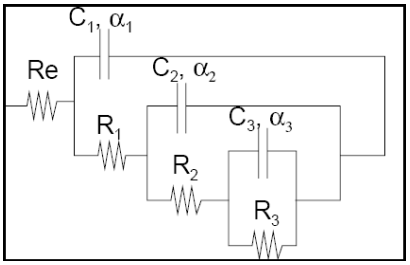

Figure 2-4: Equivalent circuit, stacked RC pairs [46]

A more commonly used equivalent circuit consists of two or three RC pairs in series (Figure 2-5): one pair represents the polarization resistance, R_P, and double layer capacitance, C_{dl}, of the steel, the second the steel/solution film resistance, R_i, and capacitance, C_i, and in the case of concrete, a third RC pair to

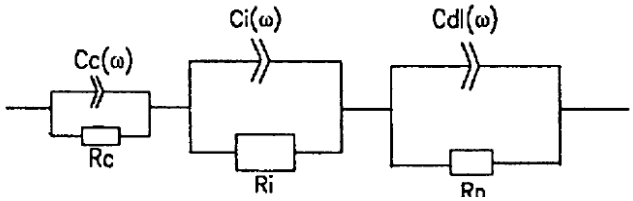

Figure 2-5: Equivalent circuit, RC pairs in series [48]

represent concrete resistance, R_c, and concrete matrix solid/liquid interface capacitance, C_c [44,48].

Although the results of EIS testing confirmed that the method is useful for finding corrosion rate with pickled or polished surfaces [44,46], the mill scale will require a much different and much more complicated equivalent circuit. Possible electrochemical interactions at the rebar surface are between base steel and mill scale, mill scale and pore fluid, and between base steel and pore fluid, with the last occurring in parallel with the previous two, which are in series when constructing an equivalent circuit. The complexity of the corrosion system of rebar with mill scale make it too complicated to be useful for testing rebar with mill scale intact.

Another technique, used by Abreu [46] on pickled stainless rebar, is cyclic voltammetry, an electrochemical technique in which a CP scan is repeated until the current response is similar from cycle to cycle. This technique is similar to CP, and plotting potential vs. current reveals potentials at which passivity forms, pitting occurs, etc [46,49]. This technique is not useful for steels with mill scale, as each cycle would alter the mill scale, and the final result would not necessarily reflect the corrosion behaviour of the original mill scale surface.

2.3.ii Corrosion Testing in Concrete and Mortar

Limited results of corrosion testing of stainless steel rebar in concrete or mortar have been published, but those available agree with results obtained through field trials and in solution testing. The testing that has been reported consists of results obtained by accelerated testing techniques and interim results of extended studies.

In work undertaken by the National Research Council (NRC) of Canada [48], concrete prisms were cast with embedded black steel or AISI 240 (high Mn, low Ni stainless steel, also known as Nitronic 33) and admixed Cl^- (premixed in water used to mix cement). The concrete prisms were submerged in a 3.5% NaCl bath for 25 to 27 months prior to testing. EIS was performed on the prisms, using the series RC equivalent circuit shown in Figure 2-5. Polarization resistances (R_P) were found by means of fitting the equivalent circuit model to generated curves, and corrosion rates approximated from those. Black

steel samples had corrosion rates more than 50 times that of comparable Nitronic 33 samples.

These results show differences between the corrosion performance of black and stainless steels similar to results from testing in pore solution, indicating that R_P values calculated from EIS are a good approximation of corrosion rates of stainless steels, assuming that the equivalent circuit model used is correct.

In the work performed at the NRC [48], Cl^- was admixed in the prisms as $CaCl_2$. The decision to use $CaCl_2$ was probably made in order to reduce the cations added to the concrete matrix when compared to NaCl or KCl. $CaCl_2$ is a bad choice for adding Cl^- to test specimens, as work by Hansson et al. [50] demonstrated that $CaCl_2$ reduced the pH of the concrete pore solution and opened up the pore structure of the cement paste (leading to increased electrical conductivity and ionic diffusivity), both of which are expected to have increased the corrosion rate.

It should also be noted that Cl^- was added at the time of casting for these tests. This is not representative of rebar in actual structures, where the steel would have years to form phases or oxides thermodynamically stable in concrete before Cl^- reached the steel surface.

Trejo and Pillai [14,15,51] designed and performed a series of accelerated corrosion tests first on A 615 and A 706 carbon steels, and then on microcomposite (10.4% Cr), 304 and 316LN steels. Tests involved casting a small sample of the steel, as well as electrodes, in a mortar cylinder. A potential of 20 V was applied between an anode near the steel sample and a cathode in a high Cl^- bath on top of the cylinder; the potential caused Cl^- ions to diffuse through the mortar much more quickly than under ambient conditions, reducing the time required for the test from decades to days. Corrosion rates were found by performing linear polarization resistance (LPR) scans (described in Chapter 3) and calculating polarization resistance from them.

Values of the critical Cl^- thresholds for the carbon steels, microcomposite steel and stainless steels are presented graphically in Figure 2-6. These results agree well with

those found by Hurley and Scully [16] for both black steel and pickled 316LN in simulated pore solution.

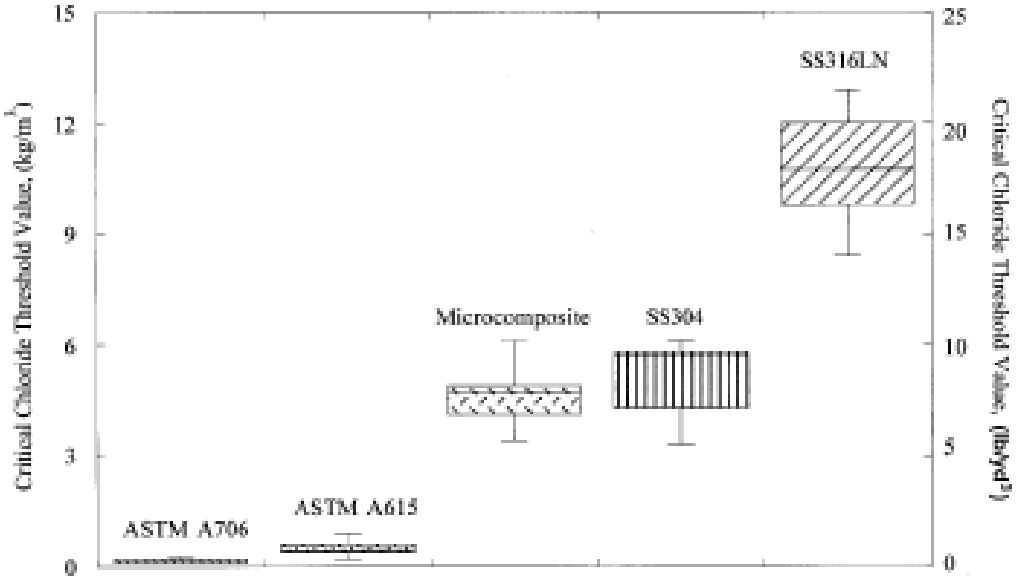

Figure 2-6: Critical Cl^- thresholds for selected rebar [15]

An obvious drawback to Trejo and Pillai's accelerated method [14,15,51] is that the high potential gradient will reduce the pH of the pore solution by oxidation of the hydroxyl ions:

$$2OH^- \rightarrow \frac{1}{2}O_2 + H_2O + 2e^- \qquad (2)$$

Through the duration of the tests (about two weeks) using 20 V, the pH near the steel samples was reduced from 13.1 to 12.5. Reduction of the pH may not even be a drawback since carbonation (reduction of pH) may occur in real structures in the decades this test is designed to simulate.

Trejo and Pillai determined that microcomposite steel (~10% Cr) and 304 had Cl^- thresholds of 4.6 and 5.0 kg/m^3 in concrete, respectively, while 316LN had a Cl^- threshold of 10.8 kg/m^3 [15]. Previous work gave Cl^- thresholds of 0.2 to 0.5 kg/m^3 for black steel in concrete [14]. A simple damage model, for a specific bridge application, proposed by Miller and Darwin [52], states that years to corrosion are approximately

equal to the Cl^- threshold in kg/m^3 divided by 0.3 $kg/m^3/yr$, which suggests that the time to initiation of corrosion is 1 to 2 years for carbon steel, 15 years for microcomposite, 17 years for 304, and 36 years for 316LN.

Garcia-Alonso et al. [53] studied carbon steel, 304, 316 and two low-cost, low-Ni grades, in which Mn was substituted for the bulk of the Ni. Slabs were cast with Cl^- contents of 2 and 4% by weight. Slabs were also cast with no chlorides, and then submerged in a bath containing 3.5% NaCl by weight of the solution, near that of seawater.

Corrosion potential (E_{corr}) and corrosion current (i_{corr}) were monitored over a period of 2 to 2.5 years using LPR. For up to 4% Cl^- in cement, the stainless steels showed no signs of corrosion initiation as either a distinct change in E_{corr} or a rapid increase in i_{corr}. CP was also used in order to determine pitting potentials for the steels in the different Cl^- contents. Pitting potentials of the stainless steels were all above +500 mV vs SCE, high enough that pitting of these steels in high Cl^- concrete environments is unlikely under normal conditions without an artificially applied potential.

These tests were useful in providing the corrosion behaviour of the steels for prescribed Cl^- contents, but Cl^- thresholds were not determined. Having to cast a separate prism for each Cl^- level studied also makes this method tedious; testing in pore solution is preferred since Cl^- content can be easily controlled and varied.

Of the electrochemical methods used in the literature, linear polarization resistance and potentiodynamic cyclic polarization seem to be the most appropriate for the testing of rebar with mill scale intact. LPR scans provide corrosion potentials and rates using only a small potential perturbation over a short period, so the effect on the mill scale is minimal. CP scans provide corrosion potentials and pitting potentials, as well as the repassivating behaviour of the steel; when performed with a relatively high scan rate over a limited potential range, damage to mill scale can be minimized.

Although EIS and cyclic voltammetry were used extensively in the literature, these methods were most useful in comparing corrosion performance between different grades. EIS could be applied to the steels with mill scale, as the potential perturbation is small,

but the effort required to find an appropriate model may be beyond the scope of this project. Cyclic voltammetry is not appropriate for testing steels with mill scale, as each potential cycle will alter the surface by attacking the most vulnerable points (Cr-depleted areas); cyclic voltammetry is most useful in comparing polished samples of different grades, where polishing leaves a smooth, homogeneous surface.

2.3.iii Effect of Surface Condition and Oxides on Corrosion

Many previous tests of the corrosion performance and critical Cl^- threshold of black and stainless steels used samples which were ground and polished prior to testing. This treatment was intended to give a homogeneous surface and reduce the variability of results; however, the surface condition has been shown to have a major effect on corrosion currents and pitting potential. Mammoliti et al. [54] compared the effect of the surface condition by suspending rebar specimens in concrete pore solution with surfaces intact, ground with 600 grit SiC paper, or metallographically ground and polished. Corrosion rates are significantly lower for polished specimens when Cl^- is present; i_{corr} of the unaltered rebar specimens were 2 to 10 times greater than those of polished specimens. Pitting potential was also highly affected by polishing; a polished specimen did not pit in 3% Cl^- solution, while the unaltered surface pitted 400 mV above E_{corr}.

Pillai and Trejo [51] demonstrated that in their accelerated corrosion test, carbon steels and 304 stainless have a 25% higher Cl^- threshold when polished, but 316LN showed a 65% reduction when polished as opposed to the original pickled surface. The reduction in Cl^- threshold for 316 could be attributed to the removal of a thick passive film previously formed during the removal of mill scale; another possibility for the reduction in Cl^- threshold would be the presence of microvoids at the surface, exposed by removal of material in the polishing process.

The difference observed between surfaces which have undergone various levels of polishing indicate the major role that surface roughness has on corrosion and suggest that tests on polished and prepared surfaces are unrealistic. The difference seems to be that the inhomogeneous surface of the original rebar promotes the formation of local anodic

and cathodic sites, allowing initiation of corrosion with less Cl^- present, or at lower applied potentials.

Alonso et al. [55] found that, in the case of carbon steels, the reduction of iron from Fe^{3+} to Fe^{2+} within the corrosion product on the steel surface is able to mask part of the corrosion reaction, and leads to an underestimation of the actual corrosion rate. This effect may be important in measuring the corrosion of steels having intact mill scale, as it is composed mostly of Fe_2O_3.

2.3.iv Summary of Corrosion Testing of Stainless Rebar

Corrosion testing of stainless steel rebar with and without mill scale in pore solution reported in literature addressed the critical chloride threshold, but the thresholds reported were for a critical pitting potential [16] rather than a maximum corrosion rate under equilibrium conditions. Results were not reported for corrosion rates, only the pitting potential. Pore solution testing in this study monitors the corrosion rate of the steels in addition to pitting potentials, as chloride content increases from zero to concentrated chlorides. Corrosion rates, as opposed to pitting potential, are a good indicator of corrosion behaviour/resistance of rebar in concrete, because the potentials at which these steels pit are above the potentials naturally observed for the steels in concrete.

Corrosion testing of stainless rebar in cement paste, mortar and concrete was found in the literature, but focused on pickled or polished stainless surfaces, whereas the present project is aimed at determining the behaviour of the steels with mill scale. Moreover, much of this testing involved casting chloride directly into the paste or mortar, which may not have allowed the natural passive surface of stainless steel in concrete to form. For this study, corrosion testing of steels in mortar did not have cast in chlorides, rather, the chlorides were driven in through mortar due to an applied potential at the rebar surface.

3 Experimental Procedure

3.1 Test Materials

In order to observe the effects of mill scale on the corrosion resistance of stainless steels, 3 grades of steel in both as-rolled and pickled conditions have been tested. The *as-rolled* (AR) condition refers to steel with its mill scale formed during hot-rolling intact. The *pickled* (PIC) condition refers to the steel which has undergone typical post rolling procedure for stainless steels; blasting with stainless steel chips to remove mill scale, and then pickling in a mixture of nitric (HNO_3) and hydrofluoric (HF) acids to remove any remaining oxide and any Cr-depleted layer.

The steel grades tested were AISI 304LN (S30453), AISI 316LN (S31653), and alloy 2205 (AISI 318L/S31803). Compositions of these steels are provided in Table 3-1.

Table 3-1: Compositions of stainless steels tested, wt%

	Cr	Ni	Mo	Mn	Si	N	S	C
304LN	18.24	8.59	n/a	1.27	0.56	0.13	0.009	0.018
316LN	17.17	10.56	2.09	1.48	0.54	0.15	0.023	0.018
2205	22.63	5.52	2.76	1.49	0.43	0.14	0.001	0.028

(Valbruna steels only, bulk is Fe)

304LN is a low carbon, high nitrogen version of the commercially popular, less expensive 304 austenitic stainless steel. The low carbon allows welding without extensive sensitization and increases toughness, while the nitrogen provides interstitial solid solution strengthening and increases pitting resistance.

316LN is similar to 304LN; it contains slightly less Cr, but contains more Ni and Mo, which are expected to improve resistance to passivity breakdown and pitting. Both Ni and Mo increase the cost of this steel.

2205 is a duplex stainless steel, containing both ferritic and austenitic phases; it has low Ni content compared to the other steels, so some ferrite exists. The resulting microstructure is a lamellar structure within the grains. The dual phase nature of this alloy makes it extremely strong and tough. Higher Cr and the addition of Mo make it expensive, so its use is most often limited to applications requiring high strength.

All the bars were hot-rolled ribbed commercial rebar. Most of the stainless steels were provided by Valbruna Stainless Steel, but previously acquired stainless bars from Carpenter Technology Canada were also tested to determine any detectable behavioural differences between bars from different suppliers.

Table 3-2: Grades, diameters and surfaces of stainless steels tested

	2205		304LN		316LN	
	AR	PIC	AR	PIC	AR	PIC
Valbruna	n/a	15M	20M	20M	20M	15M/20M
Carpenter	15M	15M	n/a	n/a	15M	15M

15M = ~16mm dia., 20M = ~20mm dia., n/a = not available

The available steels give 9 or 10 test variations, with comparisons available between grade, treatment, producer and diameter (Table 3-2).

From this point, the steels will be identified by a "C" or "V" denoting Carpenter or Valbruna steels respectively, followed by the grade, then "AR" or "PIC" identifying the surface condition. For example, Carpenter 316LN in the pickled condition will be referred to as C316LN PIC.

3.2 Investigating Cl^- Solubility in OPC Pore Solution

It was expected that the chloride corrosion threshold of these steels may be near the solubility limit of Cl^- in concrete pore solution. Information was not found in the literature regarding the solubility of Cl^- or NaCl in pore solution, which is in direct contact with the steel. Therefore, the following procedure was carried out to provide the information.

In order to determine the solubility of Cl^- in pore solution, a series of 100mm x 50mm diameter cylinders of cement paste were cast using type 10 OPC with a water cement ratio of 0.5 and NaCl additions of 0.1, 0.5, 1.0, 2.5, 5.0, 7.5 and 10.0% Cl^- by weight of cement. Cement paste was cast into cylinders, and then capped to prevent moisture loss. The cylinders were left to cure in the lab under ambient conditions for 24 hours, while being constantly rotated to prevent bleeding within the cement paste, after which they were placed in a humidity chamber (100% relative humidity near room temperature) for 28 days.

Pore solutions were extracted after approximately 28 days, following the pore solution extraction procedure outlined by Barneyback and Diamond [56], in which the cylinder was placed under compression using a steel chamber and piston in a press. High compression of the cylinder destroyed the structure, eventually forcing the interstitial fluid out through a small fluid collection duct into a syringe. Solution was extracted from 3 cylinders of each Cl^- level.

Pore solutions were then titrated in order to determine the chloride content using silver nitrate ($AgNO_3$), which precipitates AgCl from the solution. Conductivity and potential of the solution decreased due to Cl^- being depleted in the solution. Using a silver electrode and a reference electrode, an inflexion point in the curve of potential vs. amount of titrant was found; knowing the volume of solution used, the Cl^- content of the original solution was calculated.

The results of this investigation were used to determine the increments in which NaCl was added to the pore solution cells described below, based on fractions of the solubility limit.

3.3 Synthetic OPC Pore Solution Testing

The first major set of corrosion tests was designed to evaluate the corrosion response of the steels in synthetic pore solution with incrementally increasing chloride concentrations. Short, electrically isolated bars were suspended in a synthetic pore solution simulating the pore fluid in type 10 OPC cement aged 28 days. Cl^- ions were then added as NaCl until the solutions reached 16% Cl^- by mass of solution. By having bare bars in synthetic pore solution, as opposed to casting them in concrete, the concentration of Cl^- at the surface of the bars could be precisely controlled. Open circuit potentials (E_{corr}), linear polarization resistance (LPR) measurements and cyclic polarization (CP) scans were recorded at increasing increments of Cl^- content, in order to determine the critical chloride concentration for active corrosion initiation.

3.3.i Preparation of Bars and Test Cells

Rebar samples were either received in 125 mm lengths or cut to size from longer lengths. In order to provide an electrical connection, a 4.1 mm hole was drilled into the end of each bar, and then was tapped with a 10-32 thread. These grades of stainless steel are extremely tough (due to low carbon) and highly work hardenable (interstitial alloy atoms and low initial dislocation density), so a solid carbide bit was necessary to drill into them. The 4.1 mm hole was oversized for the 10-32 tap in order to reduce stress and wear on the tap. 32 mm long stainless steel machine screws were then installed as electrical connections, with a flat stainless steel washer to suspend the bar in the test cells (Figure 3-1).

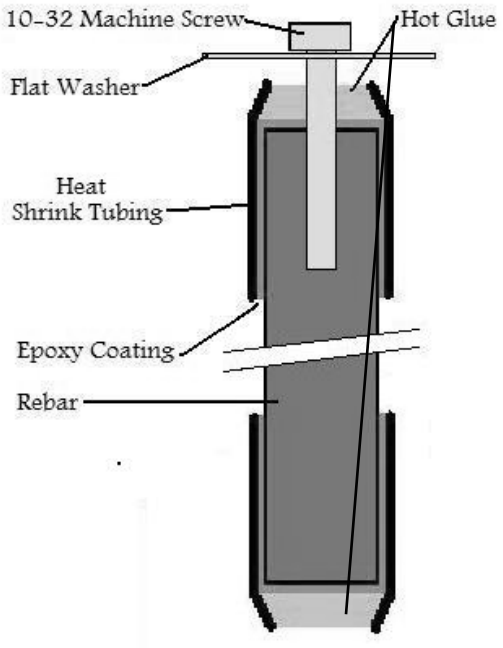

Figure 3-1: Hardware and preparation of bar ends for pore solution cells

The ends of the bars were sealed using 3 coats of SICAfloor 261CA epoxy sealer, and then covered with heat-shrink tubing. The ends of the tubing (one of which the machine screw passes through) were sealed with hot glue. The length of steel between the coated ends determined the area exposed in the corrosion test. For 15M bars, 75 mm of each bar was exposed, giving a nominal exposed area of 3770 mm^2. In order to achieve a similar area with the 20M bars, 65 mm were exposed, giving a nominal exposed area of 4080 mm^2.

Test cells used were 2.8 L polyethylene food storage containers. The lid of each cell had (5) 22 mm holes for rebar samples, equally spaced around a central 12.7 mm hole for a saturated calomel electrode (SCE), used as the reference electrode in electrochemical tests. The bars were suspended in the cells as seen in Figure 3-

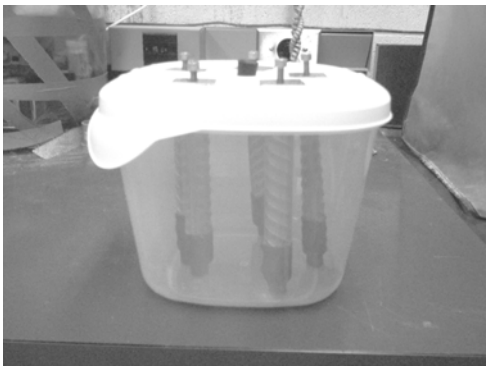

Figure 3-2: Synthetic pore solution cell

2. Several small holes were also made in the lid for the insertion of a Pt wire as a counter electrode.

3.3.ii Synthetic Pore Solution and Chloride Addition

Synthetic pore solution was mixed according to the composition determined by Marcotte [5] for solution expressed from type 10 OPC at 28 days, as listed in Table 3-3. The recipe given was adjusted to achieve the desired volume of pore solution for a single cell and batches were mixed directly in the container used in the cell so that no pore solution or solid constituents were lost in transfer. This solution has a pH of about 13.7.

Table 3-3: Synthetic pore solution composition [5]

Compound	Quantity (g)
NaOH	12.8
KOH	44.9
$CaSO_4 \cdot 2H_2O$	1.38
$Ca(OH)_2$*	5.71
H_2O	2.43L

* Excess amount

Cl^- was added in increments of 2.5% by mass to 10%, then by 2% to a total of 16% (Appendix A). Cl^- was added as NaCl, the mass of which was calculated as follows:

$$m_{Cl} = \left(m_{solution} + m_{NaCl}\right) * \%Cl^- , \tag{3}$$

where m_{Cl} is the mass of Cl^- to be added, m_{NaCl} is the mass of NaCl to be added, $m_{solution}$ is the mass of the solution, and $\%Cl^-$ is the desired Cl^- content by mass of solution. Equation (3) calculates the amount of Cl^- to add, based on the mass of the original solution plus the mass of NaCl to be added. Rearranging equation (3) to find m_{NaCl} (where $m_{Cl} = 60.661\%\ m_{NaCl}$ based on the mass percentage of Cl^- in NaCl):

$$m_{NaCl} = \frac{\left(\%Cl^- * m_{solution}\right)}{\left(60.661\% - \%Cl^-\right)} \tag{4}$$

The bars were allowed to equilibrate in the solution for two weeks prior to the addition of chlorides. Corrosion tests were performed at each Cl^- concentration. After NaCl

addition, cells were allowed to rest for five days prior to any testing. This delay was intended to allow the cells to reach equilibrium, with all Cl^- dissolved into solution.

Due to the addition of NaCl, the cells were near overflowing at 10% Cl^-, so a smaller volume of fresh solution was mixed with 10% Cl^- and the bars were transferred before testing continued up to the maximum of 16% Cl^-.

3.3.iii Cyclic Polarization Testing

Tests were performed using an EG&G 273A Potentiostat, controlled by Princeton Applied Research's PowerSuite software through a PC. This system uses a 3-electrode setup (Figure 3-3): the rebar acted as the working electrode; a saturated calomel electrode (SCE) was used as a reference electrode (against which the bar's voltage was controlled); a Pt wire was used as a counter electrode (supplying and accepting current from the bar). The system measured and stored the open circuit potential of the bar, then applied the anodic and cathodic potentials while logging the current between the rebar and counter electrode.

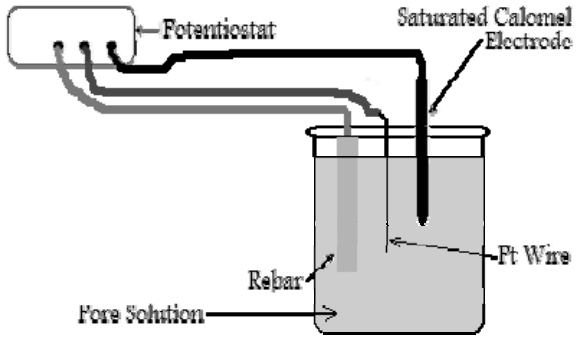

Figure 3-3: Pore solution cell and potentiostat configuration

Potentiodynamic cyclic polarization (CP) scans (Figure 3-4) were performed on one bar from each cell at Cl^- levels of 0, 5 (or 7.5), 10 and 16%. In these tests, the potential applied to the rebar was dynamically changed as the resulting current was monitored. Prior to the CP scan, the open circuit potential (E_{corr}) was measured and scans began 50 mV below the measured E_{corr}, and increased anodically to between +450 and +750 mV vs. SCE (in order to reach the transpassive region, but avoid excessive corrosion if possible), then decreased to between -400 and -1000 mV vs. SCE (in order to reach concentration polarization). Several scans were performed at 0.1, 0.05, 0.03 and 0.01 mV/s in order to determine the effect of using a different scan rate. However, most scans were carried out at a rate of 0.1 mV/s, as it was expected to be adequately slow for stable

readings; similar scans found in the literature used a scan rate of 0.167 mV/s [15,16,27]. The resulting current was recorded every 0.5 mV.

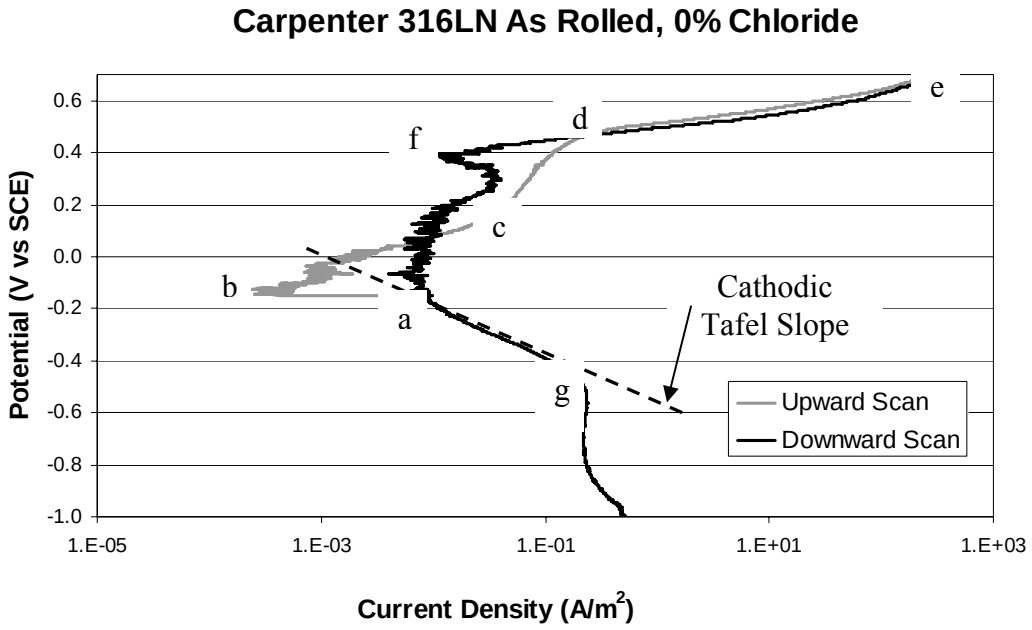

Figure 3-4: Typical cyclic polarization scan of 316LN

The anodic scan in Figure 3-4 started at point (a); the scan continued with a cathodic current to point (b), at E_{corr}, where anodic and cathodic currents were equal and the resultant measured current approached zero. According to Beverskog [57], this corresponds to the maximum stability potential for Cr_2O_3, above which it dissolves as CrO_4^{2-}. As the scan progressed upward, the now anodic current increased to point (c), and then increased more slowly to point (d), possibly due to a partially protective film of Fe_2NiO_4 [57]. The sharp increase at point (d) indicated dielectric breakdown of the film due to the high potential gradient across the film, so current increased quickly to point (e), where the scan reversed.

The current in the descending scan initially dropped along the path of (e) to (d), and then reached a minimum in current at point (f). This point was the new value of E_{corr}, which was more positive due to the protective film on the steel, built up in the ascending scan.

The scan continued beyond point (a), with cathodic current increasing to point (g), where the cathodic current limit (concentration polarization) was reached.

These scans were used to observe pitting potentials for the steels and to calculate constants needed for other electrochemical work, as described below. Pitting potentials are identified in CP curves as a point where current rapidly increases by several orders of magnitude. The curve will be flat where current has increased due to pitting, as opposed to transpassive behaviour, where the current rises in relation to potential, as seen in Figure 3-4. Pitting is a corrosion phenomenon where local anodic sites are formed on the surface, creating small patches of reduced pH and establishing a galvanic corrosion cell between the pits and the non-pitting areas surrounding them.

A constant *B*, which was used to calculate corrosion rates for LPR, was derived from the cyclic polarization curve using the relation:

$$B = \frac{\beta_a \beta_c}{2.3(\beta_a + \beta_c)}, \tag{5}$$

where β_a and β_c are Tafel constants, which relate the anodic and cathodic overpotentials (η_a and η_c respectively) in the polarization scan to the anodic and cathodic applied currents i_a and i_c by equations (6) and (7):

$$\eta_a = \beta_a * \log\frac{i_a}{i_{corr}} \qquad (6) \qquad\qquad \eta_c = \beta_c * \log\frac{i_c}{i_{corr}} \qquad (7)$$

Physically, equations (6) and (7) relate to the cyclic polarization scan in that β_a and β_c represent the linear slope of the scan within ±50 to 100 mV from E_{corr} [58]. The cathodic Tafel slope is labelled in Figure 3-4.

3.3.iv Linear Polarization Resistance Testing

The linear polarization resistance (LPR) technique was performed on each bar at every Cl^- level, measuring E_{corr} and microcell corrosion current. LPR scans consisted of subjecting a bar to an impressed overpotential of +10 mV from the bar's E_{corr}, and monitoring the current response over 60 seconds, then repeating for -10 mV from E_{corr}.

Potential was applied and current recorded using the same equipment and electrode configuration as the CP scans; for some scans a Princeton Applied Research model 2263 PARStat potentiostat was used instead of the EG&G described in Section 3.3.iii.

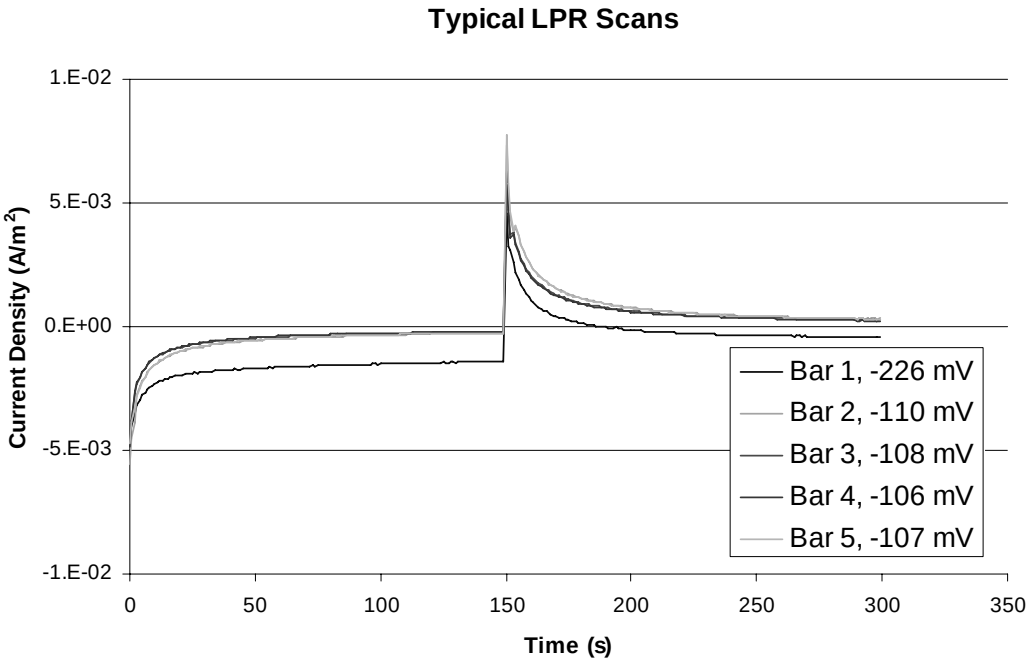

Figure 3-5: Typical LPR scans of 316LN stainless steel

Figure 3-5 demonstrates the current approaching steady state in both anodic and cathodic scans. Typically the LPR technique is used on steel in concrete employing a potential difference of ±20 mV, in order to account for a voltage drop due to concrete resistivity. In the case of the pore solution cells there was no concrete, thus solution resistance was negligible and ±10 mV was considered to be appropriate.

Following each LPR scan, the values obtained for current were entered into an Excel spreadsheet which first converted the raw current data to current density by dividing by the exposed area of the bars (m^2). The Stern and Geary relation [59] was used to calculate the corrosion current density of the steel (i_{corr}):

$$R_P = \frac{B}{i_{corr}} = \frac{\Delta E}{\Delta i}, \tag{8}$$

where ΔE represents the potential difference of 20 mV, and Δi is the difference between anodic and cathodic steady state currents in the LPR scans, taken from Figure 3-5. The polarization resistance (R_P) of the steel is a value reflecting the material's tendency to corrode subject to overpotential; R_P is inversely proportional to the corrosion current density, i_{corr}, so a relatively high R_P indicates a relatively low corrosion rate. B is a constant, approximated using slopes taken from cyclic polarization curves, as described in the previous section.

The corrosion rates are calculated in terms of current density through the surface, but it is more comprehensible to present rates in terms of depth loss over a specified time. Corrosion current density can be converted to a linear depth loss using Faraday's Law:

$$r = \frac{i_{corr} \cdot a}{\rho \cdot n \cdot F} \tag{9}$$

where r is the rate in m/s, a is atomic mass in grams (g/mol), ρ is the density in g/m^3, n is valence number of corroding species, and F is Faraday's constant (96 500 C/mol). It is assumed that the corroding species is iron, so valence, atomic mass and density are chosen as those of iron. Equation (9) can be simplified to a proportional relation between r and i_{corr}, and this can be further adjusted to represent the rate in μm/year (Appendix B):

$$r_{(\mu m / year)} = 772.66 \cdot i_{corr} \tag{10}$$

3.4 Rapid Chloride Diffusion Testing

The second major corrosion test was modelled after testing performed on black steel by Hansson and Sørensen [1], where a small anodic potential was applied to steel in concrete in order to create a potential gradient in the concrete, forcing Cl^- ions to diffuse toward the steel surface faster than under normal ambient conditions. Rebar cast in cement mortar was placed in a pore solution with high Cl^- content. A potentiostat was then used to apply a static anodic potential to the bars, using the same 3-electrode configuration used in the previous test. The current between the bars and the counter electrode was monitored automatically using a multimeter switch and a PC. The goal was to observe

the current through the bars, watching for the current to increase rapidly, indicating that a Cl^- threshold had been reached and corrosion had initiated. At this point the bar could be autopsied, and the Cl^- content at the surface of the steel measured in order to determine the Cl^- threshold.

3.4.i Preparation of Bars in Mortar

For this round of testing, the bars were prepared in the same way as for the pore solution cells. A 12.7 mm long machine screw was substituted for the 32 mm machine screw described in Section 3.3, allowing the screw head to be tightened down to the face of the rebar. An electrical connection was established by wrapping a wire around the machine screw, then tightening the screw head down to secure it, as illustrated in Figure 3-6. These bars were cast in mortar, so by attaching the wire at the steel/screw interface, then sealing with epoxy, shrink tube, and hot glue, the exposed rebar surface was the only conductive surface exposed to the cement paste and Cl^- ions, eliminating any corrosion effects of the screw or wire in electrochemical measurements.

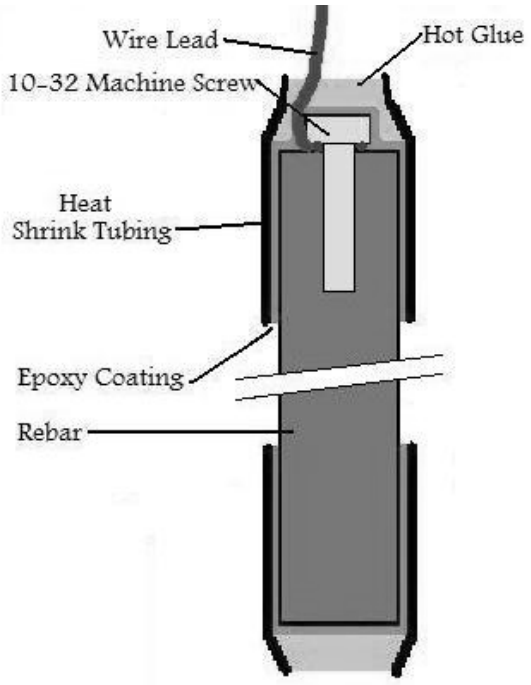

Figure 3-6: Hardware and preparation of bar ends for mortar bar samples

In order to allow Cl^- ions to diffuse to the steel rapidly, a thin shell of mortar was preferable to a thick layer. The design of the specimens cast in a mortar shell was modelled after work by Darwin et al. at the University of Kansas [60]. Figure 3-7 illustrates the moulds made for casting bars with a mortar shell of 8-10 mm thickness, using nominal 1-1/4" and 1-1/2"

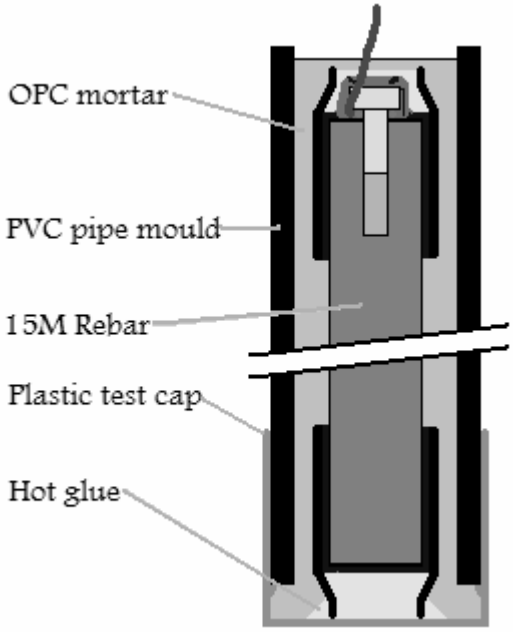

Figure 3-7: Mould for casting mortar bars

diameter schedule 40 ABS tubing for 15M bars and 20M bars respectively. The sealed but unwired ends of the prepared bars were hot glued to the centre of a plastic cap, which then had a 150 mm length of the tubing inserted to complete the mould. The lengths of tubing were cut vertically from end to end in order to allow a slight opening of the tubes for the bars to be removed from the moulds following casting.

For the mortar, type 10 OPC was used. Mortar was mixed with a water-cement-sand ratio of 1:2:4. To prepare the mortar, cement and water were first mixed together for 30 s at low speed. Next, sand was gradually added to the cement paste for 30 s. At this point the mortar was mixed aggressively for 90 s, left to rest for 60 s, and then mixed for an additional 60 s.

Moulds were filled with about 1/3 of the required mortar, and then tamped 25-30 times with a glass rod. This was repeated at about 2/3 filled and completely full. Tamping was performed in order to reduce porosity, releasing any bubbles trapped in the mortar or sticking to the rebar or mould.

During early attempts at casting, hot glue and tape were used to seal the cut seam in the lengths of ABS tubing in order to prevent the mortar from leaking out. Most of the samples prepared in this way had surface cracks and were therefore not suitable for testing. It was speculated that shrinkage was causing the cracks; further samples were cast without sealing the seam, allowing fluid to bleed out from the mortar and allowing air to enter the mould during any shrinkage. Samples cast with an open seam did not crack, so this method was used for the remainder of samples cast.

3.4.ii Preparation of Pore Solution Bath

For this test, all of the samples rested in the same bath of solution. A large, shallow plastic tub was prepared for this experiment. The lid of the tub was modified to hold a saturated calomel electrode as a reference electrode in the 3-electrode configuration. Graphite rods were drilled with a 2.4 mm hole on one end, then wires were soldered into the holes, and hot glue was used to secure the wire to the end, preventing the solder from pulling out; these rods were distributed and secured along the bottom of the tub with hot glue to use as counter electrodes. Synthetic pore solution, of the composition given in

Table 3-3, was mixed in large quantities for this test. Cl^- was added to the solution to provide a concentration of 12% Cl^- by mass of solution.

3.4.iii Wiring and Equipment Configuration

Four mortar-covered bars of each Valbruna steel and four black steel mortar covered bars were placed in the solution. Each bar was wired to a 10 Ω resistor, after which all of the bars were connected to a common lead. The common lead was connected to the potentiostat as the working electrode (Figure 3-8). The intention was that applied voltage would induce current through the bars, and by measuring potential across the resistor in series with each bar, the current passing through it could be calculated.

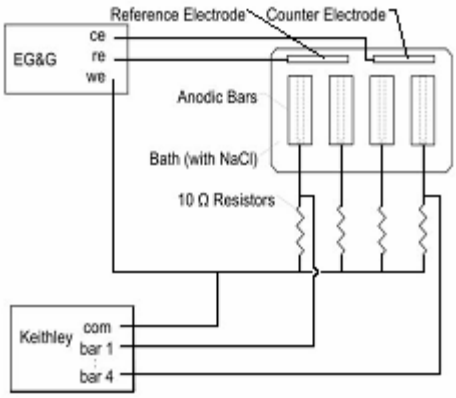

Figure 3-8: Test configuration for rapid diffusion test

A Keithley 2750 switching multimeter and Windows based PC running ExceLINX software were employed to record the voltage across each of the resistors. The leads of the multimeter were wired with the positive terminals connected at the rebar side of the resistors, and a common negative terminal connected to the working electrode lead of the 3-electrode potentiostat configuration.

3.4.iv Electrochemical Testing of Mortar Bars

For the rapid Cl^- diffusion test, the potentiostat was used to apply a potential of +100 mV vs. SCE to the common working electrode lead. The absolute anodic potential applied to each individual bar depended on the bar's corrosion potential, E_{corr}, the 10 Ω resistor, and the resistance of the mortar; the potential applied to individual bars would drop slightly if the corrosion current increased, since the resistor and mortar resistance added a potential drop proportional to the current running through it. For a highly passive bar, the applied potential was very close to +100 mV vs. SCE, but if a bar was actively corroding, the potential difference between the bar and reference electrode was diminished, ultimately limiting the corrosion rate; increased current resulted in a larger portion of the applied

voltage being consumed by the resistor. Each bar's E_{corr} also changed due to the applied current and electrochemical reactions occurring at the surface; if E_{corr} became more negative, the magnitude of the anodic potential applied to the bar would increase, and vice versa.

The multimeter system was programmed to record the voltage across every resistor at 5 minute intervals. These measurements were recorded to file in Excel, and then corrosion currents were calculated. These were plotted versus time in order detect any large increase in current. When a jump in current occurred for a particular bar, the wire could be disconnected from the common lead, so that the applied potential was removed and Cl^- diffusion slowed to rates governed by concentration gradient alone.

Prior to the application of potential, half cell potentials were recorded for all bars. Once the application of potential across all bars had been terminated, the potentiostat was used to perform LPR scans on each individual bar. These scans were similar to those described for pore solution testing; however, the potential was increased to ±15 mV from E_{corr} to account for the resistance of the mortar. The scan times were also increased to 90 s to allow more time for the current to stabilize; with higher voltage this was expected to take longer.

3.5 Characterization of Steels and Corrosion Products

Metallographic analysis was used to characterize the different grades, rolled diameters and surface treatments of the steels. Optical microscopy and scanning electron microscopy (SEM) including energy-dispersive x-ray spectroscopy (EDS) were used to observe the surface region morphology, metallography and compositions of the steels and any mill scale. X-ray powder diffraction (XRD) was employed to characterize corrosion products formed on 316LN.

3.5.i SEM and EDS of Cr Depleted Region and Rebar Surfaces

SEM and EDS were performed on the steels to determine the distribution of alloying elements in the surface region of the steels, and to investigate the existence and extent of a Cr-depleted region. This microscopy was performed in cooperation with Kyle Anders,

a fellow M.A.Sc. Candidate at the University of Waterloo, performing similar research on stainless steel rebar cast in concrete.

Cross-sectional samples of the as-rolled bars were prepared by mounting in resin, grinding, then polishing down to 0.05 μm alumina. In an attempt to magnify the thickness of the mill scale and/or depleted region (to allow easier analysis), the samples were mounted on a 65° angle, widening any surface regions by sectioning them diagonally.

Scanning electron microscopy (SEM) involves placing a sample in a vacuum chamber. Under high vacuum a high voltage beam of electrons is directed at the sample using electromagnets. Sensors are used to detect the scattered (secondary) electrons (low energy electrons knocked off out of atomic valences), the elastically scattered (backscattered) electrons (high energy incident electrons, elastically deflected back by the atomic nuclei), and the x-radiation emitted, as described below. The secondary electron image is visually presented on a monitor, showing the topography of the specimen. The backscattered electron image is also shown on a monitor, visually displaying any differences in average atomic number (or density) of different regions on the specimen's surface; this technique was valuable for identifying low-density oxides at the surface of the rebar.

When the incident electron beam creates a secondary electron by knocking an electron out of an inner valence of an atom, an electron from an outer valence level will drop to the lower energy valence to take its place. This releases an x-ray, which has energy equal to that lost by the electron. The differences in energy between electron levels are unique to each element, so x-rays are characteristic of the element from which they were emitted. Energy dispersive x-ray spectroscopy (EDS) is a technique in which the energy of the x-rays emitted is detected and the intensity of the x-rays is measured in order to provide a chemical analysis of the composition of the sample.

Analysis was performed using a JOEL® SEM with an INCA® EDS system attachment. The software used with this system allowed for EDS measurements to be taken along prescribed paths or areas and results appear as a spectrum on a PC. Chromium depletion

was investigated by taking EDS profiles of elements present along lines crossing the mill scale into the base material. Special attention was paid to levels of Fe, Cr, Ni, Mo and O.

3.5.ii Optical Microscopy of Rebar Surfaces and Cross-Sections

Optical microscopy was used to observe the grain structure and morphology near the surface of the bars. Attention was paid to differences between steels that were in pickled or as-rolled condition and different bar diameters.

Samples for optical microscopy were prepared by first cutting a 4-6 mm slice off the end of a bar, then cutting it into quarters. Two of these pieces were then mounted in resin as illustrated in Figure 3-9; one piece was mounted with the transverse cross-sectional face exposed, the other had a longitudinal cross-sectional face exposed, with the surface edge toward the center of the sample.

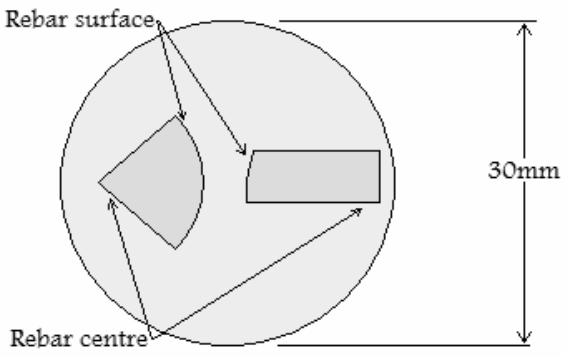

Figure 3-9: Layout of optical microscopy samples

Samples were wet ground with silicon carbide paper, and then polished with progressively finer alumina powder, down to 0.05 μm powder. Samples were etched with a solution containing two parts HCl to one part each of HNO_3 and H_2O in order to reveal the grain structure and any secondary phases such as carbon-rich $M_{23}C_6$ carbides. Submerging samples in the solution for ten minutes was determined to be sufficient to reveal the microstructure. Following the etch samples were rinsed with ethyl alcohol and distilled water to remove any residue from etching or other contaminants.

A metallographic microscope was used with a PC and ImagePro 4.5 software to observe the surfaces and to acquire digital images.

3.5.iii X-ray Powder Diffraction of Corrosion Products

Solid corrosion products generated during the corrosion testing were dried and ground to powder, then analysed using XRD.

XRD directs an x-ray at a sample of powder at a known angle and measures the diffracted beam at the equal angle of diffraction. The intensity of the beam is measured, and then plotted against angle of incidence/reflection. The beam reflects off atoms in different planes within a crystal, and when diffracted beams are in-phase, the x-rays are detected; when they are not in-phase destructive interference occurs; constructive interference occurs only when the distance between planes relates to the angle of incidence and the wavelength of the beam by a relation called Bragg's law (Figure 3-10):

$$n\lambda = 2d\sin\theta \tag{11}$$

where n is 1, 2, 3…, λ is the wavelength of the x-rays in nm, d is the interplanar spacing between planes in nm and θ is the angle of incidence/diffraction.

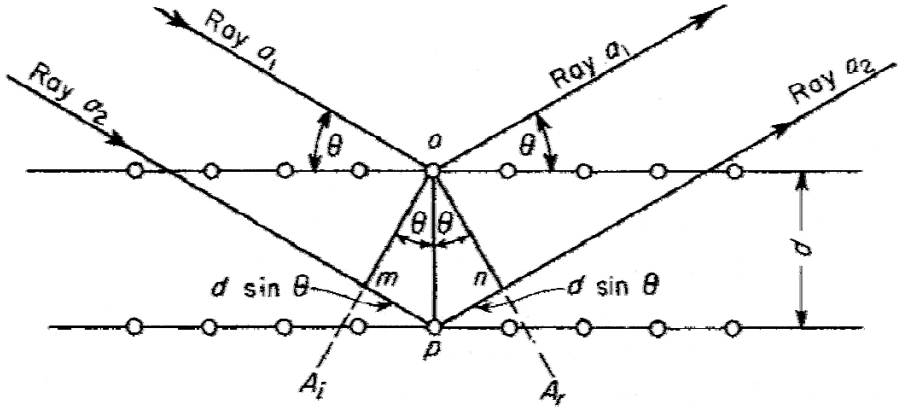

Figure 3-10: X-ray reflection relating to Bragg's law [61]

The right side of equation (11) is the extra distance a beam diffracted off a deeper plane will have to travel; constructive interference requires that waves be in phase, so this length must be an even number of wavelengths [61].

The distance between planes of a crystal is different for different compounds. The peaks in the diffraction spectrum (x-ray intensity versus angle) were compared to standard peaks for known compounds in order to identify those compounds present in the sample.

4 Experimental Results and Discussion

4.1 Cl^- Solubility of OPC Pore Solution

Pore solutions expressed using the procedure outlined by Barneyback and Diamond [56] typically gave 2-4 mL of solution for each cylinder. Pore solutions from 2-3 cylinders of each of the Cl^- addition levels described in Section 3.2 were analysed by titration.

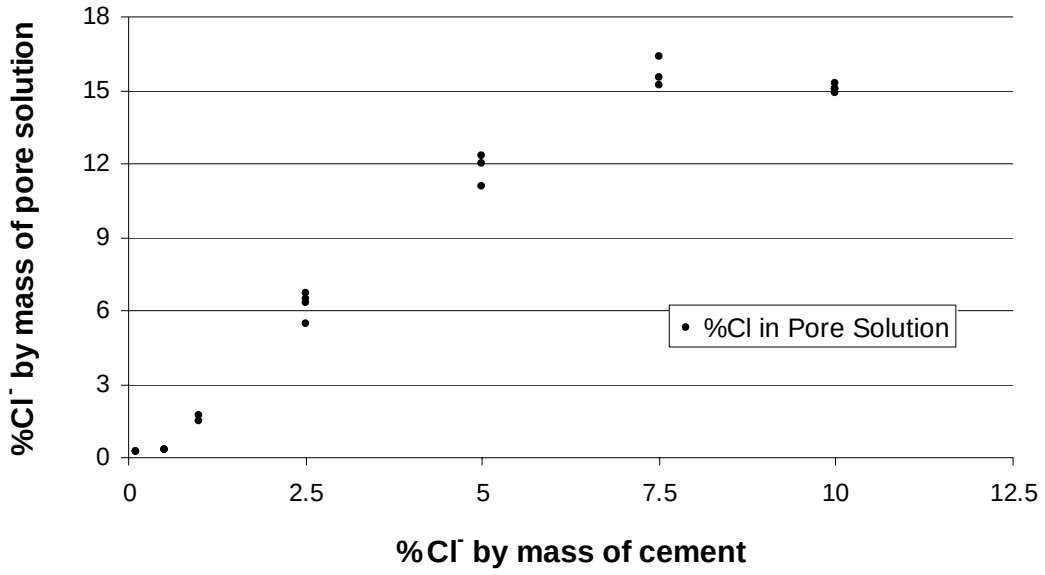

Figure 4-1: Chloride content of OPC pore solutions

Figure 4-1 presents these results graphically and shows an approximately linear relationship from 0.5 to 7.5% Cl^- by mass of cement and 0.3 to 16% Cl^- by mass of pore solution. The maximum concentration in the pore solution appears to be 16%, beyond which any additional NaCl added remains in solid form and does not affect the dissolved Cl^- level. These results were applied directly to the pore solution testing described in Section 3.3, with Cl^- additions continuing in increments to the observed maximum of 16%.

4.2 Measurement Techniques and Analysis

4.2.i Noise Reduction of Cyclic Polarization Scans

Cyclic polarization (CP) scans were obtained at Cl^- levels specified in Section 3.3.iii. A scan rate of 0.1 mV/s was used. Several scans taken at the specified rate had excessive noise when plotted, such as that shown in Figure 4-2.

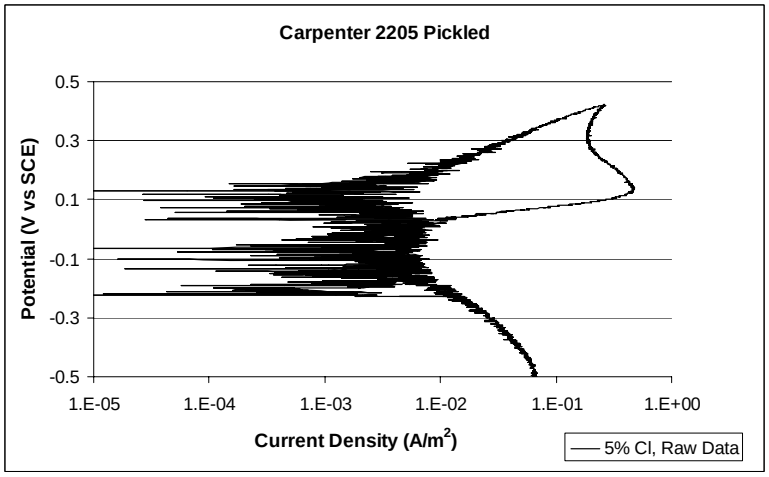

Figure 4-2: CP curve featuring low-current noise

The noise was more pronounced at the lower current region of the plot, so the log scale used for displaying current density was credited with exaggerating noise in low-current regions. Graphs with noise present were not useful for calculating Tafel constants, so the graphs were adjusted to reduce noise by using averages of the values graphed with those directly adjacent to them, following the equation:

$$i_{corr}'(t) = \sum_{n=-5}^{5} \frac{i_{corr}(t+n)}{11} \tag{12}$$

in which the current density (i_{corr}) for a time (t) is averaged with the five values preceding and following it; $i_{corr}'(t)$ is the adjusted value of $i_{corr}(t)$.

The resultant curve of applying the noise reduction to the data in Figure 4-2 is shown in Figure 4-3, where the curve, although not smooth, has more recognizable direction through areas of low current. When

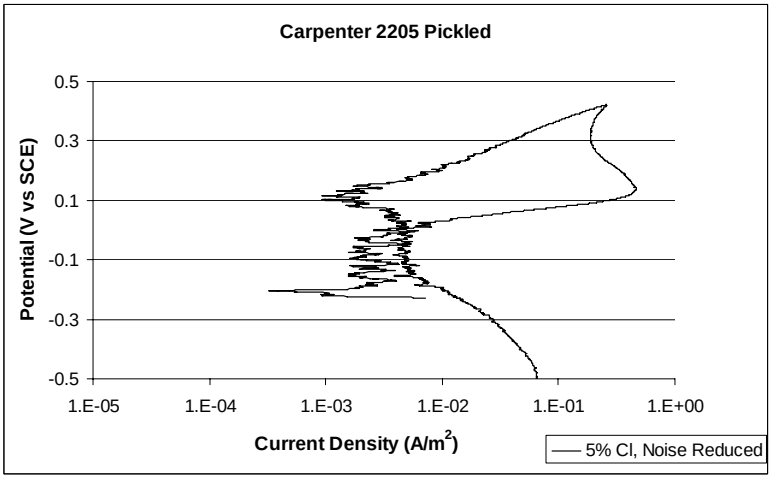

Figure 4-3: CP curve featuring noise reduction

equation (12) was applied to a curve in a continuously increasing or decreasing region, the averaged values tended to smooth the curve out, but for values near E_{corr}, or the reversal of the applied potential, where the direction of the curve reversed with respect to current, the peak was diminished; however, the peaks in the curves for which noise reduction was applied were pronounced enough that they are still identifiable following noise reduction.

4.2.ii Effect of Scan Rate on Cyclic Polarization Curves

Several possible causes of the noise observed in the CP scans were identified: the scan rate used might have been too high (leaving inadequate time for current to stabilize); there may have been electrical noise through the power supply (due to other equipment running on the same supply); the low-current resolution of the potentiostat may have been inadequate for accurate readings. Most scans were performed at night to avoid the effects of other electrical equipment on the same circuit, but this seemed to have little effect.

In order to observe the effect of reducing the scan rate, scans were taken at 0.03 mV/s and 0.01 mV/s to be compared to the scan taken at 0.1 mV/s, and are illustrated in Figure 4-4.

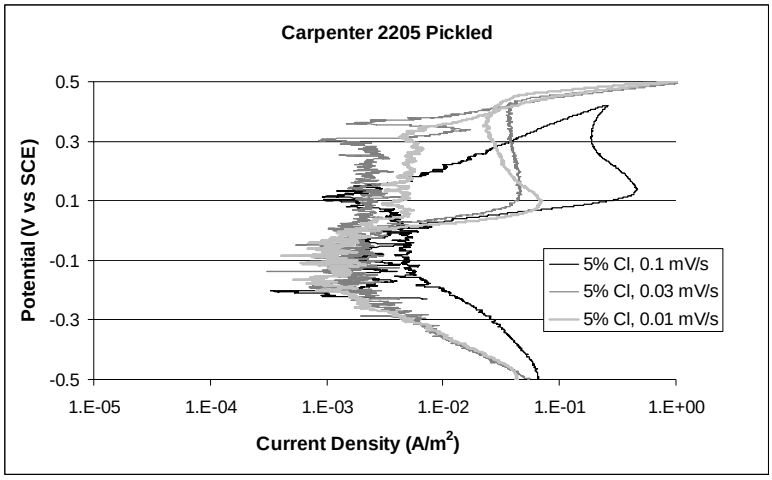

Figure 4-4: CP curves at various scan rates

The curves generated at 0.03 and 0.01 mV/s are similar through the entire scan, but the scan at 0.1 mV/s is significantly different, reaching currents an order of magnitude higher than those of the slower scans in the anodic region. The general trends, however, are comparable between the scans.

All three curves exhibited a region of constant current in the increasing anodic portion of the curve (vertical regions in Figure 4-4), emerging at approximately +100 mV vs. SCE. The slower scans reached constant current at slightly lower potentials than the faster

scan; the faster scan rate also exhibited a higher constant current, which was attributed to a protective film having more time to form at lower potentials in the slower scans. The constant current regions observed in Figure 4-4 are similar to passive regions for black steel, but are identified as semi-passive; passive corrosion currents are generally considered passive below 1 mA/m^2, while the constant currents observed were more than an order of magnitude higher than these.

The curves for the slower scans both showed the transpassive region emerging near +400 mV vs. SCE; the curve for 0.1 mV/s reversed at +420 mV, but the slope of the curve as it approached this peak is close to the slope of the curve descending from it, indicating that transpassive behaviour should be expected at a slightly more anodic potential.

As the curves descended from the anodic peaks, the slower scans reached lower currents more quickly, which is indicative of a thicker protective film and should be expected, as any films formed had more time to develop in these scans. All three scans reached a minimum current of approximately 2 mA/m^2, again indicating that the cause of the difference between the scans was the kinetics of the reactions; the behaviours observed occurred at similar potentials.

Overall, the three scans indicated that the scan rate of 0.1 mV/s was adequately slow to identify potentials of interest in the CP scans. Slower scan rates allow for a more stable scan and a more accurate depiction of the steady state behaviour of the steel for the prescribed potentials; however, these were avoided, as slower scans allow more time for any corrosion behaviour to permanently affect the surface of the steel sample being tested. In order to reduce damage caused by CP, scans continued to be taken at 0.1 mV/s.

The region of constant current in the increasingly anodic scan is usually referred to as the "passive" region, based on the low current density of black steel for this potential range; current densities in the passive region are ~1 mA/m^2 for black steel. Stainless steels are generally considered more corrosion resistant than black steel, so current densities for stainless were expected to be equal to or lower than values for black steel. The stainless steels exhibit much higher current densities in the passive region of the CP curves, ranging from 10 to 1000 mA/m^2. The higher current is attributed to the instability of

metal oxide films, particularly Cr_2O_3. Stainless steel forms a passive film under ambient conditions. Cr_2O_3 is unstable above -250 mV vs. SCE, which is near the half cell potentials of the steel in concrete, so Cr_2O_3 begins to break down as soon as the potential starts to rise.

4.2.iii Unstable Linear Polarization Resistance Scans

LPR scans were performed as described in Section 3.3.iv. On scans where the steady-state current dropped below 3×10^{-3} A/m^2 (or 10 μA through the potentiostat) using a PARStat 2263 potentiostat, the curves would become erratic and show zero measurements (Figure 4-5). The steady-state current in these scans was calculated as the average of the five last non-zero measurements taken.

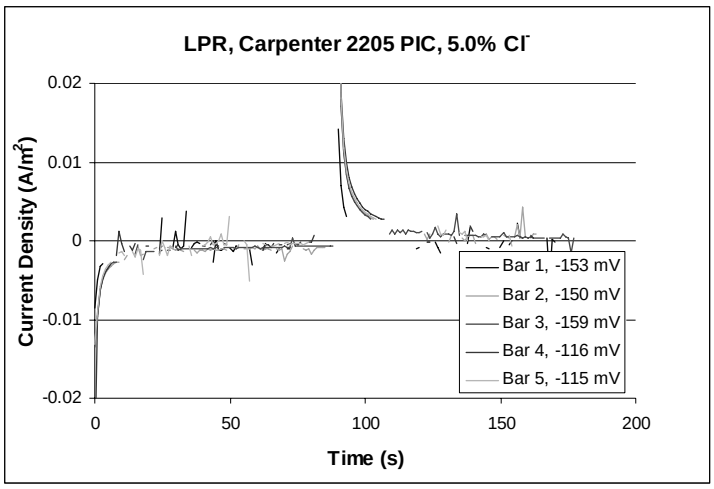

Figure 4-5: Unstable LPR curves generated by 2263 potentiostat

The unstable readings and zero measurement were unexpected, as the potentiostat is equipped to measure currents smaller than 200 nA. It was suspected that there was some malfunction with the switching of the detectors (ammeters) used by the potentiostat; when current became too low for one detector, the potentiostat should have switched to one for lower current levels.

Later measurements were taken using an EG&G 273A potentiostat. The EG&G was able to measure below 10 μA; however, during several scans there were also regions of oscillating currents, as seen in one of the curves in Figure 4-6

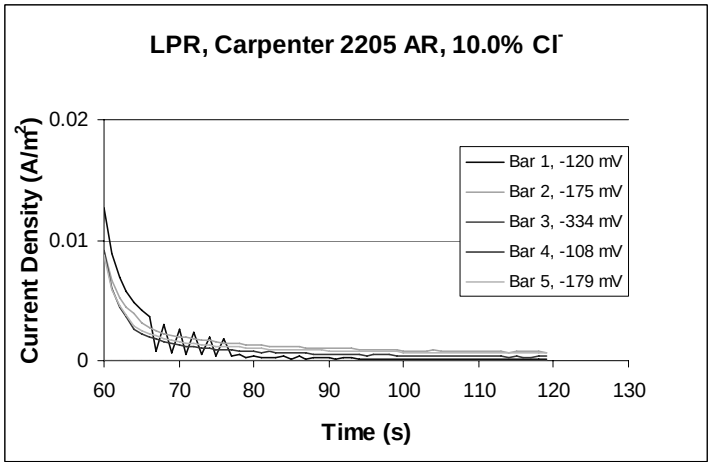

Figure 4-6: LPR curves featuring oscillating current levels

from 65 to 77 s. Below 65 s the curve follows the trend of the other curves; the upper values between 65 and 77 s appear to follow the trend prior to 65 s. After 78 seconds, the current seems to approach a non-zero steady state current; the lower values between 65 and 77 s appear to precede the trend after 77 s.

The potentiostat was designed to switch to a finer detector if the current becomes too low for the detector in use; it was expected that the different current levels observed between 65 and 77 s were due to alternating measurements between two detectors in the potentiostat which where out of calibration. The oscillating current levels began when the current reached 10 μA; the same current that was reached before the curves in Figure 4-6 became erratic, supporting the hypothesis that the detectors in the potentiostats are responsible for the unexpected behaviours.

4.3 Synthetic OPC Pore Solution Testing

4.3.i Half Cell Potentials

Half cell potentials were automatically recorded for each bar as a part of the LPR and CP scans. The averages of E_{corr} for each type of steel, taken from LPR scans, are plotted versus Cl^- concentration in Figure 4-7. The E_{corr} values for individual bars at each Cl^- concentration are given in Appendix B.

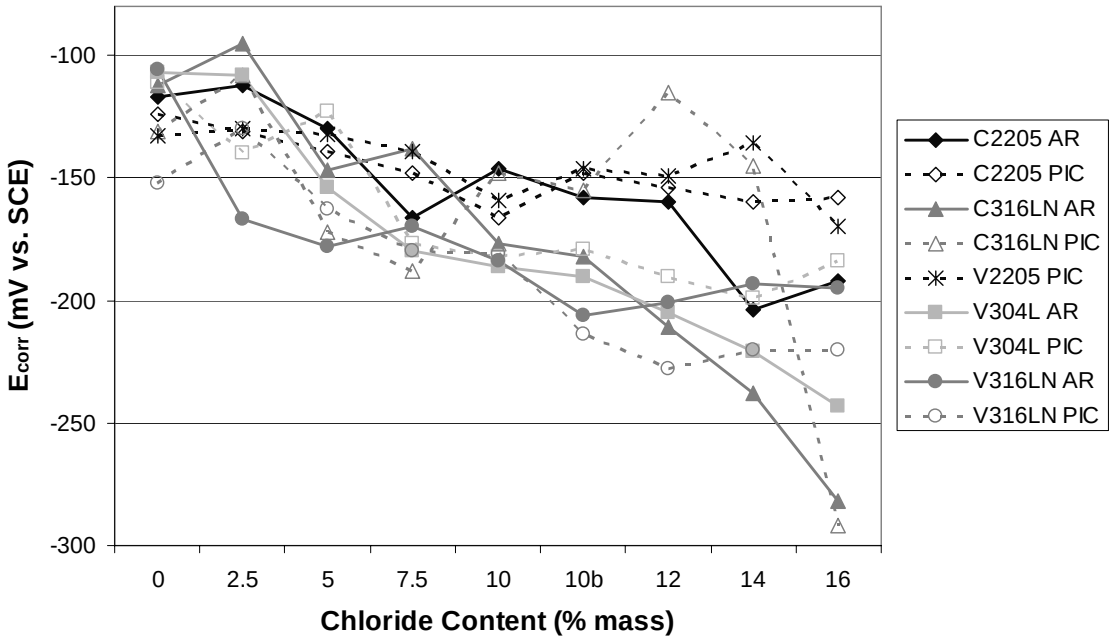

Figure 4-7: Half cell potentials of steels in OPC pore solution

Limited potentials were available from CP scans since these scans were only performed on one bar of each type and not at each Cl^- concentration, but there was good correlation between those obtained from CP scans and those measured during LPR for the respective steels. If LPR scans were performed on a bar closely following a CP scan, the steel often exhibited an abnormally low potential; therefore, these values were omitted from the averages for Figure 4-7. Two sets of data are presented for 10% Cl^-, because bars were

tested at 10% Cl^- in the original pore solutions as well as in replacement solutions, as described in Section 3.3.ii (10b denotes measurements taken in replacement solution).

A clear difference in the trend of E_{corr} seen here compared with that normally observed for black steel, is the gradual decrease as Cl^- content increases. Black steel will typically exhibit a steady E_{corr} until a Cl^- threshold is reached, at which point it drops sharply. The E_{corr} values for all of the stainless steels became steadily more negative from 0% to 16% Cl^-. The absence of a discrete drop in Figure 4-7 indicated that a gradual change was occurring in the surface film(s).

ASTM standard C876-91 [62] states that for black steel in concrete, an E_{corr} more negative than -275 mV vs. SCE indicates a 90% probability of active corrosion. This does not mean that the same is true for stainless rebar, because that value relates only to the stability of Fe-oxides (Fe_2O_3 and Fe_3O_4). Stainless steel can also be protected by Cr, Ni and in some cases Mo oxides, as well as mixed oxides (spinels) featuring Fe, Ni, and Cr. At the pH levels found in concrete and pore solution and in the absence of Cl^-, Cr_2O_3 film is stable between -275 and -1600 mV vs. SCE [57] and an iron-nickel spinel ($NiFe_2O_4$) is stable between +500 and -800 mV vs. SCE [57]; protective oxides are stable on stainless steels at potentials associated with the breakdown of passivity of Fe-oxides on black steel in the presence of Cl^-. Cr_2O_3 and $NiFe_2O_4$ may be stable to higher Cl^- levels than Fe-oxides, so a reduction in potential to -275 mV vs. SCE might only be accompanied by active corrosion for a specific minimum Cl^- content. The gradual decrease in E_{corr} may be an indication of a protective film becoming gradually less stable with rising Cl^- content.

The average E_{corr} values are all within approximately 50 mV of one another until 10% Cl^-, after which the values diverge; potentials of the 2205 steels are less negative, while the austenitic grades exhibited more of a drop at higher Cl^- levels.

At 16% Cl^-, E_{corr} of C316LN bars, as-rolled and pickled, dropped below -275 mV vs. SCE. The sudden drop observed in potentials of bars in both conditions suggests that some previously stable oxide, most likely $NiFe_2O_4$ [57], has become unstable due to the high Cl^- level at the surface. The new E_{corr} values were close to the expected stability

limit of Cr_2O_3 in this environment [57], so it is uncertain whether Cr_2O_3 has become stable or protective films have broken down to allow active corrosion to begin.

4.3.ii Microcell Corrosion Current Densities

The averages of the i_{corr} values for each type of steel, obtained from LPR scans, are plotted versus Cl^- concentration in Figure 4-8. Values of i_{corr} for individual bars of each grade at each Cl^- concentration are provided in Appendix C.

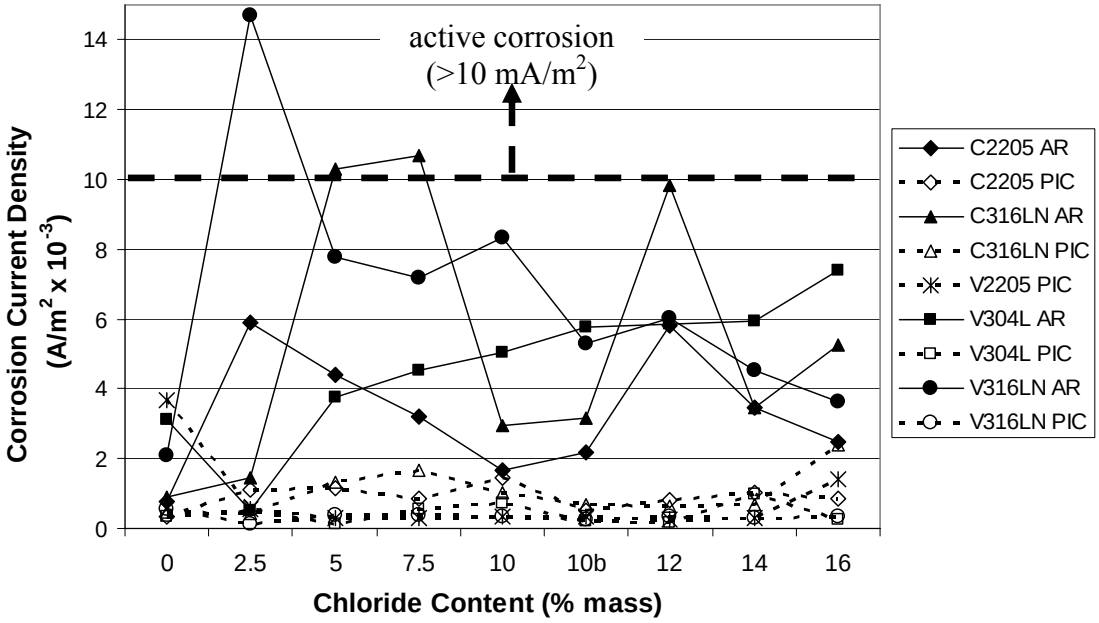

Figure 4-8: Corrosion current densities of steel in OPC pore solution

The average values of i_{corr} for the pickled steels remained below those of the as-rolled grades throughout the test and showed no appreciable increase with increasing Cl^- content. The general trend of i_{corr} values for the as-rolled steels is a slight increase in i_{corr} for increasing Cl^- content; however, the averaged current densities for the steels are very erratic. The fluctuations in the data are not unusual for corrosion studies; dissolution of ions and repassivation of the surface are random phenomena. Figure 4-8 reveals that all of the as-rolled grades exhibited poor corrosion resistance in the presence of chlorides

and V316LN AR even shows poor corrosion resistance with only 2.5% Cl^-. C2205 AR exhibited a minor spike in i_{corr} at 2.5% Cl^-, but its magnitude was much smaller than that of the 316LN steels, peaking at 6 mA/m^2, whereas the C316LN AR steel reached approximately 11 mA/m^2 at 7.5% Cl^-. V304LN AR did not see any drastic spikes; its corrosion current slowly increased from negligible levels in Cl-free solution to 8 mA/m^2 at 16% Cl^-.

The corrosion of the as-rolled 316LN steels at low Cl^- levels is attributed to attack of vulnerable points on the rebar surfaces. Once the as-rolled 316LN was tested from both suppliers at increasing Cl^- content, it was realized that only these two steels exhibited high corrosion currents at low Cl^- concentrations. Several possibilities were considered for this behaviour.

There may have been some form of black steel contamination on the surface of these steels. The high corrosion rates could represent the corrosion of black steel, and the declining rate the depletion of contaminants.

It was also discovered, in literature, that the sulphur content of the austenitic steels is of critical importance to pitting resistance [44,47,53]. Blanco et al. found that 316LN with 0.006% S had a pitting potential 150 mV lower than similar steel with 0.002% S. The V316LN has much higher sulphur content, 0.023%, while V304LN has only 0.009% S; the S content of C316LN was not known. The difference in S content could be responsible for the difference in the corrosion behaviour of the steels; 316LN exhibited sharp, erratic changes in corrosion rate, indicative of pitting and repassivation, while the 304LN exhibited a slowly increasing, steady corrosion rate.

The surfaces of the as-rolled bars did not appear to have been destroyed, or otherwise altered by Cl^- addition or due to the LPR scans. The mill scale was still present at the end of the testing and does not appear to have flaked off or expanded, and rust was not visible. Corrosion may become visible given sufficient time for products to form, or perhaps the corrosion currents measured are less severe than assumed, and currents are partially due to changes in the mill scale itself; some oxides formed on the stainless steels

during rolling may become unstable in pore fluid, and further oxidation of unstable oxides could affect the measured corrosion rates.

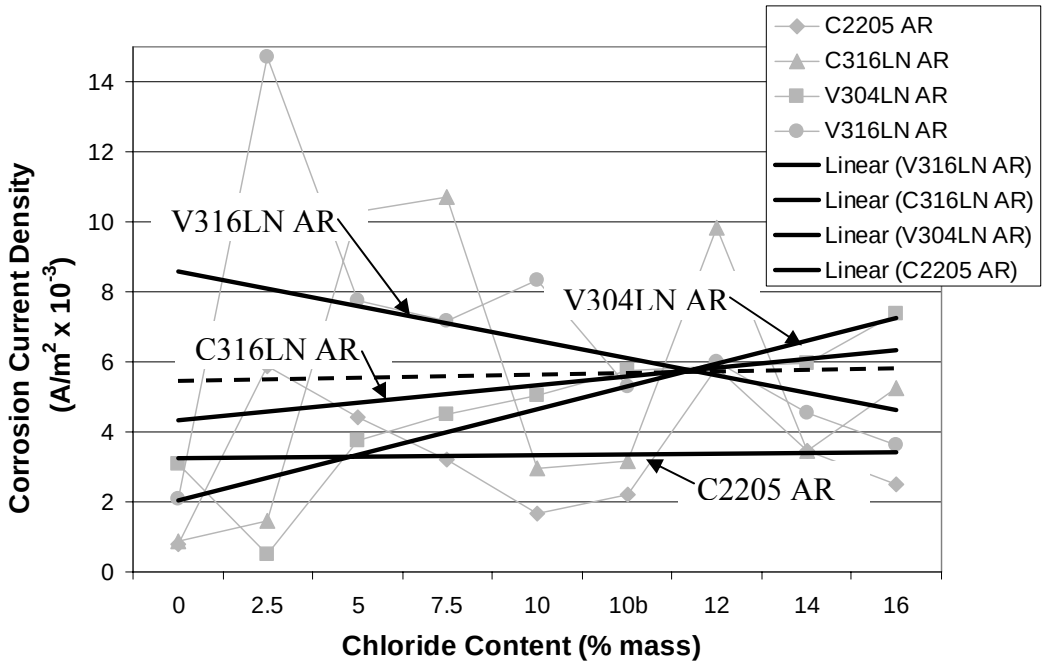

Figure 4-9: Trend lines of i_{corr} of as-rolled steels in OPC pore solution

Figure 4-9 shows the values of i_{corr} for the as-rolled steels with linear trend lines. With the exception of Valbruna 316LN, all of the as-rolled grades displayed at least a small increase in corrosion current density with increasing Cl^-. For V316LN, the trend line shows a decline in corrosion current from a particularly high i_{corr} value recorded at 2.5% Cl^-. The decline in the corrosion current of as-rolled V316LN while Cl^- levels increased, suggest that the corrosion rate is not directly related to Cl^- content for this steel, and that the rate is being limited by something, possibly slow formation of a new passive film, or exhaustion of surface contamination or of oxidizable species in the mill scale.

If the high value of i_{corr} is omitted from the curve for V316LN, the trend line has only a slight slope, similar to that of C2205 AR, increasing slowly at approximately 0.0055 A/m^2, denoted by a dashed line in Figure 4-9.

Overall, the corrosion current densities observed in all steels in both the as-rolled and pickled condition do not suggest active corrosion; they are lower than that of black steel in concrete with 2% Cl^-, typically above 0.01 A/m^2 (10 mA/m^2) [53], but less than an order of magnitude higher than the corrosion rates obtained for the stainless steels at 16% Cl^-.

Applying Equations (9) and (10) to the values of i_{corr} measured at 16% Cl^-, the maximum rate of material loss was 4.1 μm/year (C316LN AR) and the minimum was 0.13 μm/year (V304LN PIC).

Results of all of the LPR tests are summarized Table 4-1:

Table 4-1: Corrosion potentials and rates obtained using LPR

	i_{corr} (0% Cl^-)	i_{corr} (16% Cl^-)	Apparent Depth Loss	Crack Initiation	E_{corr} (0% Cl^-)	E_{corr} (16% Cl^-)
C2205 AR	0.699	1.21	0.94	26.6	-117	-192
C2205 PIC	0.884	1.12	0.87	28.7	-124	-158
C316LN AR	0.888	5.26	4.06	6.2	-112	-315
C316LN PIC	0.465	2.39	1.85	13.5	-131	-292
V2205 PIC	0.628	1.76	1.36	18.4	-133	-170
V304LN AR	1.72	3.80	2.94	8.5	-107	-254
V304LN PIC	0.631	0.17	0.13	192	-111	-207
V316LN AR	1.29	1.82	1.41	17.7	-106	-195
V316LN PIC	0.753	0.25	0.19	131.6	-152	-243

i_{corr} [mA/m^2], E_{corr} [mV vs. SCE], Depth Loss [μm/year], Crack Initiation [yrs][63]

For black steel it is generally considered that active corrosion exhibits a rate greater than 10 μm/year [64]; however, these values are for steel embedded in concrete. Corrosion rates measured in simulated pore solution have been found to be generally an order of magnitude higher than measurements made under the same conditions in concrete, so the rates determined through LPR testing of the stainless steels in pore solution indicate that, at least in the short term, they will not actively corrode when exposed to concentrated Cl^- in concrete.

As Cl^- levels approached 16%, E_{corr} values were still becoming more negative, approaching -275 mV vs. SCE, below which Cr_2O_3 may become stable. If Cr_2O_3 forms, the corrosion currents may be reduced. At 16% Cl^-, Carpenter 316LN (AR and PIC)

exhibited E_{corr} < -275 mV vs. SCE, so monitoring i_{corr} over time may identify repassivation due to Cr_2O_3.

4.3.iii Pitting Potentials

When an anodic potential is applied to an active/passive metal, the typical response is passive behaviour followed by the breakdown of passivity in the transpassive region. This behaviour was observed in the CP scan of C316LN AR at 0% Cl^-, as seen in Figure 4-10. When Cl^- ions were present at the steel's surface, corrosion occurred and current density continued to increase.

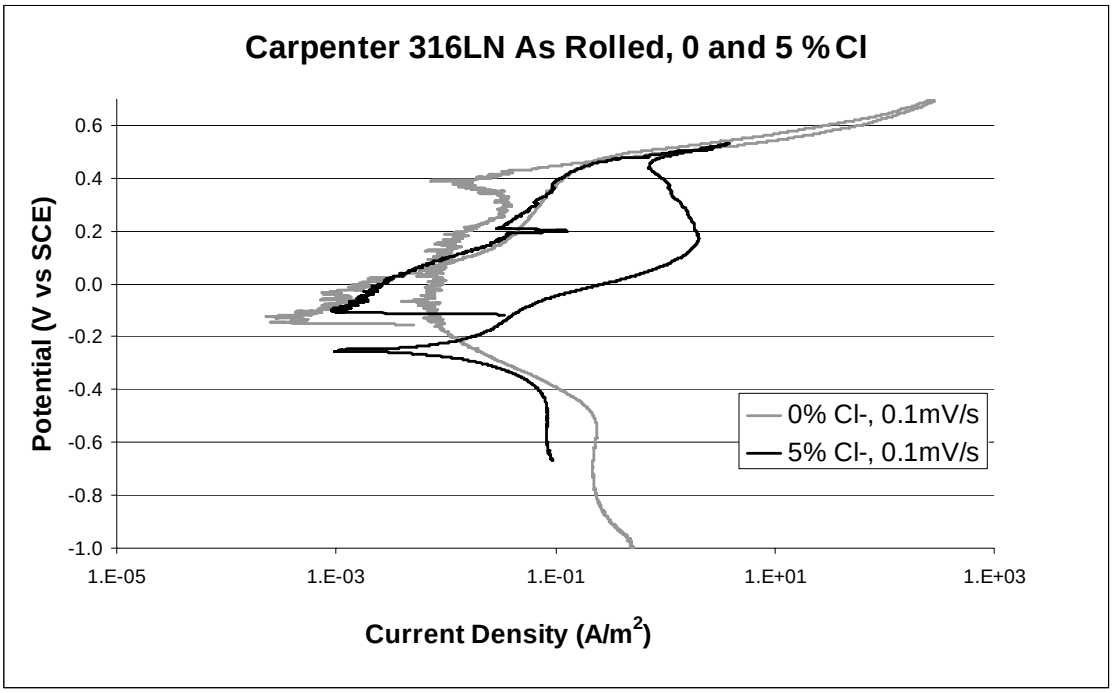

Figure 4-10: Cyclic polarization of C316LN AR with 0 and 5% Cl

Pitting/corrosion potentials of the steels were determined from the CP curves. Curves for all steels at different levels are located in Appendix D. From Figure 4-10, active corrosion occurs at 5% Cl^- within the transpassive region, indicated by the observation that the current suddenly increased as potential decreased below +500 mV vs. SCE. The corrosion was described as occurring in the transpassive region because the curve exhibited an increase in current similar to the 0% Cl^- curve; however, on the decreasing scan the current starts to decrease, but suddenly starts to increase again near +475 mV vs.

SCE. This can not be conclusively identified as pitting, since the current only rises by a factor of 3, as opposed to several orders of magnitude. However, it should be noted that the whole exposed area of the steel was used to calculate the corrosion current density whereas, if pitting is occurring, the corrosion current divided by only the area of the pits would give far higher corrosion rates.

Pitting occurred before the transpassive region was reached in solutions with both 10 and 16% Cl^-; at +400 and +225 mV vs. SCE respectively (Appendix D).

The values of apparent pitting potentials for all of the steels tested are tabulated in Table 4-2.

Table 4-2: Pitting potentials of stainless rebar (mV vs. SCE)

	0% Cl^-	5.0% Cl^-	7.5% Cl^-	10.0% Cl^-	16.0% Cl^-
C2205 AR	n/o	n/o	-	+550 mV	+500 mV
C2205 PIC	n/o	n/o	-	n/o	+500 mV
C316LN AR	n/o	+475 mV	-	+400 mV	+225 mV
C316LN PIC	n/o	n/o	-	n/o	n/o
V2205 PIC	n/o	n/o	-	+500 mV*	+475 mV*
V304LN AR	n/o	+200 mV	+200 mV	+200 mV	+200 mV
V304LN PIC	n/o	-	+350 mV*	+400 mV	+400 mV
V316LN AR	n/o	-	**	**	**
V316LN PIC	n/o	-	n/o	n/o	+500 mV

* Value uncertain due to unstable curve, ** General corrosion, n/o = not observed

The steels which exhibited the best resistance to pitting were as-rolled and pickled 2205, and pickled 316LN. This result corroborated the theory that adding Mo to the steels increases resistance to passivity breakdown and pitting [65,66,67]. C316LN showed more extensive pitting activity in the as-rolled condition, with the pitting potential decreasing to +225 mV vs. SCE at 16% Cl^-. V316LN AR did not show pitting, rather, general corrosion (or dissolution of protective films) at low potential. V304LN AR showed similar behaviour to V316LN AR, but at potentials approximately 150 mV higher.

V304LN showed poor resistance to pitting, especially in the as-rolled condition, which consistently showed pitting at +200 mV vs. SCE. V304LN PIC showed better pitting resistance than its as-rolled equivalent, but poorer resistance than C2205 AR.

These results suggest that 304LN would be at risk of pitting if used in the as-rolled condition; however, 316LN would be safe to use in the as-rolled condition because the likelihood of the steel being exposed to such anodic potentials is negligible. Moreover, the chloride concentration of 5% in solution is equivalent to ~2% by weight of cement, far higher than the threshold for black steel. 2205 seems to have excellent pitting resistance with its mill scale intact.

4.3.iv Corrosion Due to Cyclic Polarization Scans

In CP scans obtained for bars in synthetic pore solution at higher Cl^- levels, particularly those obtained for the as-rolled steels, severe corrosion was observed following the semi-passive behaviour. Corrosion was identified in CP curves by a rapid increase in current density. If corrosion currents stayed high until a significantly lower potential than that at which corrosion was initiated, the corrosion was expected to be pitting; lower potentials are required to repassivate and stop pitting, which creates local anodic sites with reduced pH, thus, different corrosion properties. When corrosion occurred and potential continued to increase, the corrosion current became very large, destroying the mill-scale and affecting the underlying material; bars damaged this way were excluded from future electrochemical tests, since the surfaces were no longer representative of the original rebar.

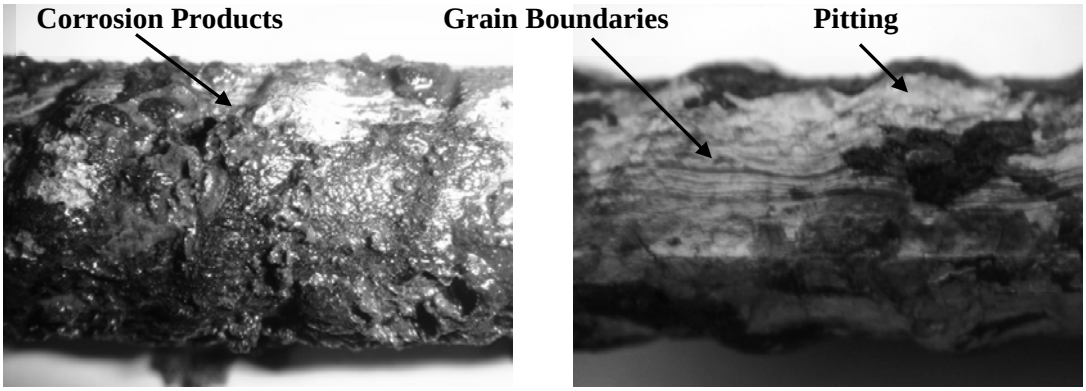

(a) (b)

Figure 4-11: Corroded surface of 16 mm diameter C316LN AR bar following cyclic polarization: (a) with corrosion products intact, (b) following mechanical removal of loose corrosion products

The first bar for which extensive damage occurred was a Carpenter 316LN bar in the as-rolled condition. Testing of the bar at 10% Cl^- caused extensive corrosion over the entire surface. Visual inspection of the bar following the scan revealed that the entire surface was covered in a thick crust of corrosion products, as illustrated in Figure 4-11. It was realized that the bar would not be useful for further electrochemical tests, as the surface had been permanently altered, so the bar was removed from the cell.

The majority of the corrosion on the surface of the bar was loosely adhered (Figure 4-11a) and could be removed by lightly brushing and rinsing with water. The surface of the steel below the corrosion product showed evidence of both pitting (top of rib in Figure 4-11b) and the grain direction of the steel, revealed by corrosion of grain boundaries. It is expected that the pitting was caused by localized disruption of the passive film by Cl^- ions, and the grain direction was revealed by subsequent attack of the high energy grain boundaries, which are more prone to corrosion.

4.4 Rapid Chloride Diffusion Testing

4.4.i Initial Corrosion Potentials of Mortar Covered Bars

The half cell potentials (E_{corr}) of the bars were recorded prior to the application of an anodic potential. The values recorded were in the range of -75 to -150 mV vs. SCE, which was typical of the bars in synthetic pore solution prior to the addition of Cl^-. An anodic potential of +100 mV vs. SCE was applied to all bars by means of the EG&G potentiostat.

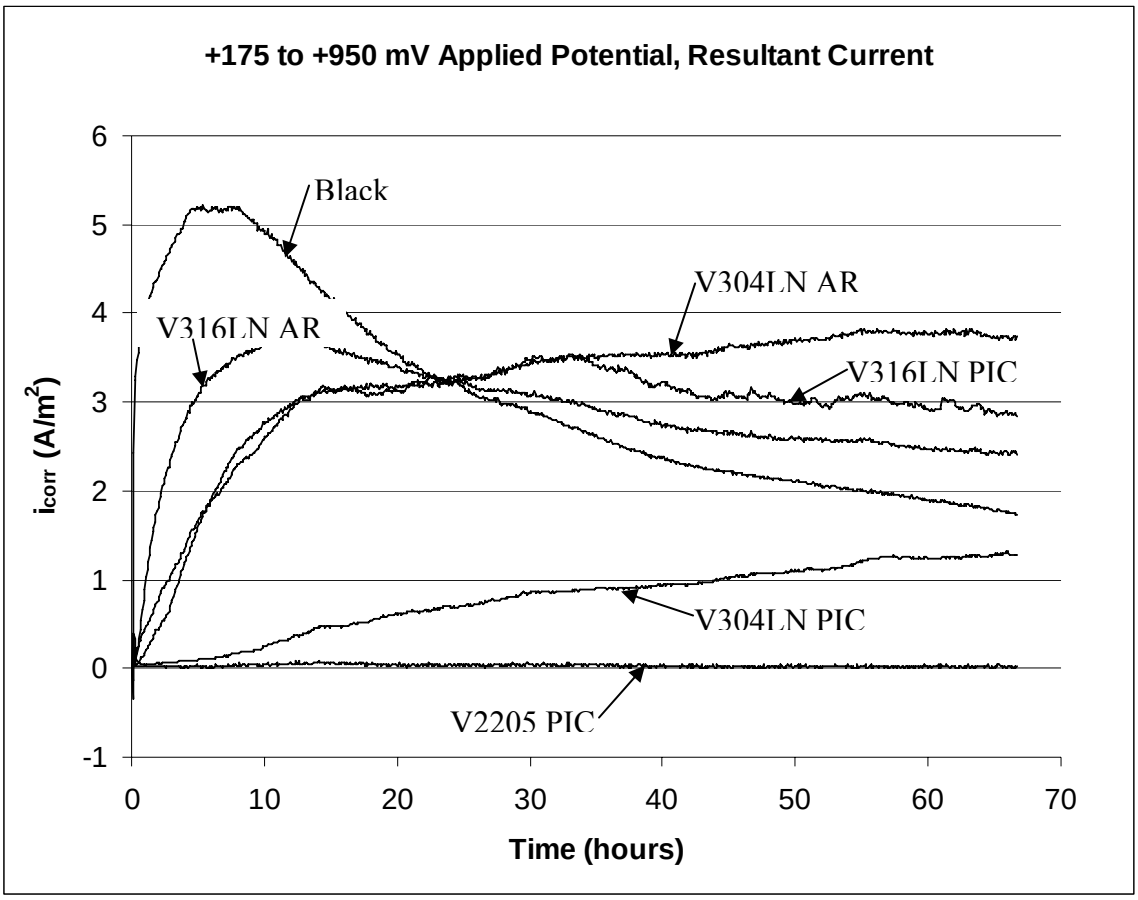

Figure 4-12: Net corrosion current densities of steels in OPC pore solution with 12% Cl^-, subject to applied potential of +100 mV vs. SCE

Figure 4-12 shows the average values of current density through four bars of each steel grade/surface. The current densities through the individual bars showed very good reproducibility. It was expected that the current densities through the steels would initially remain at passive levels (on the order of 10^{-3} A/m^2); however, shortly after the

potential was applied, the current densities of most bars quickly increased to highly active corrosion levels.

After three days all samples other than 2205 had suffered severe corrosion of the rebar. Rust products were observed on the outer surfaces of the mortar, and most mortar shells had been cracked at various locations along the exposed region of the underlying steel (Figure 4-13).

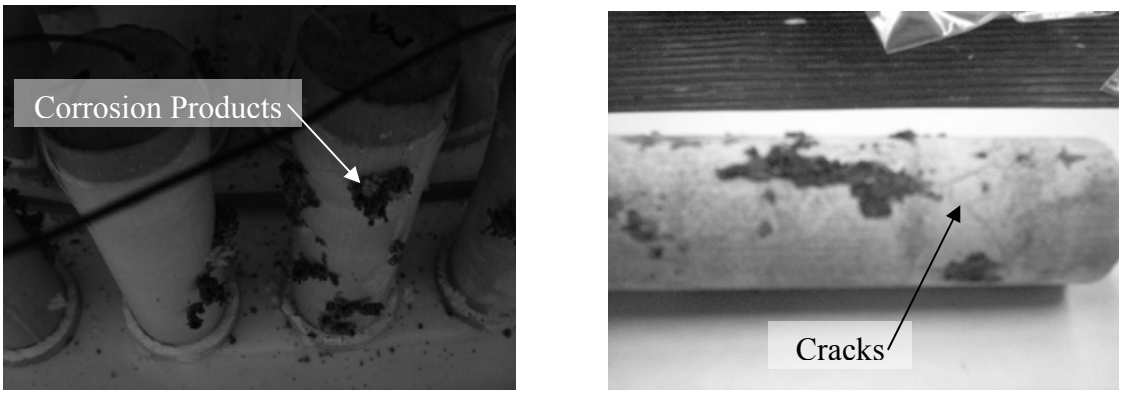

(a) (b)

Figure 4-13: Corrosion of mortar covered rebar under applied potential in high Cl- pore solution bath (a) in solution bath and (b) removed from solution

As illustrated in Figure 4-12, the current density increased first in the black steel bars, followed by as-rolled 316LN and 304LN, then pickled 316LN and 304LN; the 2205 pickled bars never reached active current density levels. The current densities of both the black steel and 316LN AR samples peaked quickly and then slowly declined. It would be reasonable to assume that sufficient Cl^- had reached the black steel, as much less is required for this steel.

The CP curve of Valbruna 316LN AR in pore solution (Appendix D) demonstrates that at +100 mV vs. SCE, the steel had a current density above 0.01 A/m^2 with no Cl^- present, which is considered active. The steel suffered severe general corrosion (~1 A/m^2) with 7.5% Cl^- or more present. Therefore, for the steel in mortar, regardless of Cl^- content, the applied voltage initiated the corrosion. Corrosion may have been increased by voids or microcracks in the mortar allowing Cl^- ions to the steel surfaces prematurely.

Information from the CP curves indicates that the applied potential was inappropriately high, and should either be reduced, or applied via an external electrode.

316LN PIC saw similar behaviour to 316LN AR, although it emerged one to two days later and to a lesser extent. 304LN AR was similar to 316LN PIC, but a decline was not clear in the graph, although it could have appeared if the test were to continue. 304LN PIC only saw a gradual increase in current while 2205 PIC did not increase at all.

One day after the application of anodic potential was terminated, LPR and half cell potential measurements were made on several bars of each steel grade (Table 4-3). Values of i_{corr} reflected the performance of the steels in Figure 4-12. The i_{corr} of 2205 was near the values of passive 2205 in pore solution. For 304LN PIC, which saw limited increase in current density in Figure 4-12, i_{corr} was an order of magnitude higher than levels observed in pore solution. All other steels showed i_{corr} values reflecting active corrosion (on the order of 10^{-2} to 10^{-1} A/m^2).

Table 4-3: LPR and half cell potentials after potential was applied

	i_{corr} (high)	i_{corr} (low)	E_{corr}
V2205 PIC	2.5	0.23	-834 to -844
V304LN AR	115	114	-831 to -861
V304LN PIC	15.8	9.9	-840 to -845
V316LN AR	36.1	23.9	-845
V316LN PIC	108	105	-845 to -850
Black	400	326	-846

i_{corr} (mA/m^2), E_{corr} (mV vs. SCE)

The half cell potentials of the steels following the application of potential were all -840 ±10 mV vs. SCE. The new values of E_{corr} are all near the hydrogen line on the Pourbaix diagram [4], indicative of oxygen depletion. The potentials were very close to each other (much closer than potentials in pore solution), also suggesting oxygen depletion, as differences in E_{corr} would be simply related to minor differences in pH.

Oxygen depletion at the rebar surface may be responsible for the outward growth of corrosion products at the surface of the mortar, as illustrated in Figure 4-13(a). Metallic ions liberated from the rebar surface would normally react with oxygen locally to form oxides or hydroxides; however, in the absence of oxygen, these ions needed to diffuse outward to the mortar surface, where oxygen was available.

Some of the corrosion products were collected from the mortar surface for the purpose of chemical analysis. Details of powder X-ray diffraction performed on corrosion products of 316LN AR are given in section 4.5.iii.

4.5 Characterization of Steels and Corrosion Products

4.5.i SEM and EDS of Cr-Depleted Region at Rebar Surfaces

Valbruna 304LN AR

The first SEM/EDS analyses were performed at the edge of a cross-section of as-rolled Valbruna 304LN. Several scans were taken at various locations along the rebar surface. Figure 4-14 shows one of the images taken, with an EDS profile of six points along a length of approximately 0.22 μm (accounting for magnification by the angle of the cross-section).

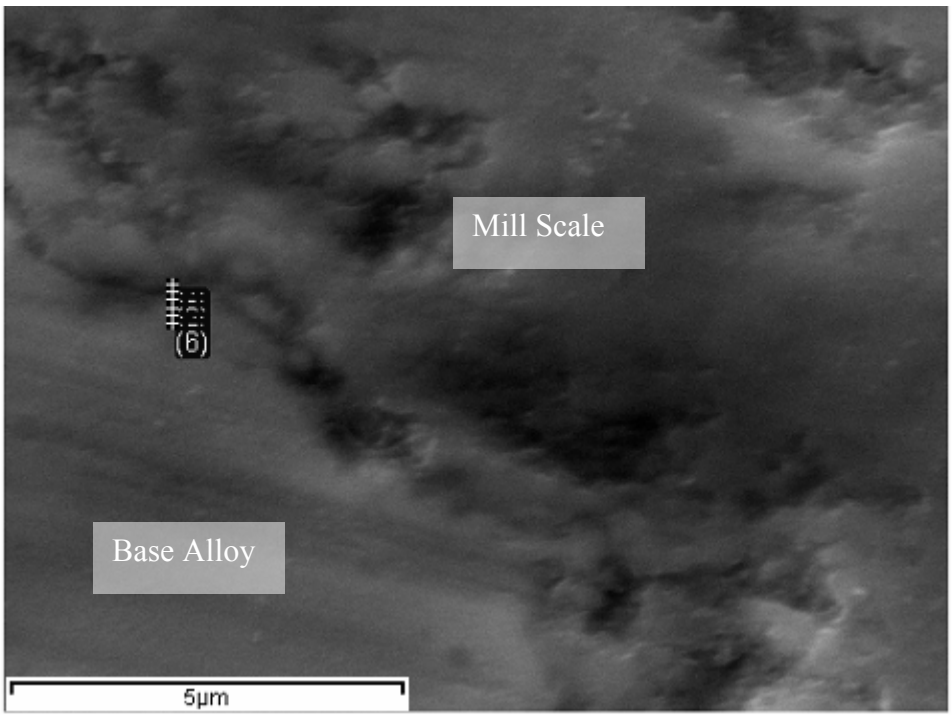

Figure 4-14: Secondary electron SEM image and location of EDS analysis of Valbruna 304LN as-rolled surface region of a cross-section

The distribution of elements along the profile shown in Figure 4-14 are shown graphically in Figure 4-15. This graph shows the weight percentage of the metallic elements with respect to Fe, Cr and Ni, excluding oxygen from that calculation; oxygen is only shown as a reference to indicate where the oxide phases exist. The positions indicated in the graph are taken from the mill scale inwards into the base alloy.

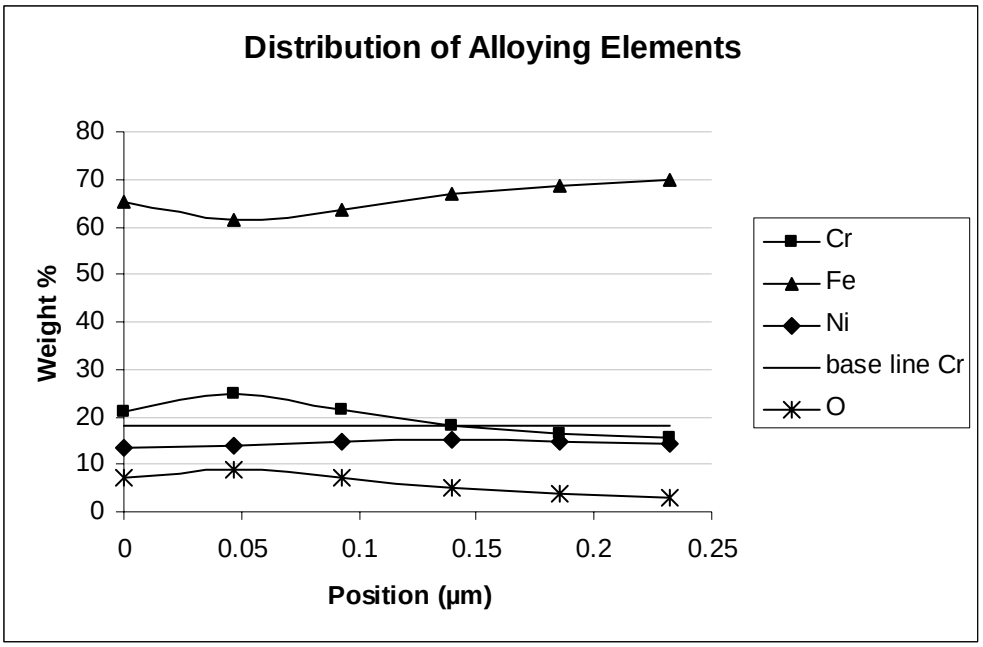

Figure 4-15: EDS analysis of points shown in Fig. 4-14 image of Valbruna 304LN

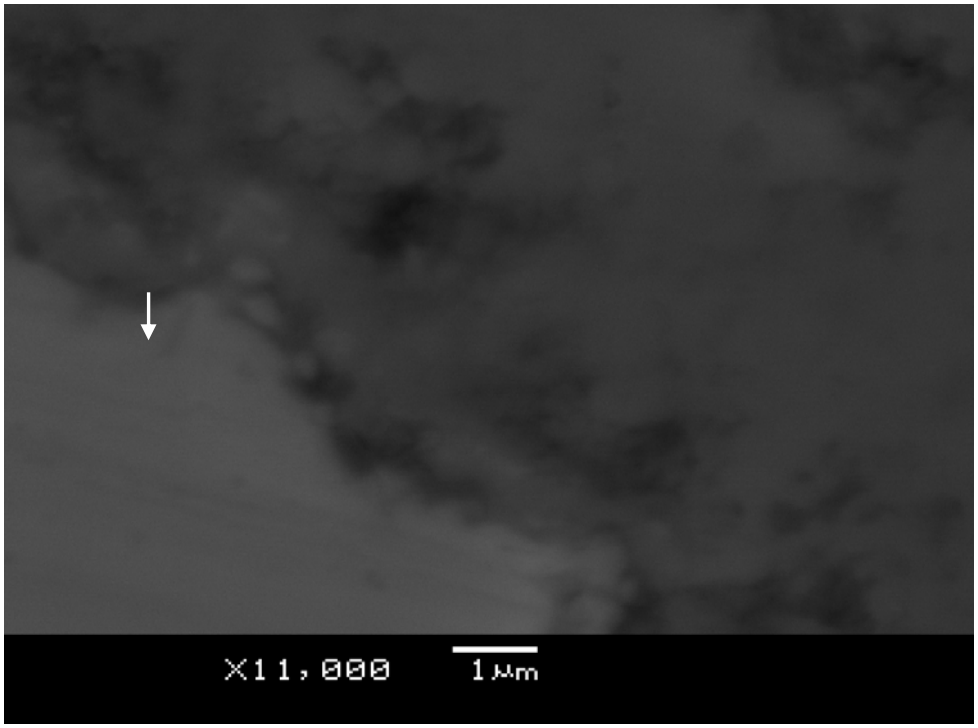

Figure 4-16: Back scattered electron image of same area of Valbruna 304LN as in Fig. 4-14

In the second point measured, the oxide seems to be changing from an iron-rich oxide to a more chromium-rich oxide. As oxygen content dropped, the Cr also dropped to 15.5

wt%, compared to 18 wt% in the base alloy, indicating some "Cr-depletion"; however, this is not certain, as some oxygen still remained and the oxide is not uniform at the surface.

Figure 4-16 is the backscattered image (BSE) of Figure 4-14. A slightly darker region can be observed near the end of where the EDS profile was recorded (shown by a white arrow in Figure 4-16), indicating a low density region which is likely to be more oxide and possibly accounts for the low Cr content.

A second SEM scan of Valbruna 304LN was taken, with an EDS profile covering a larger distance (approximately 0.75 µm) and at a point along the surface which exhibited a more uniform oxide scale (Figure 4-17).

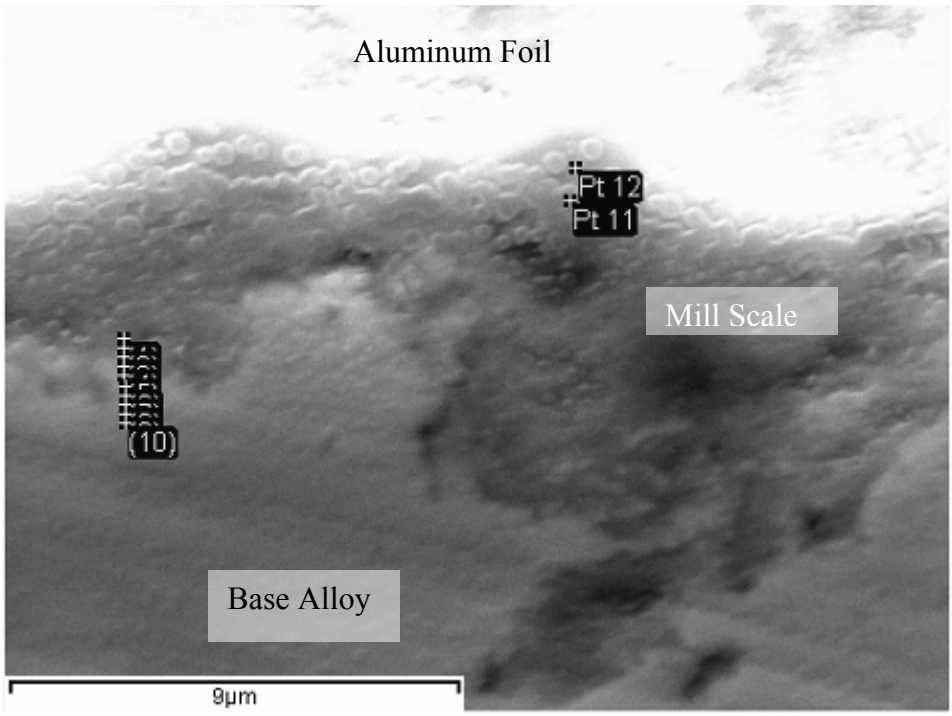

Figure 4-17: Secondary electron image and EDS analysis points of a second area of the metal/oxide interface region of Valbruna 304LN as-rolled cross-section

Figure 4-18 shows the distribution of metallic elements determined by the EDS analysis, similar to Figure 4-15. This graph gives profiles of the metallic elements from the oxide layer through to the base alloy, as Fe, Cr and Ni reach their base alloy levels (~70% Fe, 18% Cr, 8% Ni) in the final three points, while oxygen reaches negligible levels.

In this scan, Cr-depletion could be observed in the low Cr level around 0.45 μm in Figure 4-18, for a depth of approximately 0.2 μm. The lowest Cr content measured is 14.2 wt% Cr, which is 4% lower than the base alloy; however, this Cr-depletion is not considered to be detrimental, as the alloy remains above 12% Cr, which is widely considered to be the minimum Cr-content for passivation of stainless steels.

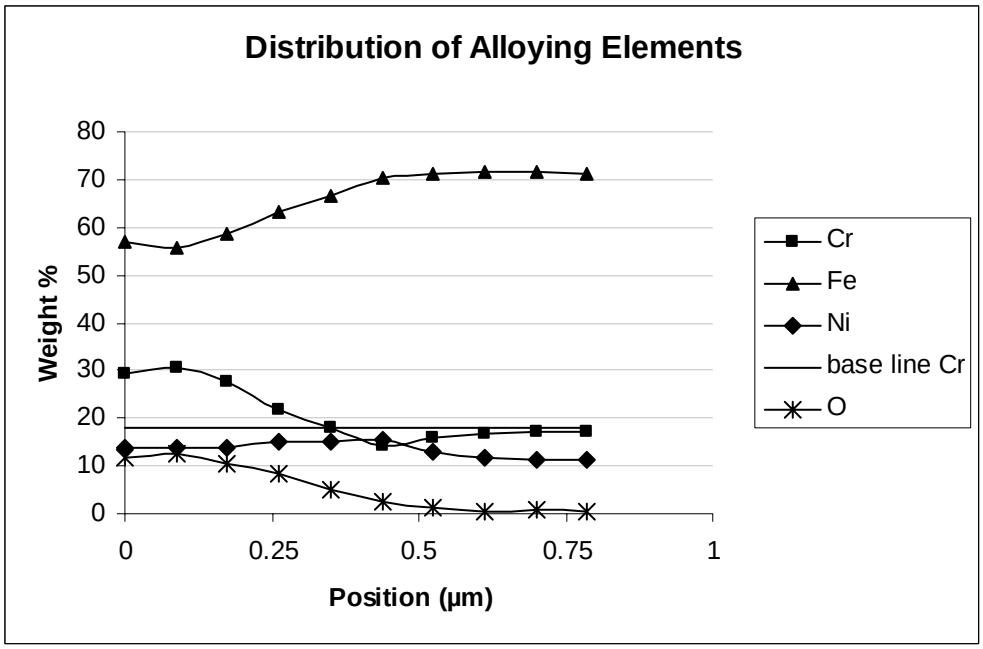

Figure 4-18: EDS analysis of points shown in Fig. 4-17 image of Valbruna 304LN

EDS analysis was also performed for two additional points in the oxide scale (Pt 11 and Pt 12 in Figure 4-17). Circular patterns could be seen in the outer mill scale, EDS was taken on one of the circles (Pt 11) as well as between them (Pt 12) in order to determine if there was a difference in the composition, or if the observed circular patterns were simply due to the morphology of the oxide or a sample preparation artefact. The compositions of these points were similar; both locations were oxides with high levels of iron and less than 10% Cr. This indicated that the pattern seen in the surface is due to the morphology of the outer Fe-rich oxide or an artefact.

The interface between the mill scale and steel is very rough and inconsistent. The position of the interface varies by about 4.2 μm with respect to the edge of the rebar in

each of the images taken. The thickness of the mill scale in Figure 4-17 varies from 1.3 to 4.2 μm.

Carpenter 2205 AR

The mill scale and the underlying surface of as rolled Carpenter 2205 were rough, similar to those observed on Valbruna 304LN. Figure 4-19 shows a secondary electron image of C2205 AR, taken at a lower magnification than those taken on V304LN AR. The outer mill scale was 2-4 μm, similar to V304LN; however, large, finger-like oxide areas extended up to 15 μm into the steel. The large areas of oxides (darker streaks in Figure 4-19) seemed to be following specific orientations within the metal. It is possible that the oxidation grew inward through one of the two phases of 2205 while the other phase remained a metal, or that mill scale formed early in the rolling process compressed into the metal by subsequent rolling.

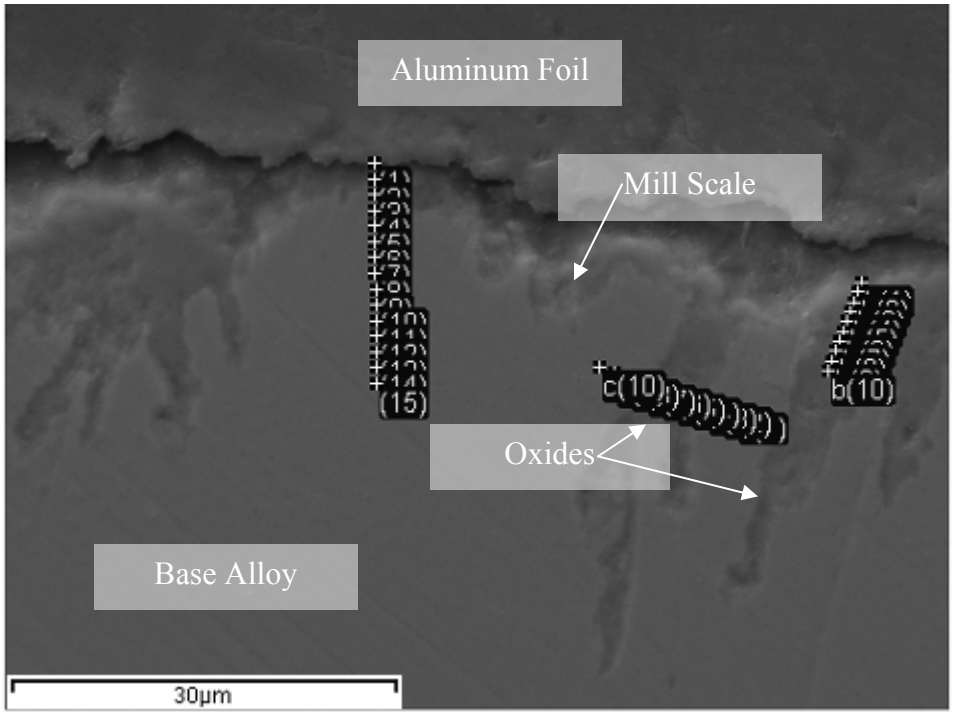

Figure 4-19: Secondary electron SEM image and location of EDS analysis of Carpenter 2205 as-rolled surface region of a cross-section

Figure 4-20 gives the distribution of metallic elements along the longer, vertical profile in Figure 4-19. The scale was much larger than the profiles of V304LN, but local Cr-

depletion near the surface was not observed. The profile covered approximately 8 µm and three regions of minor Cr-depletion can be seen. The appearance of multiple Cr-depleted regions may be detection of the different phases of the duplex steel.

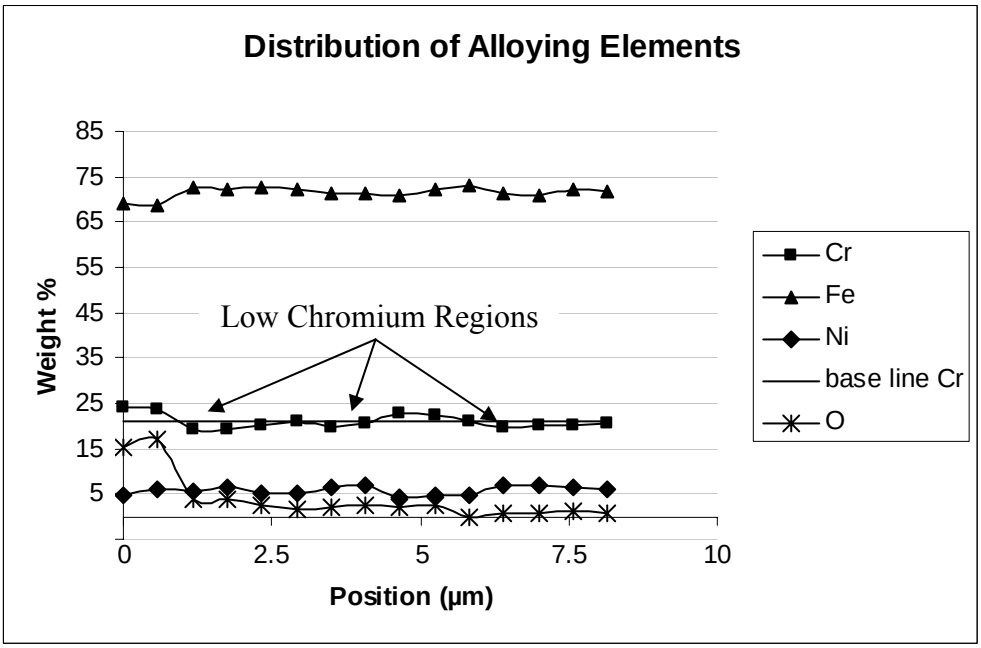

Figure 4-20: EDS analysis of points shown in Fig. 4-19 image of Carpenter 2205

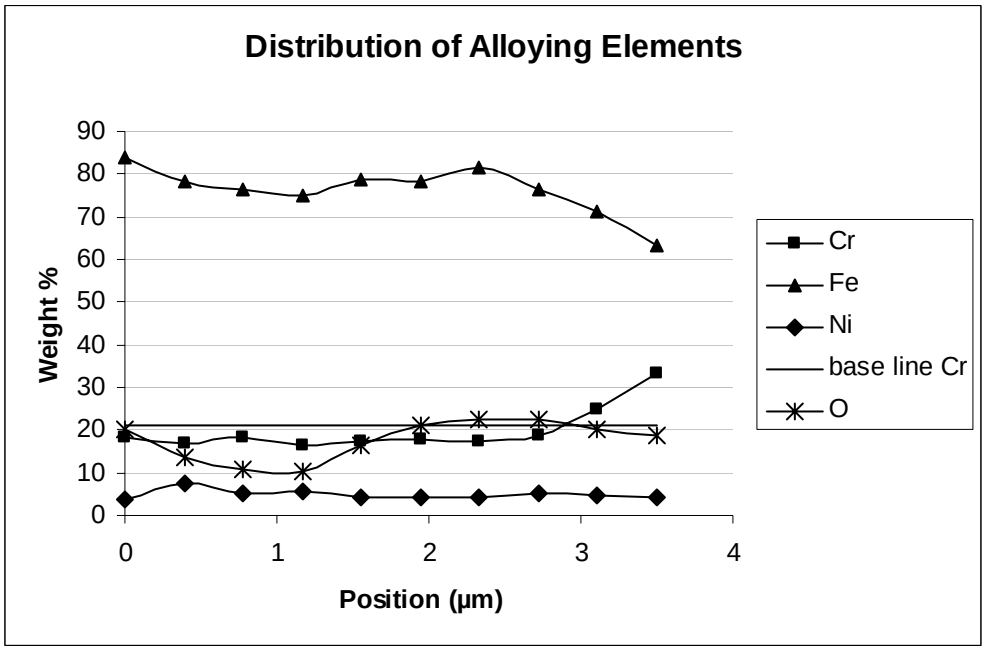

Figure 4-21: EDS analysis of points shown in profile "b" of Fig. 4-19 image of Carpenter 2205

Further EDS analysis was performed on one of the oxide patches observed in Figure 4-19, denoted as profile "b". Figure 4-21 gives the distribution of metallic elements, which scanned into the rebar from the mill scale, remaining in the oxide patch.

The metallic contents of the oxide in the outer 2.5 μm vary between 75 and 83% Fe, and then drop to ~62% at 3.5 μm. Chromium content rises from ~18% in the first 2.5 μm to ~35% Cr at 3.5 μm. It is believed that the 2.5 μm to 3.5 μm region is a transition from a region comprised mostly of Fe-oxides to a region of mostly Cr-oxides. This may be evidence of a Cr-rich oxide region between the Fe-rich oxide and base alloy, as shown at the surface of V304LN AR in Figures 4-15 and 4-18.

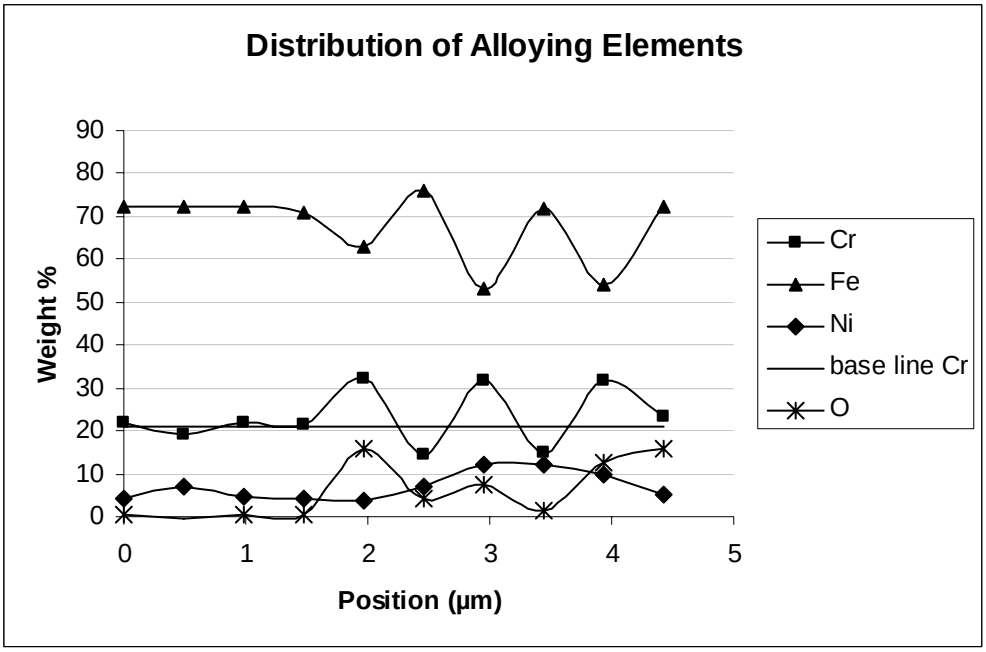

Figure 4-22: EDS analysis of points shown in profile "C" of Fig. 4-19 image of Carpenter 2205

A third EDS profile was taken on the C2205 AR sample. This scan traversed one of the oxide patches from Figure 4-19; the distribution of oxygen and the metallic oxides are shown in Figure 4-22. For the first 1.5 μm of the scan, oxygen was negligible and the levels of the alloy elements were near those of the base alloy. From 1.5 to 4.5 μm, the levels of Fe and Cr increased and decreased inversely to each other; at 4, 6 and 8 μm the Cr and oxygen content were high. At the points between the Cr-rich oxides (2.5 and 3.5

μm in Figure 4-22), Cr and oxygen both decrease, with Cr dropping to 15%, much lower than the nominal composition of 22%.

The Cr-rich oxides in 4-22 have over 30% Cr by wt. and less than 70% Fe, similar to the Cr-rich oxide in Figure 4-21. The regions of the curve between these seemed to be Cr-depleted alloy, rather than Fe-rich oxide, since oxygen content is relatively low at these points. Another possible explanation for the composition in Figure 4-22 would be mixing of Cr_2O_3 into metallic iron, as the proportion of Cr to O is similar between the low and high points.

It should be noted that for measurements with oxygen content below 2%, oxygen was considered negligible. The incident electron beam in SEM energizes a small amount of material around the point of incidence. EDS detects x-ray emissions from all of the material energized. If some oxide exists immediately below or adjacent to base alloy on the surface, EDS will also detect the oxygen and report levels lower than in pure oxide and higher than in the base alloy.

Valbruna 316LN AR

The mill scale on V316LN AR was 5-7.5 μm thick, 2-3 μm thicker than the other two grades; this difference may simply be coincidental because the thickness and morphologies of the mill scales on all steels were inconsistent and highly irregular, therefore the depth of the mill scale may differ at different regions of the surface. Similar to the 304LN AR steel, the mill scale is a disorganized mixture of Cr and Fe-rich oxides. Figure 4-23 shows a secondary electron image of the steel, with the mill scale covering most of the image. Figure 4-24 is the backscattered image of the SEM image in Figure 4-23. The lighter (denser) regions contain less oxygen; the darker regions, believed to be oxides, are of varying shades indicating varying compositions with the lighter regions being denser, Fe-rich oxide regions.

EDS analysis was performed on a number of different locations in order to determine whether the oxide contains primarily Cr or Fe, or a mixture of the two. Spectra 1, 5 and 7 have O content near 1% by mass and approximately 16% Cr and 14-15% Ni, which is near the nominal composition for the alloy. Spectra 3 and 6 were Fe-rich oxides, while

Spectrum 4 was Cr-rich oxide. The trend for the oxide seemed to be that layers of the different oxides exist, with higher Cr in the regions appearing darker in the BSE image.

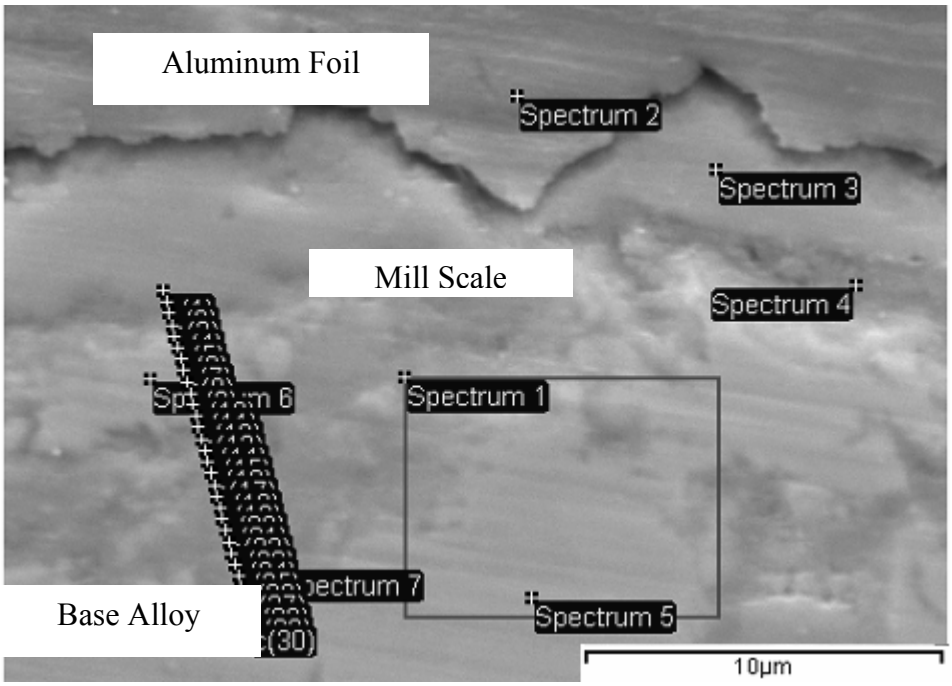

Figure 4-23: Secondary electron SEM image and location of EDS analysis of Valbruna 316LN as-rolled surface region of a cross-section

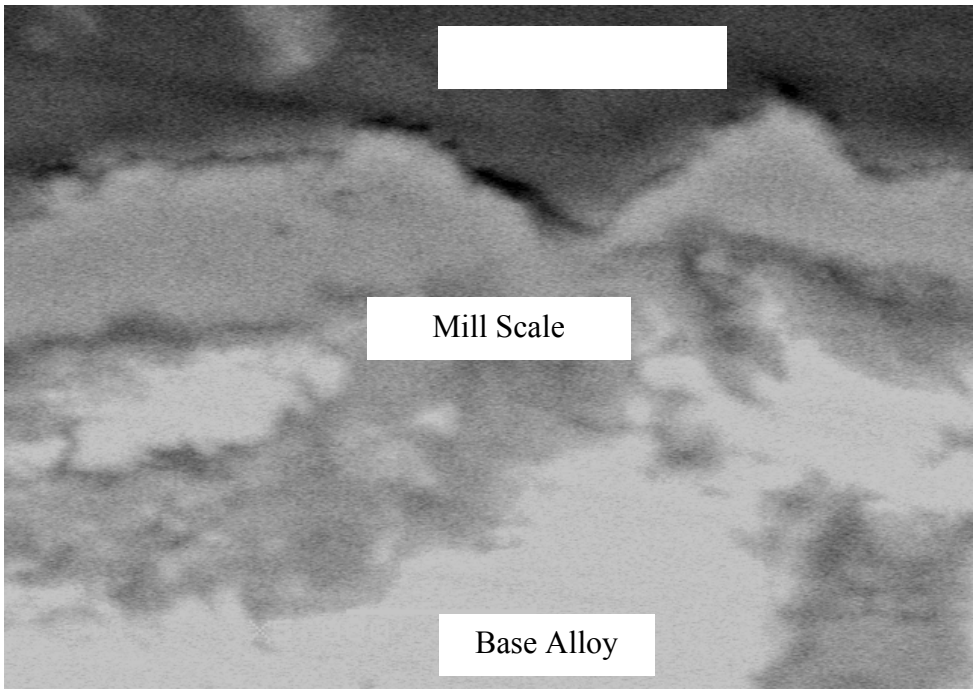

Figure 4-24: BSE image of SEM image of Valbruna 316LN in Fig. 4-23

Figure 4-25 gives the distribution of metallic elements along the profile shown in Figure 4-23. It appears that Cr is high for most of the profile, other than the lightly shaded area in the SEM image around Spectrum 6, which is a high Fe oxide. Cr decreased to 13.9% at the end of the scan when oxygen dropped off and the base alloy began.

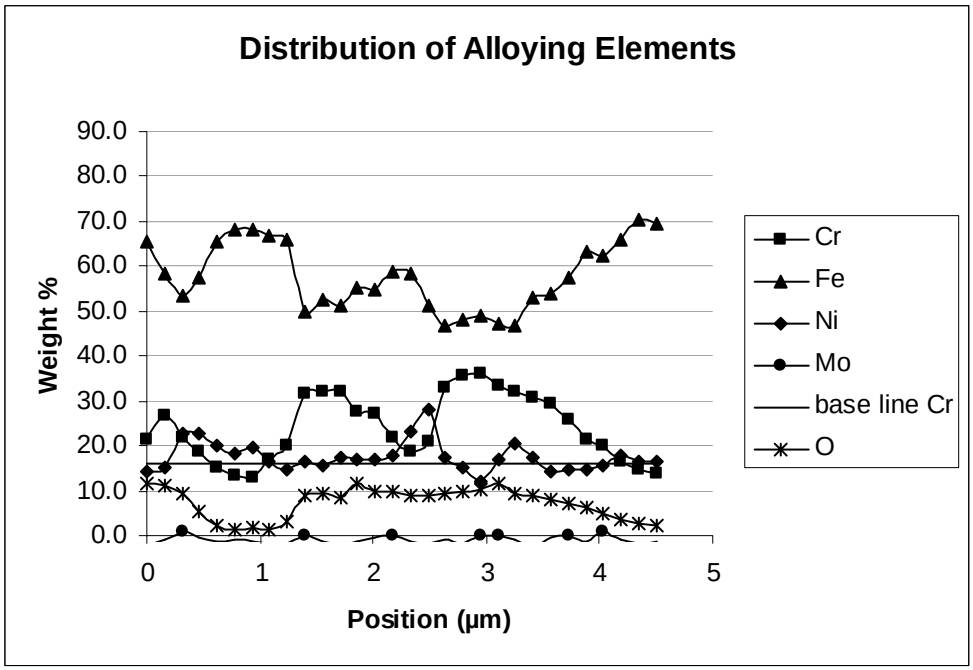

Figure 4-25: EDS analysis of points shown in Fig. 4-23 image of Valbruna 316LN

The Cr content in the profile seemed to fluctuate between higher and lower contents, with low Cr not only at the 4.5 µm point, but also at 1 µm (12.9% Cr) and near 2.3 µm (18.7% Cr). 1 µm and 4.5 µm show very little oxygen, and may simply be Cr depleted alloy.

Between 1.4 and 3 µm, the oxygen content is almost constant, but Fe changes from 50% at 1.4 µm, increasing to 59% at 2.3 µm, then decreasing to 49% at 3.3 µm. Over the same range, Cr changes from 32% at 1.4 µm, decreasing to 19% at 2.3 µm, then increasing to 36% at 3.3 µm. This supports the growth mechanism proposed by Bombara [36] in the literature, where the mill scale is composed of alternating Cr and Fe-rich oxides.

Further EDS analysis was performed near where the base alloy began at the bottom of the SEM image. This was done on a fine scale in order to detect any Cr-depletion, as the low

point of 13.9% Cr was seen in the first profile, lower than the specified 16-18% for the grade. The additional EDS profiles taken at the transition from oxide to base alloy never detected Cr levels below 14% by mass; this Cr depletion, which is about 0.4 μm thick, is not seen as threatening to the steel or any structure in which it is placed.

Pfeiffer [63] published a literature review in which models for corrosion initiated concrete cracking were compared. A simplified model was proposed in which cracking occurs once 25 μm depth loss to corrosion has occurred for black steel. Assuming that the densities of the steel and oxides are similar between black and stainless steel, this would allow for complete dissolution of these Cr-depleted regions well before enough metal has been lost to initiate cracking.

Of the three different steels inspected with SEM and EDS, none seemed to suffer significant Cr-depletion. While Cr-depletion was observed in all three as-rolled steels, as shown in Table 4-4, it was limited to 2-4% less Cr than specified, well above 12%, which is considered the minimum for a stainless steel. In conventional terms, stainless steels are those containing more than 12% Cr, and the minimum amount found in the steels inspected was 13.9% Cr.

Table 4-4: Cr-depletion of as-rolled stainless rebar

	Cr-depletion depth (μm)	wt% Cr	Specified Cr – Depleted Cr (%)
V304LN AR	0.2	14.2	3.8
C2205 AR	2-3	19.2	2.8
V316LN AR	0.4	13.9	2.1

If these levels of Cr-depletion are representative of all stainless rebar of similar grades, then Cr-depletion should not be a major concern for the use of these bars in structures, as a Cr-depleted region this thin could corrode away to reveal the base steel to the corrosive environment without causing major damage to the concrete structure. With this very shallow Cr-depletion, it is also reasonable to assume that, in the time required for sufficient Cl^- to reach the steel to initiate corrosion, Cr will diffuse from bulk alloy and reduce this Cr-depletion or even restore the bulk alloy composition.

4.5.ii Optical Microscopy of Microstructure and Rebar Surfaces

Optical microscopy revealed a microstructure of grains elongated along the rebar axis, caused by the rolling process; the reduction in diameter is facilitated by an increase in the length of the bar. Figure 4-26 gives the longitudinal microstructure of 15M Carpenter 316LN pickled a) near the rebar surface, and b) in the interior of the rebar. The elongated grain structure is clear in these images; the vertical bands reveal the presence and direction of the grains. Optical micrographs are given for all steels in Appendix E.

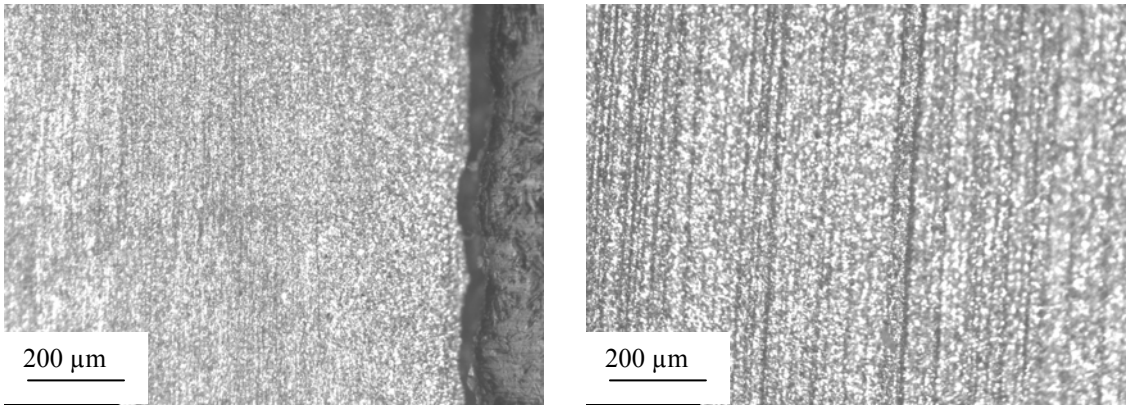

(a) (b)

Figure 4-26: Longitudinal microstructure of C316LN PIC steel (a) surface region and (b) interior

The grains of all of the steels were finer near the surface of the rebar; the grain refinement observed was believed to be an effect of faster cooling following rolling and possibly an effect of partial recrystallization near the surface caused by deformation during rolling; if rolling occurred before the steel was hot enough, early rolling may produce a finer grain structure, and subsequent rolling could then elongate these grains.

Figure 4-27 shows the cross-sectional microstructures for the C316LN PIC steel. In the transverse orientation, the grains appear equiaxed. The grains near the surface were smaller then those observed in the interior, similar to the longitudinal section.

One exception to the described microstructure was found for the 20M Valbruna 316LN steel, which did not have elongated grains near its surface. Instead, the grains in the longitudinal section were similar in structure to those shown for the cross-section in Figure 4-27. This is most likely due to some variation in the rolling process. This

suggests that this steel has recrystallized, having been rolled above the recrystallization temperature, or post-roll annealed too high or for too long. It does not seem likely that this would have any effect on the corrosion performance of the steel.

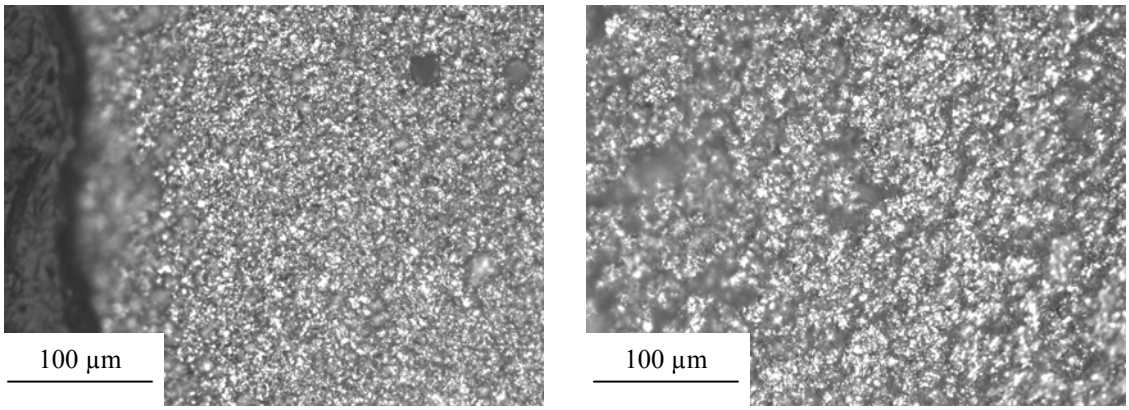

(a) (b)

Figure 4-27: Cross-sectional microstructure of C316LN PIC steel (a) surface region and (b) interior

Figure 4-28 shows the pickled surfaces of V316LN in a) 15M and b) 20M diameters. The surfaces are comparable in terms of roughness and the presence of crevices.

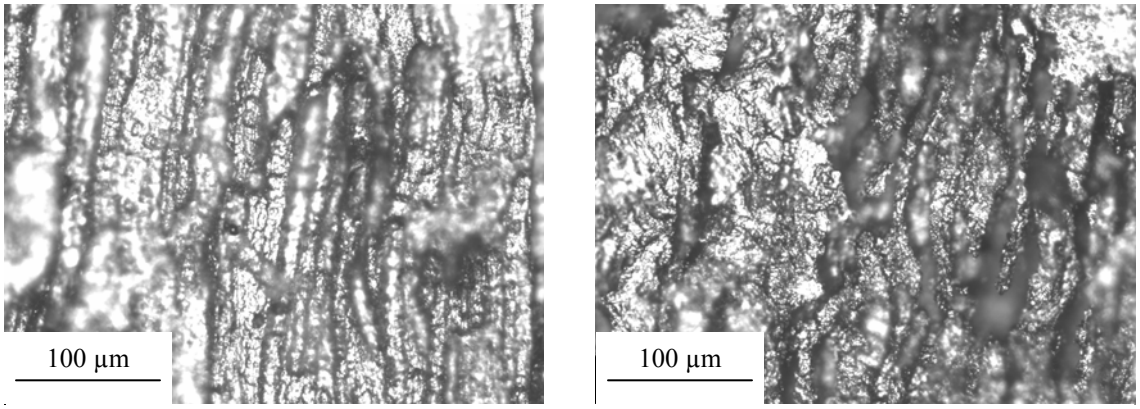

(a) (b)

Figure 4-28: Surface micrograph of V316LN PIC steel (a) 15M diameter and (b) 20M diameter

The mill scale which formed on V316LN 20M, Figure 4-29(a), was very similar in appearance to the mill scale formed on V304LN and C316LN (Appendix E). In contrast, the mill scale on C2205, Figure 4-29(b) appeared damaged, as though some abrasion process had been applied.

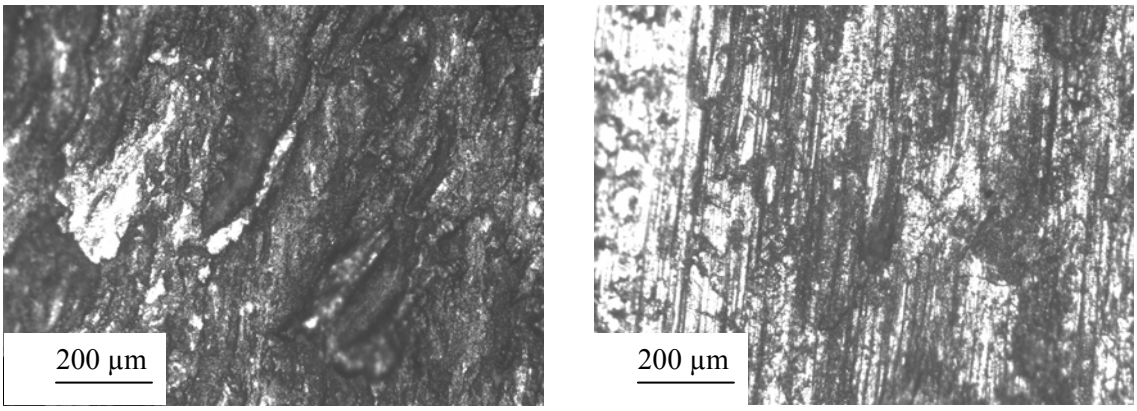

(a) (b)

Figure 4-29: (a) Sound mill scale on V316LN AR steel, compared to (b) damaged mill scale on C2205 AR

In Figure 4-29(b) many vertical bands are visible. The surface was described as damaged because the bands are all parallel, straight, and vary between what appears to be dark mill scale and bright steel, as though the mill scale had been partially removed. This surface was widespread on the C2205 AR, so it is not likely that this was damage caused by handling. These vertical bands may also be evidence of microstructural effects, such as elongated grains or the dual phase structure of the steel, but these are unlikely since the grains are not this straight on the surfaces of the other steels, nor does the dual phase structure appear in the V2205 steel.

Overall, no evidence was found of significant differences in the microstructure or surface conditions of the steels. It is not likely that differences in microstructure or surface condition between the steels (aside from the presence of mill scale) would have a pronounced affected on corrosion performance as tested here, however, the work performed during rolling introduces internal stress near the surface of the bar and may increase the likelihood of stress corrosion cracking in real structures, although external stresses on the bars are only a small fraction of those required for SCC.

4.5.iii X-Ray Diffraction of Corrosion Products

Solid corrosion products were visible on the surface of the mortar covered bars following the procedure described in section 3.4. Some of these corrosion products were collected, dried, and then ground to a fine powder for X-ray diffraction (XRD). The resultant peaks

from the XRD of the corrosion products taken from V316LN PIC are shown in Figure 4-30.

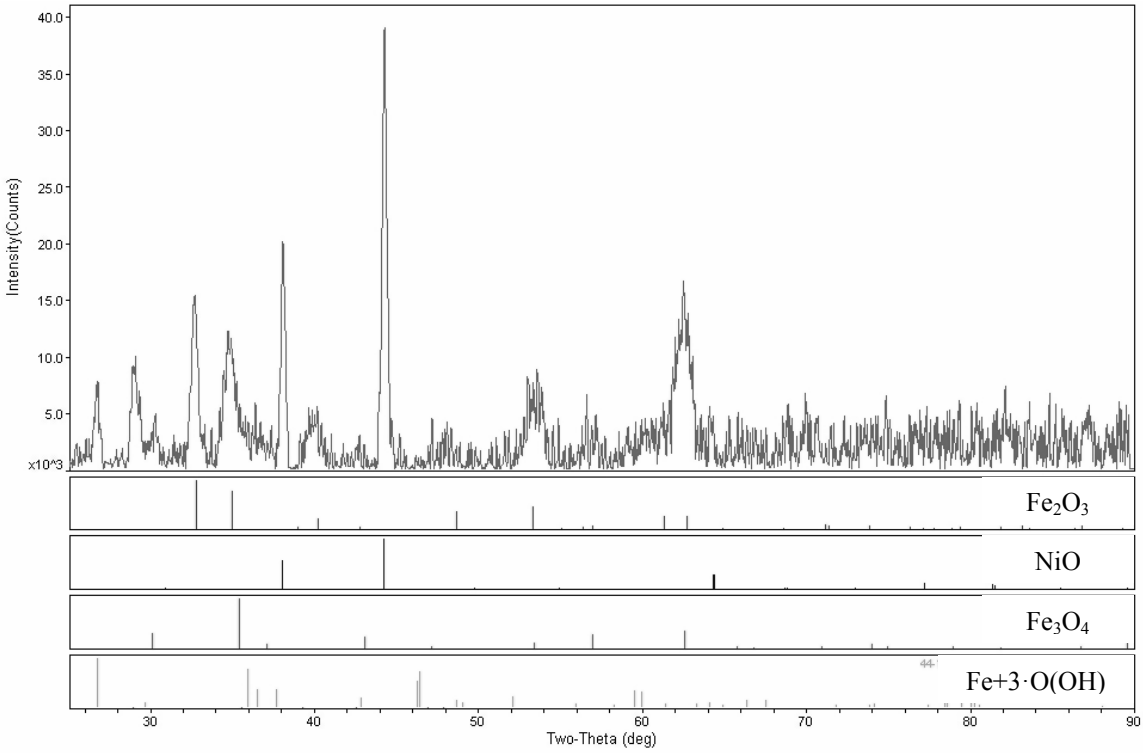

Figure 4-30: XRD scan for corrosion products developed on Valbruna 316LN pickled

The major peaks in Figure 4-30 are for Fe-oxides and what is believed to be NiO. The major peaks, identified as NiO, may also be the aluminum sample holder, although aluminum peaks were not compared at the time of testing. The only Fe-based corrosion products whose peaks roughly matched those found were Fe_2O_3, Fe_3O_4 and Fe+3·O(OH). Peaks were compared to the graph for Cr, Ni and Mo oxides, as well as spinels of Fe and the alloys, none of these peaks matched the XRD of the corrosion product analyzed.

This result agrees with the products predicted by the E/pH diagrams for Cr and Fe, which show that at the potential applied, at the pH of the mortar and test solution, solid Fe_2O_3 is stable, while Cr exists as the non-solid CrO_4^{2-} ion [4]. The instability of Cr at this potential explains the failure of the applied potential test, as Cr_2O_3 would have become unstable and dissolved from the when the potential was first applied.

It was also expected that $NiFe_2O_4$ would appear, as it is stable up to +500 mV in this environment [57], but no match could be confirmed between the recorded spectrum and standard peaks for it.

5 Summary and Conclusions

The corrosion behaviour of steels of all grades and both surface conditions was determined by LPR and CP tests in synthetic concrete pore solution with up to 16% Cl^- by weight of solution. LPR indicated similar performance between grades, with corrosion rates about an order of magnitude higher for as-rolled steels compared to pickled steels at high chloride concentrations. CP revealed inferior pitting resistance for the as-rolled steels under an applied anodic potential; however, the potentials at which pitting occurred are higher than can be expected in service. The one exception to this statement might be if they are exposed to stray currents, eg. from electrified railroad systems. Rapid chloride diffusion tests failed to yield any conclusive results.

Metallographic investigation of the bars revealed an extremely narrow Cr-depleted region, and similar surface microstructures between grades. Furthermore, the level of depletion was not such that the passive Cr_2O_3 film should become unstable.

Neither the as-rolled nor pickled stainless rebar tested were susceptible to severe pitting under the conditions normally present in a reinforced concrete structure. Furthermore, these results may not be realistic representations of the comparative pitting performance of the steels in a real structure, as scans artificially dissolve existing Cr_2O_3 on the surface.

Some active corrosion appears to have occurred on the as-rolled 316LN steels at low Cl^- contents, identified by the spikes in i_{corr} in Figure 4-3, but lower corrosion current densities were measured at higher Cl^- contents for the same steels, indicating that the surface has been repassivated. This corrosion observed may have been due to pitting, but it may have also been the corrosion of black steel contamination or oxidizable mill scale products, which were subsequently exhausted, resulting in the decreased current.

All of the pickled steels tested performed well in LPR, with corrosion rates staying constant at 1 to 2 mA/m^2, regardless of Cl^- content. The 304LN and 316LN steels showed comparable results, with pickled bars performing as well as pickled 2205 and as-rolled bars showing final corrosion rates of 1.5 to 2.5 times that of as-rolled 2205 (Table 4-1). The difference in performance between the 2205 and the austenitic grades is not

large enough to suggest that the choice of grade will have significant effects on the corrosion performance of a reinforced structure. There was no appreciable difference in the performance of steels between producers.

The corrosion rates observed for stainless steels with mill scale, combined with the time required for sufficient Cl^- ions to reach the steel, would allow for service lives significantly longer than for black steel. The poorest performing steel was the as-rolled Valbruna 304LN, exhibiting a corrosion rate of 1.3 μm/year with no Cl^- added and 5.8 μm/year with 16% Cl^-. The corrosion rates observed for all of the as-rolled steels with up to 16% Cl^- were near 3 μm/year, with spikes up to 11.6 μm/year, a level considered to be active corrosion; however, these rates are typical of black steel with less than 1% Cl^-., and may very well be the corrosion of black steel contamination, as corrosion rates of all of the as-rolled steels return to near 3 μm/year.

Cyclic polarization results suggest that 304LN would be at risk of pitting if used in the as-rolled condition; however, 316LN would be safe to use in the as-rolled condition because the likelihood of the steel being exposed to such anodic potentials is negligible. Moreover, the chloride concentration of 5% in solution is equivalent to ~2% by weight of cement, far higher than the threshold for black steel. 2205 seems to have excellent pitting resistance with its mill scale intact.

The above statements are all based on the assumption that the rebar surface will not change over the period required for Cl^- ions to diffuse to the steel; however, diffusion of Cr in the steel may restore the Cr-depleted region to the base alloy composition. Furthermore, the minor depth of the chromium depletion also means that even if sufficient Cl^- is available at the steel surface, the depleted region will be removed by corrosion in as little as a year, exposing the stainless steel beneath. It is concluded that stainless steel rebar can be safely and reliably used with the mill scale intact.

The accelerated corrosion test, as performed, was deemed inappropriate for stainless steels, as the application of anodic potential destroys any Cr_2O_3 formed prior to casting in mortar.

Microscopy of the stainless steels detected chromium depletion limited to a few micrometers, and the chromium present in the depleted regions remained above approximately 14 wt%. These results suggest that the hot rolling process does not allow sufficient time and heat for chromium depletion to fully develop; the depleted regions all the surfaces retained enough of their chromium to be able to form Cr_2O_3.

No difference was observed between the surface conditions or surface microstructures of the pickled Valbruna 316LN in 15M or 20M diameter. Although grain elongation was observed near the surface of the 15M bars, but not the 20M bars, the size of the grains and the appearance of the surfaces were similar to each other and the other pickled steels. No comparison could be made of mill scales for different diameters of any grade; however, mill scales were all similar in thickness, varying from 3 to 10 μm on any particular surface, and morphology, regardless of grade and diameter. It is concluded that there is no appreciable difference in the corrosion performance of different bar diameters.

6 Recommendations

It is recommended that LPR testing be continued on these steels for up to several months in order to observe the longer term performance of the steel under concentrated Cl^- conditions, as it is speculated that the steels may be repassivated by the formation of Cr_2O_3. The increase in corrosion current in Carpenter 316LN at 16% suggests active corrosion, but there may be Cr_2O_3 forming.

It would also be helpful to repeat the pore solution tests, removing bars from the pore solution at increasing Cl^- contents, and following electrochemical tests, in order to visually observe the effects on the steel surface. The use of a glove box with Ar would allow for the removal of the bars from pore solution without unwanted atmospheric oxidation of the surface.

Crevice corrosion is known to affect stainless steels, and rebar in bridge decks are typically in contact with other bars at certain points within the reinforcement mat. Pore solution tests featuring bars in contact, in order to create a crevice representative of the real world situation, would allow for crevice corrosion effects to be observed.

The accelerated chloride diffusion test was not successful in determining critical chloride levels for corrosion initiation of the steels. The application of an anodic potential is expected to have destroyed any existing Cr_2O_3. It is recommended that this test be repeated with a modified design, in which the rebar being tested is not the anode driving chloride diffusion, but rather, employing a separate anode. This modification will allow chlorides to reach the steel quickly without destroying or altering the surface of the rebar.

It is also recommended that these steels be retested following electrolytic pickling instead of acid pickling. Full pickling of the steel is not necessary since the surface appearance is not important, and electrolytic pickling could be used to attack and remove only vulnerable regions on the surface.

References

1. C.M. Hansson, B. Sørensen, *The Threshold Concentration of Chloride in Concrete for the Initiation of Reinforcement Corrosion.* Corrosion Rates of Steel in Concrete, 1990, ASTM, Philadelphia, PA: p. 3-16.

2. C.M. Hansson, *Comments on Electrochemical Measurements of the Rate of Corrosion of Steel in Concrete.* Cement and Concrete Research, 1984, 14(4): p. 574-584.

3. T.P. Hoar, *The Production and Breakdown of the Passivity of Metals.* Corrosion Science, 1967, 7: p. 341-355.

4. M. Pourbaix, *Atlas of Electrochemical Equilibria in Aqueous Solutions.* NACE: Houston, TX, 1984.

5. T.D. Marcotte, *Characterization of Chloride-Induced Corrosion Products that Form in Steel-Reinforced Cementitious Materials.* PhD Thesis in Dept. of Mechanical Engineering, 2001, University of Waterloo: Waterloo, ON, Canada: p. 330.

6. S.R. Yoemans, *Performance of Black, Galvanized, and Epoxy-Coated Reinforcing Steels in Chloride-Contaminated Concrete.* Corrosion, 1994, 50(1): p. 72-81.

7. W.A. Pyc, R.E. Weyers, M.M. Sprinkel, R.M. Weyers, D.W. Mokarem, J.G. Dillard, *Performance of Epoxy-Coated Reinforcing Steel.* Concrete International, 2000. 22(2): p. 57-62.

8. G. Hultquist, C. Leygraf, *Highly Protective Films on Stainless Steels.* Materials Science and Engineering, 1980, 42: p. 199-206.

9. T.P. Teng, *Critical Literature Review of High-Performance Corrosion Reinforcements in Concrete Bridge Applications.* FHWA Report FWHA-RD-04-093, National Technical Information Service, Springfield, Virginia. 2004.

10. *Pier in Progreso, Mexico: Inspection Report, Evaluation of the Stainless Steel Reinforcement.* RAMBØLL Consulting Engineers and Planners, Copenhagen, Denmark, 1999.

11. D.B. McDonald, M.R. Sherman, D.W. Pfeifer, Y.P. Virmani, *Stainless Steel Reinforcing as Corrosion Protection.* Concrete International, May 1995: p. 65-70.

12. *Willing to Bend.* Roads and Bridges, 2002, 40(5): p. 34-37.

13. *New Bridge in Brooklyn Features 100-year Life, Stainless Rebar, Precast Construction, Fast Build, No Traffic Disruption.* Carpenter Technology, 12 August 2004.

14. D. Trejo, R.G. Pillai, *Accelerated Chloride Threshold Testing – Part I: ASTM A 615 and A 706 Reinforcement.* ACI Materials Journal, 2003, 100(6): p. 519-527.

15. D. Trejo, R.G. Pillai, *Accelerated Chloride Threshold Testing – Part II: Corrosion-Resistant Reinforcement.* ACI Materials Journal, 2004, 101(1): p. 57-64.

16. M.F. Hurley, J.R. Scully, *Threshold Chloride Concentrations of Selected Corrosion-Resistant Rebar Materials Compared to Carbon Steel.* Corrosion, 2006. 62(10): p. 892-904.

17. G. Clemeña, Y.P. Virmani, *Comparing the Chloride Resistances of Reinforcing Bars.* Concrete International, 2004. 26(11): p. 39-49.

18. S. Goni, C. Andrade, *Synthetic Concrete Pore Solution Chemistry and Rebar Corrosion Rate in the Presence of Chlorides.* Cement and Concrete Research, 1990. 20: p. 525-539.

19. Rasheeduzzafar, F.H. Dakhil, M.A. Bader, M.M. Khan, *Performance of Corrosion Resisting Steels in Chloride-Bearing Concrete.* ACI Materials Journal, 1992, 89(5): p. 439-448.

20. L. Mammoliti, C.M. Hansson, *The Influence of Surface Treatment on Corrosion Behaviour of Stainless Steel Reinforcement Part 1: Tests in Synthetic Pore Solution.* Submitted for publication.

21. H.H. Uhlig, *Structure and Growth of Thin Films on Metals Exposed to Oxygen.* Corrosion Science, 1967, 7: p. 325-339.

22. P.A. Tempest, R.K. Wild, *Thickness Measurements of Spinel and Chromia Layers in Stainless Steel Oxide Scales by X-Ray Diffractometry.* Oxidation of Metals, 1982, 17(5/6): p. 345-357.

23. B. Johnson, F. Nelson, *Management of Coastal Bridges Using Cathodic Protection and Stainless Steel Reinforcing Bars.* Technical Memorandum of Public Works Research Institute, 2006. http://www.pwri.go.jp/eng/ujnr/tc/g/pdf/21/21-8-2johnson.pdf, accessed 01-02-2008.

24. W.F. Smith, *Structure and Properties of Engineering Alloys, 2nd ed.* Materials Science and Engineering Series, McGraw-Hill, New York, NY, 1993.

25. N. Boucherit, A. Hugot-Le Goff, S. Joiret, *Influence of Ni, Mo and Cr on Pitting Corrosion of Steels Studied by Raman Spectroscopy.* Corrosion, 1992. 48(7): p. 569-579.

26. B.H. Neuhart, *Use of Stainless Steels in Reinforced Concrete Structures-Status 1998.* State-of-the-Art Report, Specialty Steel Industry of North America, 1998.

27. H. Castro, C. Rodriguez, F.J. Belzunce, A.F. A.F. Canteli, *Mechanical Properties and Corrosion Behaviour of Stainless Steel Reinforcing Bars.* Journal of Materials Processing Technology, 2003. 143/144: p. 134-137.

28. InfoMine, *Metal Commodities Price Chart: Steel 3-month.* http://www.infomine.com/investment, accessed 02-09-2008.

29. MetalPrices.com, *Primary Metals List: Chrome Price Charts.* http://www.metalprices.com, accessed 02-09-2008..

30. InfoMine, *Metal Commodities Price Chart: Nickel 10-year.* http://www.infomine.com/investment, accessed 02-09-2008.

31. InfoMine, *Metal Commodities Price Chart: Molybdenum 10-year.* http://www.infomine.com/investment, accessed 02-09-2008.

32. B.S. Covino Jr., J.V. Scalera, P.M. Fabis, *Pickling of Stainless Steels – A Review.* Information Circular, US Department of the Interior, Bureau of Mines, 1984.

33. F. Pianca, *Reinforcement Installed Cost Comparison for 2007.* Personal communication, 17-10-2008.

34. J.F. McGurn, *Stainless Steel Reinforcing Bars in Concrete.* State-of-the-Art Report, Nickel Development Institute.

35. H. Shibata, S. Itoyama, K. Sorimachi, *US Patent 6261639: Process for Hot-Rolling Stainless Steel.* United States Patent, 17-07-2001.

36. G. Bombara, A. Tamba, N. Azzerri, *Potentiostatic Anodic Pickling of Stainless Steels.* Journal of the Electrochemical Society: Electrochemical Technology, 1971. 118(4): p. 676-681.

37. L.-F. Li, J.-P. Celis, *Pickling of Austenitic Stainless Steels (A Review).* Canadian Metallurgical Quarterly, 2003. 42(3): p. 365-376.

38. *ASSDA - Pickling and Passivation.* Australian Stainless Steel Development Association, 2006. http://www.assda.asn.au/index.php?option=com_content&task=view&id=78&Itemid=103, accessed 01-02-2008.

39. H.E. Evans, D.A. Hilton, R.A. Holm, *Chromium-Depleted Zones and the Oxidation Process in Stainless Steels.* Oxidation of Metals, 1976. 10(3): p. 149-161.

40. G.C. Wood, D.P. Whittle, *The Mechanism of Breakthrough of Protective Chromium Oxide Scales on Fe-Cr Alloys.* Corrosion Science, 1967. 7: p. 763-782.

41. G.C. Wood, D.P. Whittle, *On the Mechanism of Oxidation of Iron-16.4% Chromium at High Temperature.* Corrosion Science, 1964. 4: p. 263-292.

42. G.C. Wood, D.P. Whittle, *The Unusual Scaling Behaviour of Iron-22.9% Chromium at High Temperature.* Corrosion Science, 1964. 4: p. 293-313.

43. S.H.C. Park, Y.S. Sato, H. Kokawa, K. Okamoto, S. Hirano, M. Inagaki, *Corrosion Properties in Friction Stir Welded 304 Austenitic Stainless Steel.* Welding in the World, 2005. 49(3/4): p. 63-68.

44. G. Blanco, A. Bautista, H. Takenouti, *EIS Study of Passivation of Austenitic and Duplex Stainless Steel Reinforcements in Simulated Pore Solutions.* Cement & Concrete Composites, 2006. 28: p. 212-219.

45. *Basics of Electrochemical Impedance Spectroscopy.* Princeton Applied Research, Application Note AC-1, http://www.princetonappliedresearch.com/products/appnotes.cfm, accessed 26-06-2006.

46. C.M. Abreu, M.J. Cristóbal, R. Losada, X.R. Nóvoa, G. Pena, M.C. Pérez, *High Frequency Impedance Spectroscopy Study of Passive Films Formed on AISI 316 Stainless Steel in Alkaline Medium.* Journal of Electroanalytical Chemistry, 2004. 572: p. 335-345.

47. P. Schmuki, H. Hildebrand, A. Friedrich, S. Virtanen, *The Composition of the Boundary Region of MnS inclusions in Stainless Steel and Its Relevance in Triggering Pitting Corrosion.* Corrosion Science, 2005. 47: p. 1239-1250.

48. P. Gu, S. Elliott, J.J. Beaudoin, B. Arsenault, *Corrosion Resistance of Stainless Steel in Chloride Contaminated Concrete.* Cement and Concrete Research, 1996. 26(8): p. 1151-1156.

49. L. Veleva, M.A. Alpuche-Aviles, M.K. Graves-Brook, D.O. Wipf, *Comparative Cyclic Voltammetry and Surface Analysis of Passive Films Grown on Stainless Steel 316 in Concrete Pore Model Solutions.* Journal of Electroanalytical Chemistry, 2002. 537: p. 85-93.

50. C.M. Hansson, Th. Frølund, J.B. Markussen, *The Effect of Chloride Cation Type on the Corrosion of Steel in Concrete by Chloride Salts.* Cement and Concrete Research, 1985. 15: p. 65-73.

51. R.G. Pillai, D. Trejo, *Surface Condition Effects on Critical Chloride Threshold of Steel Reinforcement.* ACI Materials Journal, 2005, 102(2): p. 103-109.

52. G.G. Miller, D. Darwin, *Performance and Constructibility of Silica Fume Bridge Deck Overlays.* SM Report No. 57, University of Kansas Center for Research, 2002.

53. M.C. Garcia-Alonso, M.L. Escudero, J.M. Miranda, M.I. Vega, F. Capilla, M.J. Correia, M. Salta, A. Bennani, J.A. González, *Comments on Electrochemical Measurements of the Rate of Corrosion of Steel in Concrete.* Cement and Concrete Research, 2007. 37: p. 1463-1471.

54. L.T. Mammoliti, L.C. Brown, C.M. Hansson, B.B. Hope, *The Influence of Surface Finish of Reinforcing Steel and pH of the Test Solution on the Chloride Threshold Concentration for Corrosion Initiation in Synthetic Pore Solutions.* Cement and Concrete Research, 1996. 26(4): p. 545-550.

55. C. Alonso, C. Andrade, M. Izquierdo, X.R. Nóvoa, M.C. Pérez, *Effect of Protective Oxide Scales in the Macrogalvanic Behaviour of Concrete Reinforcements.* Corrosion Science, 1998. 40(8): p. 1379-1389.

56. R.S. Barneyback, Jr., S. Diamond, *Expression and Analysis of Pore Fluids from Hardened Cement Pastes and Mortars.* Cement and Concrete Research, 1981. 11: p. 279-285.

57. B. Beverskog, I. Puigdomenech, *Pourbaix Diagrams for the Ternary System of Iron-Chromium-Nickel.* Corrosion, 1999. 55(11): p. 1077-1087.

58. D.A. Jones, *Principles and Prevention of Corrosion, 2nd ed.* Prentice Hall, Upper Saddle River, NJ, 1996.

59. M. Stern, A.L. Geary, *Electrochemical Polarization I: A Theoretical Analysis of the Shape of Polarization Curves.* Journal of the Electrochemical Society, 1957. 104(1): p. 56-63.

60. J.T. Kahrs, D. Darwin, C.E. Locke Jr., *Evaluation of Corrosion Resistance of Type 304 Stainless Steel Clad Reinforcing Bars*. Structural Engineering and Engineering Materials SM Report No. 65, University of Kansas Center for Research Inc., Kansas, 2001.

61. R.E. Reed-Hill, R. Abbaschian, *Physical Metallurgy Principles, 3rd ed.* The PWS Series in Engineering, PWS Publishing Company, Boston, MA, 1994.

62. ASTM C876-91 (1999), *Standard Test Method for Half-Cell Potentials of Uncoated Reinforcing Steel in Concrete*.

63. D.W. Pfeiffer, *High Performance Concrete and Reinforcing Steel with a 100-Year Service Life.* PCI Journal, 2000. 45(3): p. 46-54.

64. C. Alonso, C. Andrade, M. Castellote, P. Castro, *Chloride Threshold Values to Depassivate Reinforcing Bars Embedded in a Standardized OPC Mortar.* Cement and Concrete Research, 2000. 30: p. 1047-1055.

65. R.F.A. JargeIius-Pettersson, B.G. Pound, *Examination of the Role of Molybdenum in Passivation of Stainless Steels Using AC Impedance Spectroscopy.* Journal of the Electrochemical Society, 1998. 145(5): p. 1462-1469.

66. V. Vignal, J.M. Olive, D. Desjardins, *Effect of Molybdenum on Passivity of Stainless Steels in Chloride Media using Ex Situ Near Field Microscopy Observations.* Corrosion Science, 1999. 41: p. 869-884.

67. C.M. Abreu, M.J. Cristóbal, R. Losada, X.R. Nóvoa, G. Pena, M.C. Pérez, *Comparative Study of Passive Films of Different Stainless Steels Developed in Alkaline Medium.* Electrochemica Acta, 2004. 49: p. 3049-3056.

Appendix A - Chloride Additions for Pore Solution Cells

	Carpenter				Valbruna				
	2205 AR	2205 PIC	316LN AR	316LN PIC	2205 PIC	304LN AR	304LN PIC	316LN AR	316LN PIC
Solution Mass (g)	**2492.50**	**2470.59**	**2488.26**	**2462.04**	**2499.93**	**2506.92**	**2499.95**	**2499.63**	**2500.08**
Calc 2.5%	**107.14**	**106.20**	**106.96**	**105.83**	**107.46**	**107.76**	**107.46**	**107.44**	**107.46**
Added for 2.5%	**107.14**	**106.20**	**107.31**	**105.76**	**107.43**	**107.79**	**107.46**	**107.40**	**107.45**
Calc 5.0%	223.90	221.93	223.52	221.16	224.57	225.19	224.57	224.54	224.58
- Added for 2.5%	**116.76**	**115.73**	**116.21**	**115.40**	**117.14**	**117.40**	**117.11**	**117.14**	**117.13**
Added for 5.0%	**116.73**	**115.73**	**116.36**	**115.20**	**117.13**	**117.40**	**117.12**	**117.10**	**117.10**
Total Added 5.0%	223.87	221.93	223.67	220.96	224.56	225.19	224.58	224.50	224.55
Calc 7.5%	351.64	348.55	351.05	347.35	352.69	353.68	352.70	352.65	352.71
- Added for 5.0%	**127.77**	**126.62**	**127.38**	**126.39**	**128.13**	**128.49**	**128.12**	**128.15**	**128.16**
Added for 7.5%	**127.84**	**126.62**	**127.57**	**126.03**	**128.13**	**128.49**	**128.12**	**128.15**	**128.18**
Total Added 7.5%	351.71	348.55	351.24	346.99	352.69	353.68	352.70	352.65	352.73
Calc 10.0%	492.00	487.67	491.16	485.98	493.46	494.84	493.47	493.40	493.49
- Added for 7.5%	**140.29**	**139.12**	**139.92**	**138.99**	**140.77**	**141.16**	**140.77**	**140.75**	**140.76**
Added for 10.0%	**140.27**	**139.25**	**139.91**	**138.98**	**140.81**	**141.28**	**140.81**	**140.78**	**140.78**
Total Added 10.0%	491.98	487.80	491.15	485.97	493.50	494.96	493.51	493.43	493.51
Solutions Replaced									
Solution Mass (g)	**2211.82**	**2211.82**	**2215.84**	**2216.96**	**2211.82**	**2210.83**	**2210.83**	**2210.84**	**2211.83**
Calc 10.0%	436.59	436.59	437.39	437.61	436.59	436.40	436.40	436.40	436.59
Added for 10.0%	**436.60**	**436.60**	**437.75**	**437.60**	**436.60**	**436.40**	**436.40**	**436.40**	**436.60**
Calc 12.0%	545.44	545.44	546.44	546.71	545.44	545.20	545.20	545.20	545.45
- Added for 10.0%	**108.84**	**108.84**	**108.69**	**109.11**	**108.84**	**108.80**	**108.80**	**108.80**	**108.85**
Added for 12.0%	**108.84**	**108.84**	**108.65**	**109.11**	**108.84**	**108.81**	**108.82**	**108.80**	**108.85**
Total Added 12.0%	545.44	545.44	546.40	546.71	545.44	545.21	545.22	545.20	545.45
Calc 14.0%	663.63	663.63	664.83	665.17	663.63	663.33	663.33	663.33	663.63
- Added for 13.0%	**118.19**	**118.19**	**118.43**	**118.46**	**118.19**	**118.12**	**118.11**	**118.13**	**118.18**
Added for 14.0%	**118.19**	**118.19**	**118.43**	**118.45**	**118.19**	**118.12**	**118.11**	**118.13**	**118.18**
Total Added 14.0%	663.63	663.63	664.83	665.16	663.63	663.33	663.33	663.33	663.63
Calc 15.0%	726.60	726.60	727.92	728.29	726.60	726.28	726.28	726.28	726.60
- Added for 14.0%	**62.97**	**62.97**	**63.09**	**63.13**	**62.97**	**62.95**	**62.95**	**62.95**	**62.97**
Added for 15.0%								**62.95**	**62.97**
Total Added 15.0%	663.63	663.63	664.83	665.16	663.63	663.33	663.33	726.28	726.60
Calc 16.0%	792.39	792.39	793.83	794.24	792.39	792.04	792.04	792.04	792.40
- Added for 10.0%	**128.76**	**128.76**	**129.00**	**129.08**	**128.76**	**128.71**	**128.71**	**65.76**	**65.80**
Added for 16.0%	**128.76**	**128.76**	**129.00**	**129.08**	**128.76**	**128.71**	**128.71**	**65.76**	**65.80**
Total Added 16.0%	792.39	792.39	793.83	794.24	792.39	792.04	792.04	792.04	792.40

Appendix B – Corrosion Rate Conversion

The rate of material loss at a uniformly corroding surface can be determined using Faraday's Law:

$$r\left[m/s\right] = \frac{i_{corr}\left[C/s*m^2\right]*M\left[g/mol\right]}{\rho\left[g/m^3\right]*n*F\left[C/mol\right]}, \tag{B1}$$

where i_{corr} is corrosion current density, M is molar mass, ρ is density, n is valence electrons released for the particular species, and F is Faraday's constant, 96 500 coulomb's required to oxidize 1 equivalent of material.

Continuity exists in the units, as demonstrated:

$$r = \frac{C}{s*m^2}\frac{g}{mol}\frac{m^3}{g}\frac{mol}{C} = \frac{m}{s}; \tag{B2}$$

however, measuring corrosion of reinforcement in m/s does not provide a realistic idea of the damage occurring. The rate can be converted to μm/year by the following modification:

$$r\left[\mu m/year\right] = r\left[m/s\right]\frac{10^6\,\mu m}{m}\frac{3.1536\times10^7\,s}{year} = 3.1536\times10^{13}*r\left[m/s\right] \tag{B3}$$

Substituting (B1) into (B3) gives:

$$r\left[\mu m/year\right] = 3.1536\times10^{13}*\frac{i_{corr}*M}{\rho*n*F} \tag{B4}$$

Applying molar mass and density for Fe:

$$r\left[\mu m/year\right] = 772.66*i_{corr}\left[A/m^2\right] \tag{B5}$$

Appendix C – Microcell Corrosion of Steels in Pore Solution

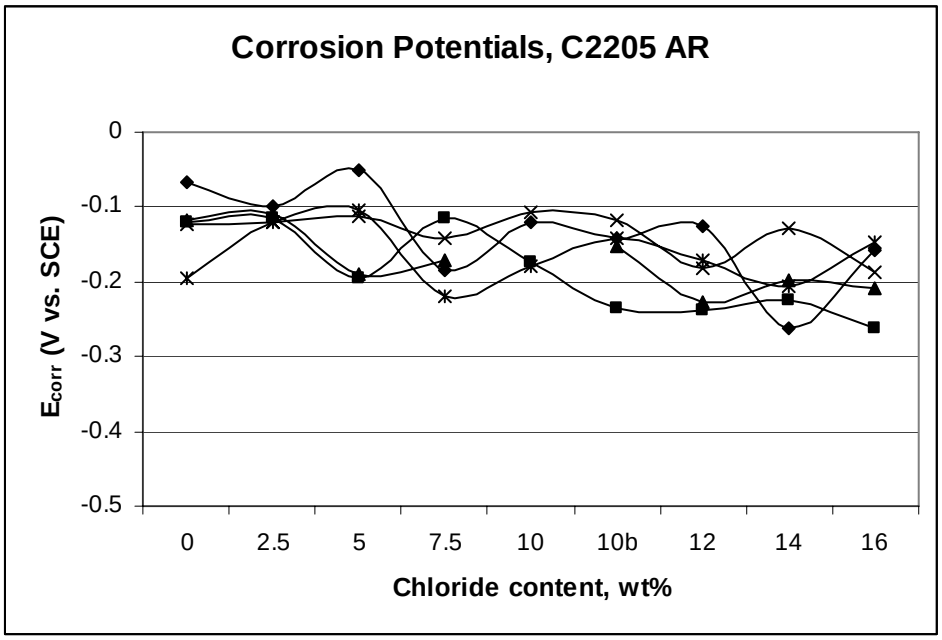
Corrosion Potentials, C2205 AR
0
-0.1
-0.2
-0.3
-0.4
-0.5
Ecorr (V vs. SCE)
0
2.5
5
7.5
10
10b
12
14
16
Chloride content, wt%

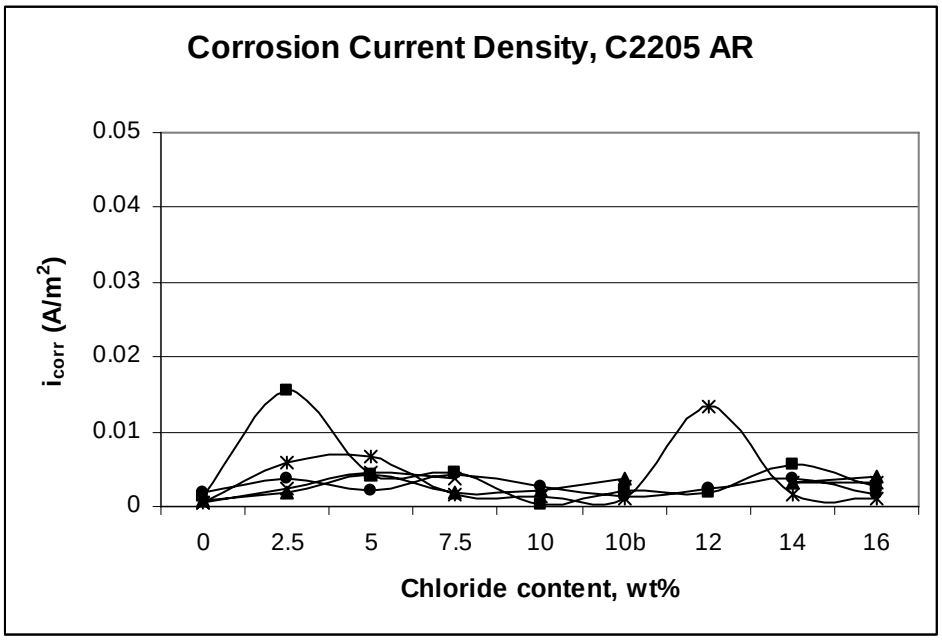
Corrosion Current Density, C2205 AR
0.05
0.04
0.03
0.02
0.01
0
icorr (A/m2)
0
2.5
5
7.5
10
10b
12
14
16
Chloride content, wt%

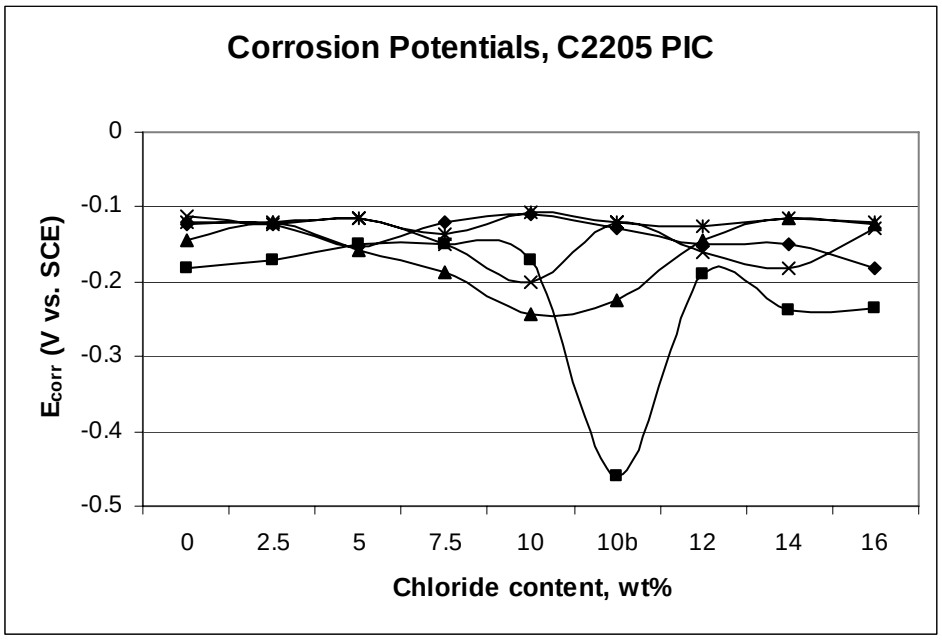
Corrosion Potentials, C2205 PIC
0
-0.1
-0.2
-0.3
-0.4
-0.5
Ecorr (V vs. SCE)
0
2.5
5
7.5
10
10b
12
14
16
Chloride content, wt%

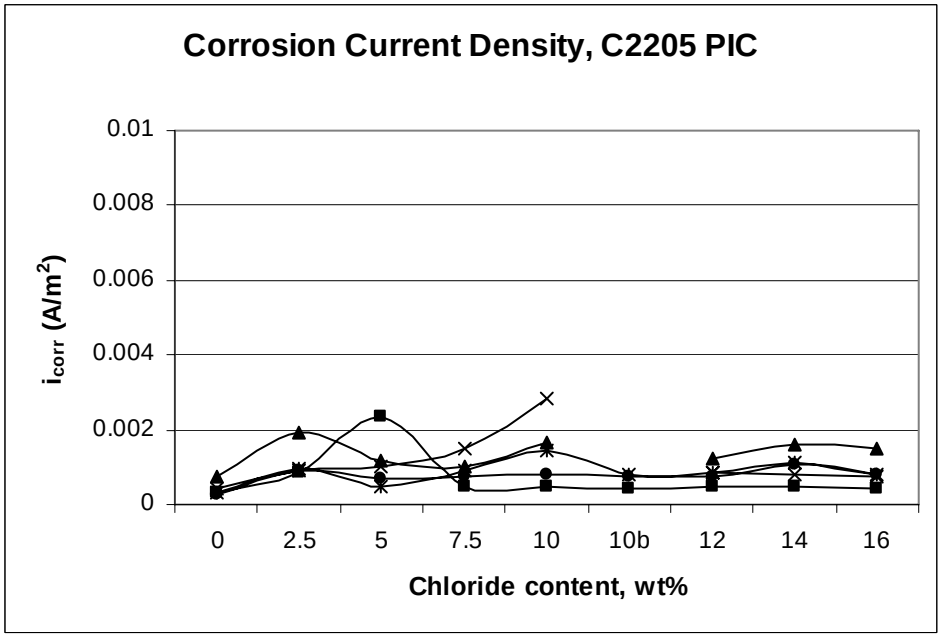
Corrosion Current Density, C2205 PIC
0.01
0.008
0.006
0.004
0.002
0
icorr (A/m2)
0
2.5
5
7.5
10
10b
12
14
16
Chloride content, wt%

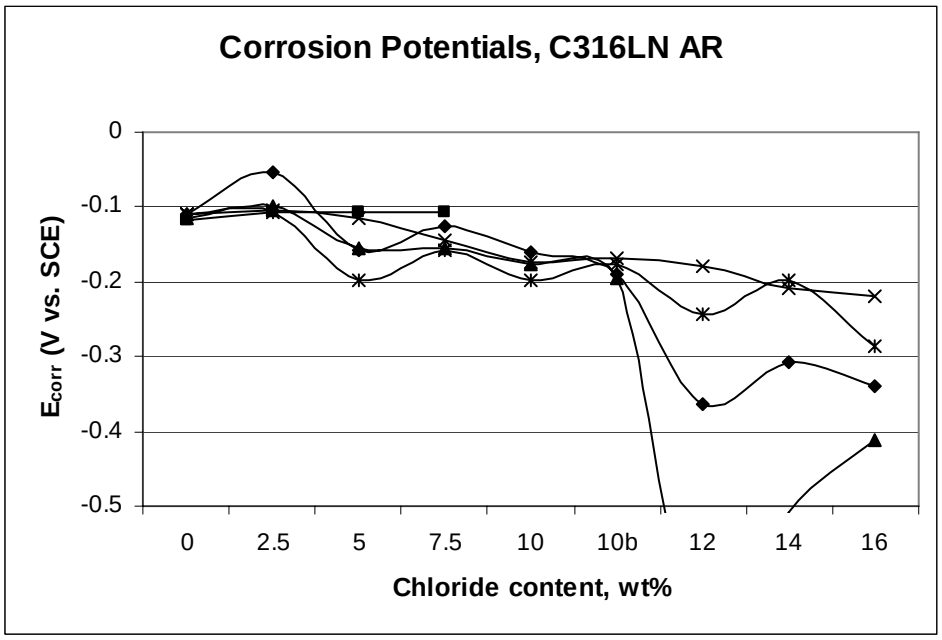
Corrosion Potentials, C316LN AR
0
-0.1
-0.2
-0.3
-0.4
-0.5
Ecorr (V vs. SCE)
0
2.5
5
7.5
10
10b
12
14
16
Chloride content, wt%

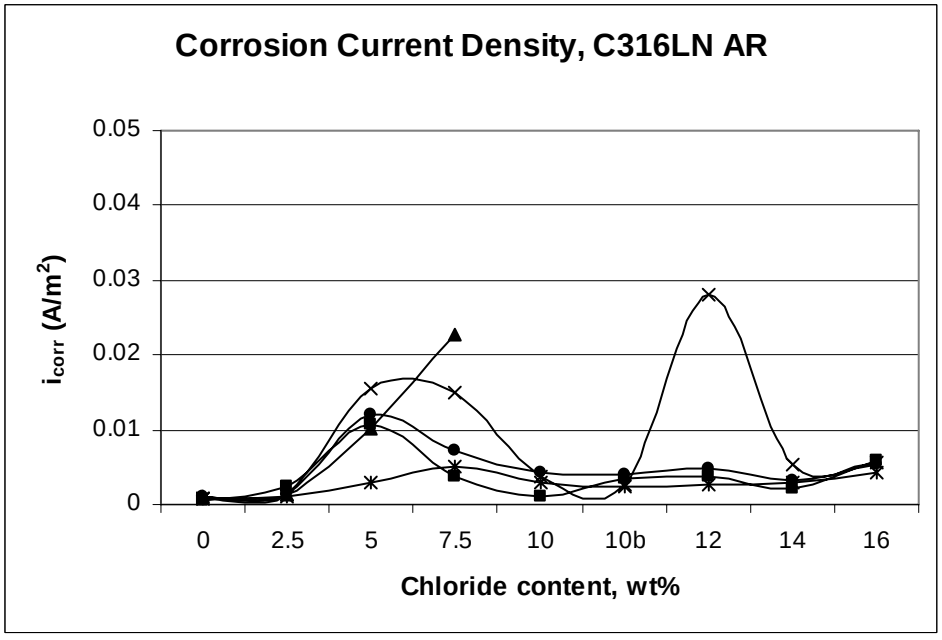
Corrosion Current Density, C316LN AR
0.05
0.04
0.03
0.02
0.01
0
icorr (A/m2)
0
2.5
5
7.5
10
10b
12
14
16
Chloride content, wt%

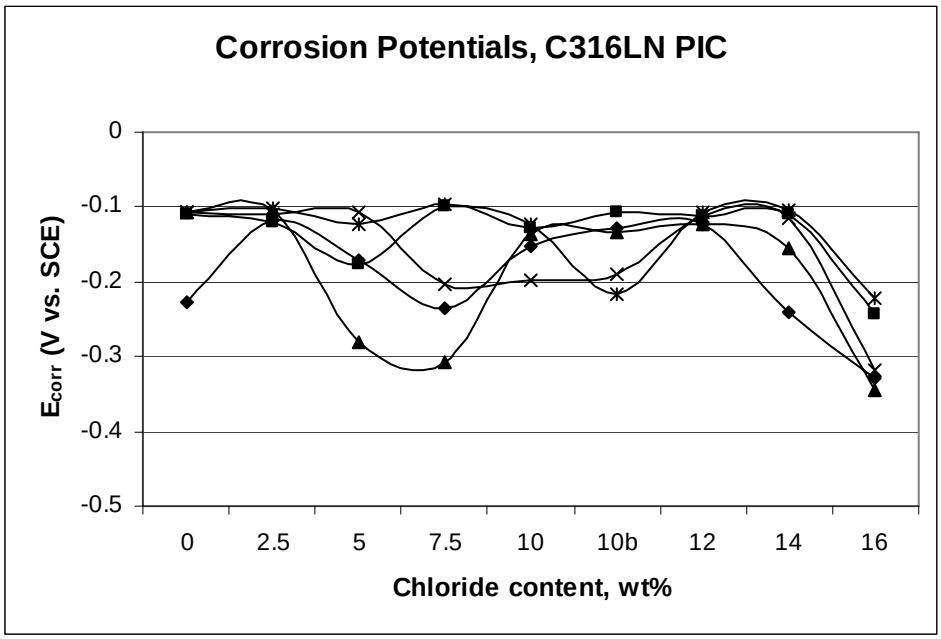
Corrosion Potentials, C316LN PIC
0
-0.1
-0.2
-0.3
-0.4
-0.5
Ecorr (V vs. SCE)
0
2.5
5
7.5
10
10b
12
14
16
Chloride content, wt%

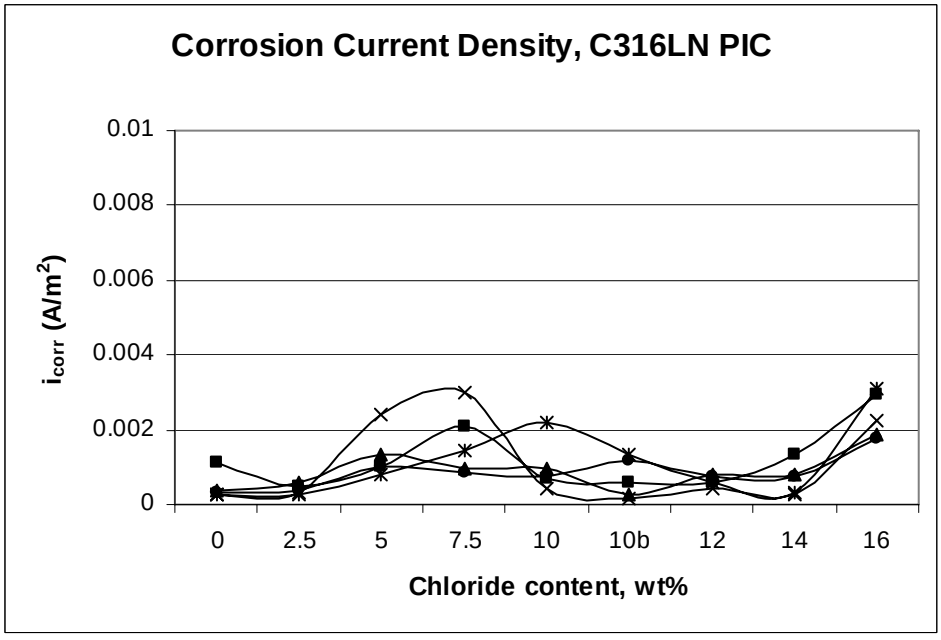
Corrosion Current Density, C316LN PIC
0.01
0.008
0.006
0.004
0.002
0
icorr (A/m2)
0
2.5
5
7.5
10
10b
12
14
16
Chloride content, wt%

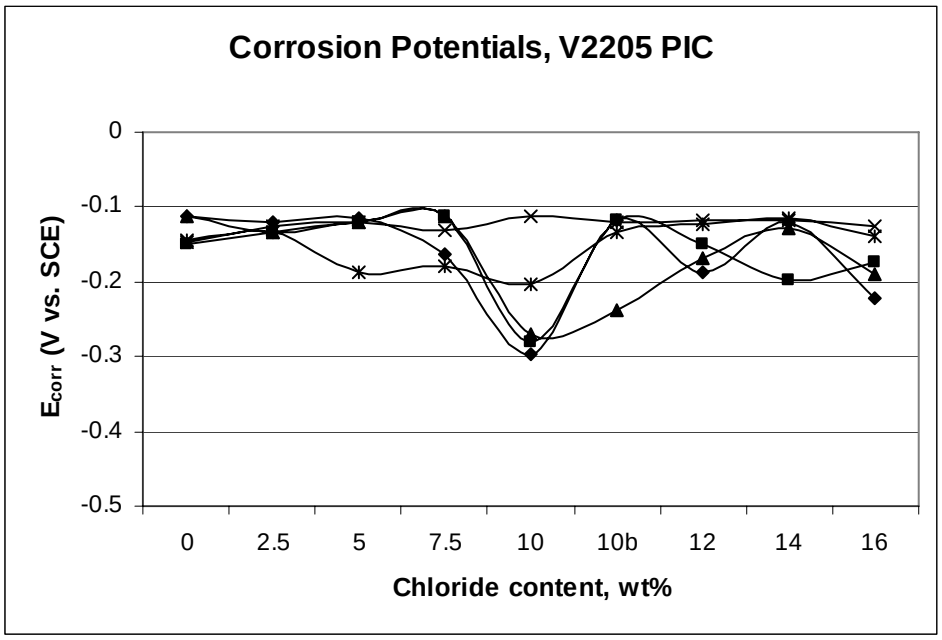
Corrosion Potentials, V2205 PIC
0
-0.1
-0.2
-0.3
-0.4
-0.5
Ecorr (V vs. SCE)
0
2.5
5
7.5
10
10b
12
14
16
Chloride content, wt%

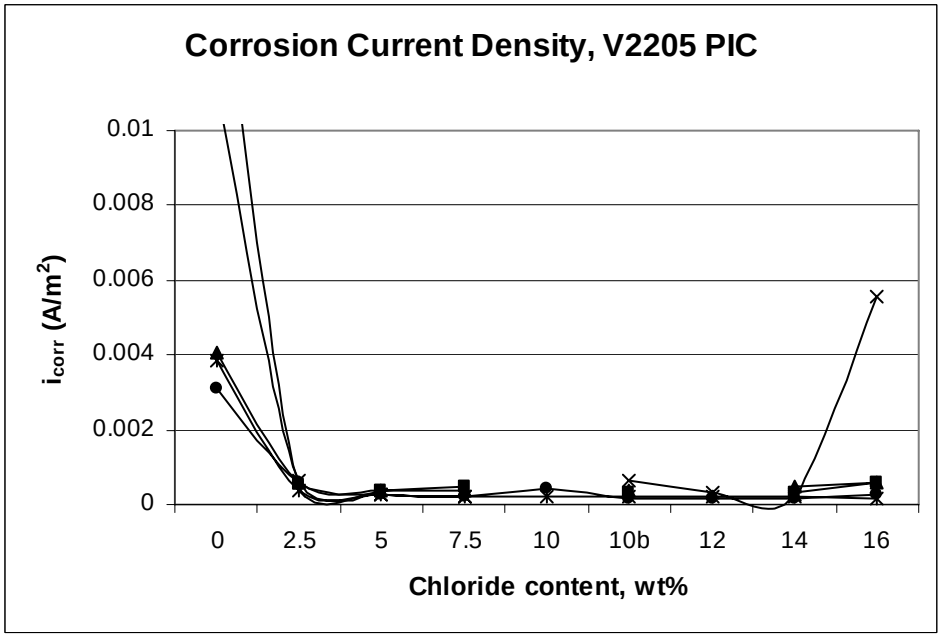
Corrosion Current Density, V2205 PIC
0.01
0.008
0.006
0.004
0.002
0
icorr (A/m2)
0
2.5
5
7.5
10
10b
12
14
16
Chloride content, wt%

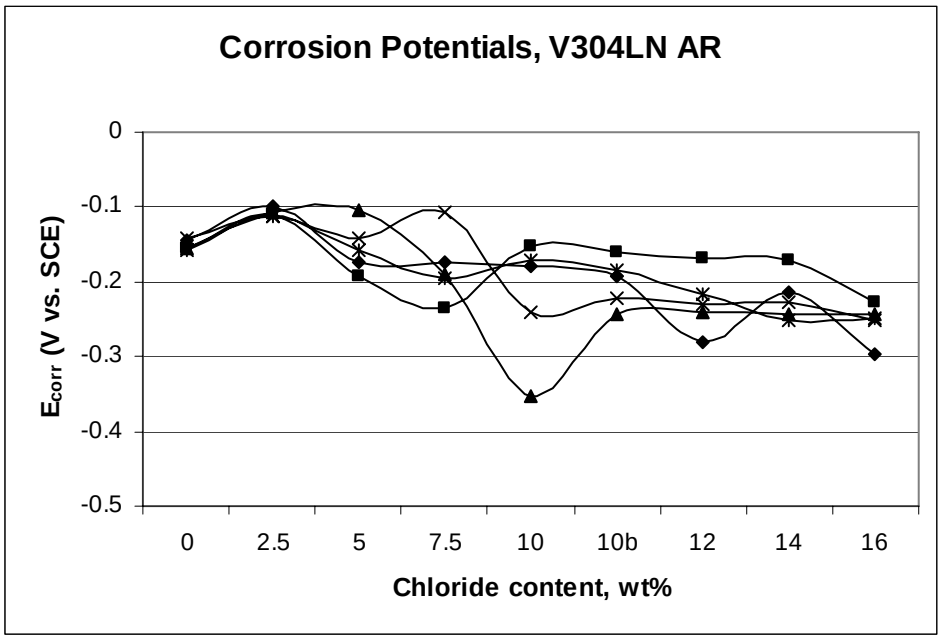
Corrosion Potentials, V304LN AR
0
-0.1
-0.2
-0.3
-0.4
-0.5
Ecorr (V vs. SCE)
0
2.5
5
7.5
10
10b
12
14
16
Chloride content, wt%

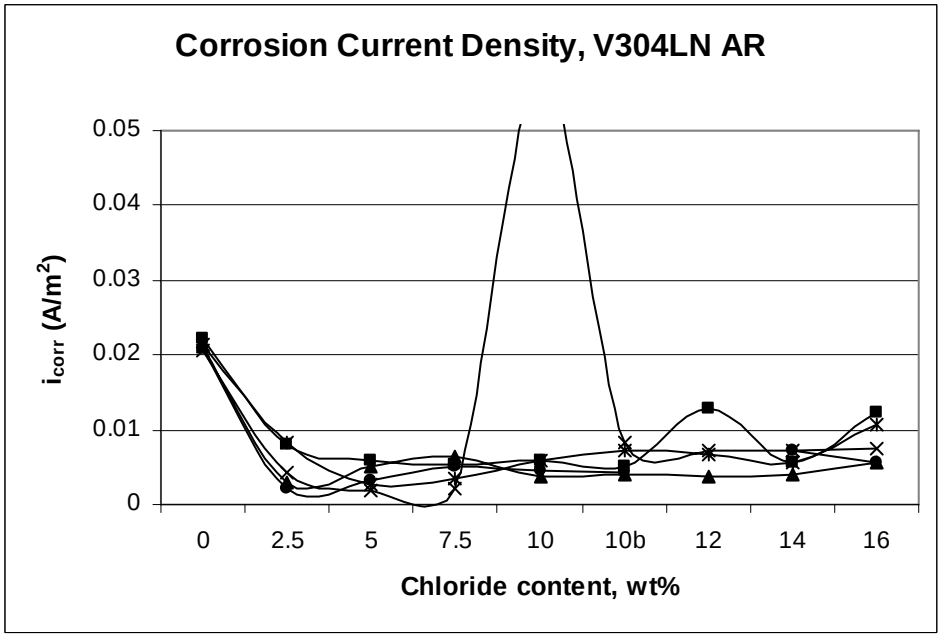
Corrosion Current Density, V304LN AR
0.05
0.04
0.03
0.02
0.01
0
icorr (A/m2)
0
2.5
5
7.5
10
10b
12
14
16
Chloride content, wt%

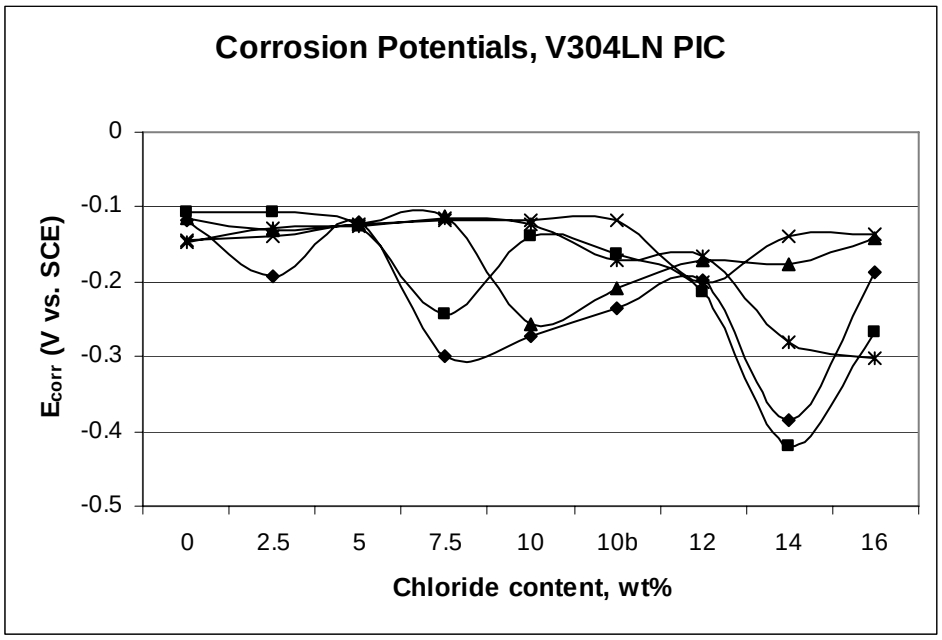
Corrosion Potentials, V304LN PIC
0
-0.1
-0.2
-0.3
-0.4
-0.5
Ecorr (V vs. SCE)
0
2.5
5
7.5
10
10b
12
14
16
Chloride content, wt%

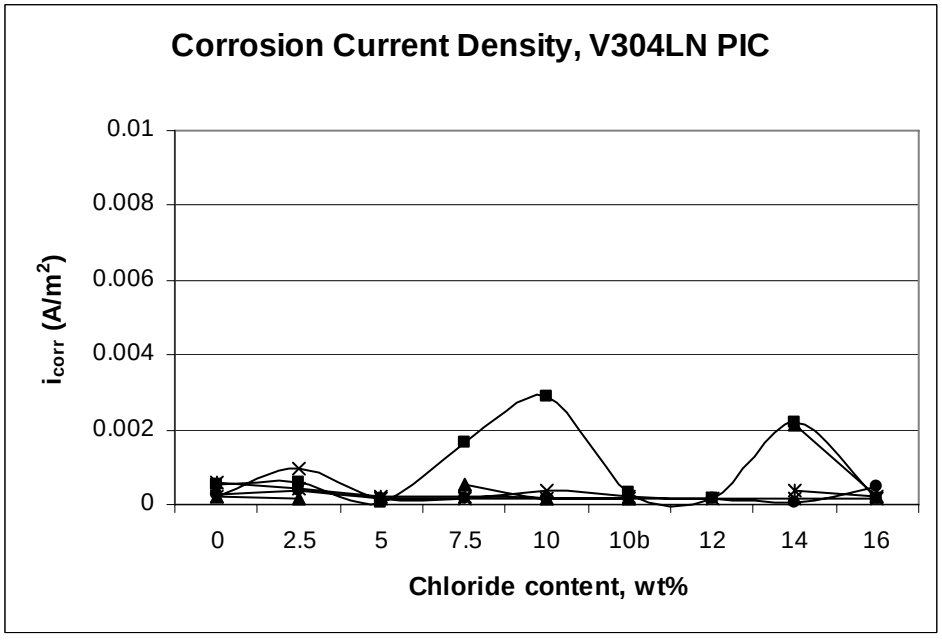
Corrosion Current Density, V304LN PIC
0.01
0.008
0.006
0.004
0.002
0
icorr (A/m2)
0
2.5
5
7.5
10
10b
12
14
16
Chloride content, wt%

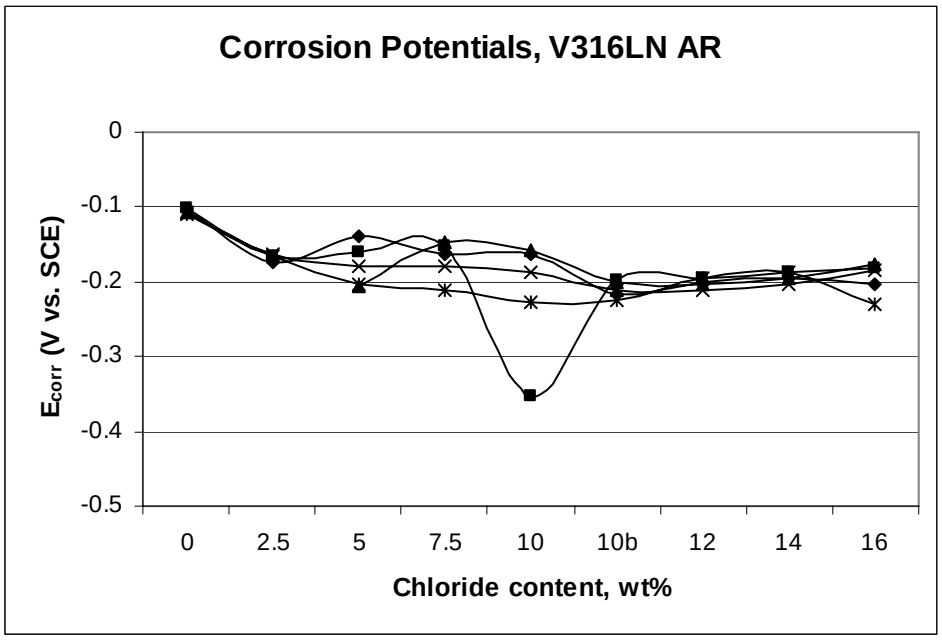
Corrosion Potentials, V316LN AR
0
-0.1
-0.2
-0.3
-0.4
-0.5
Ecorr (V vs. SCE)
0
2.5
5
7.5
10
10b
12
14
16
Chloride content, wt%

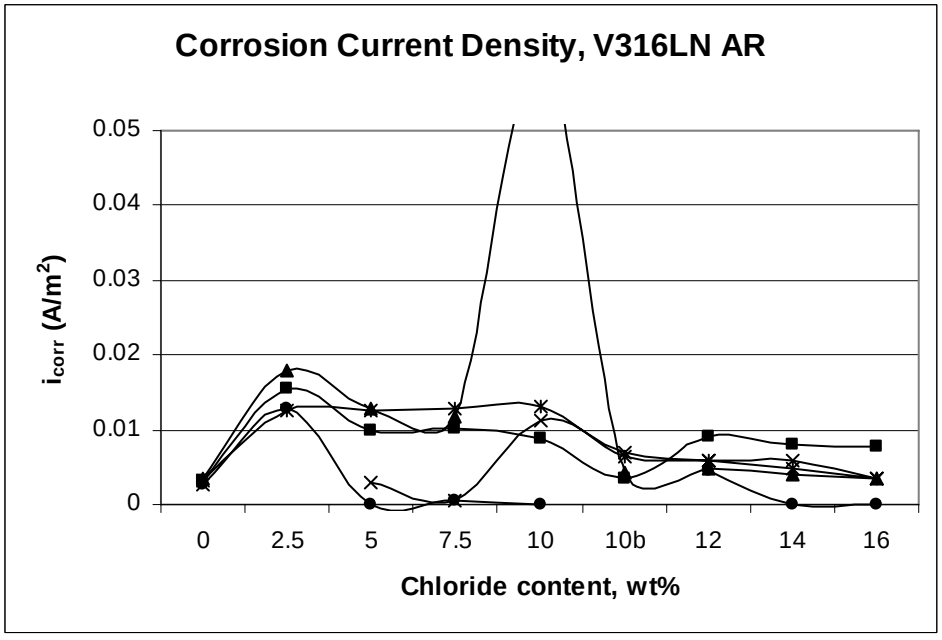
Corrosion Current Density, V316LN AR
0.05
0.04
0.03
0.02
0.01
0
icorr (A/m2)
0
2.5
5
7.5
10
10b
12
14
16
Chloride content, wt%

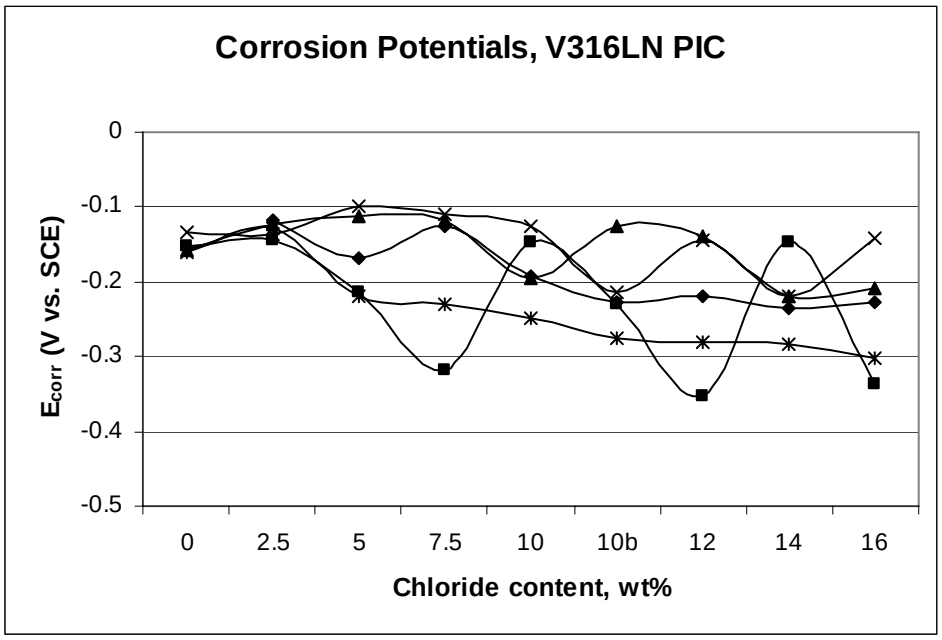
Corrosion Potentials, V316LN PIC
0
-0.1
-0.2
-0.3
-0.4
-0.5
Ecorr (V vs. SCE)
0
2.5
5
7.5
10
10b
12
14
16
Chloride content, wt%

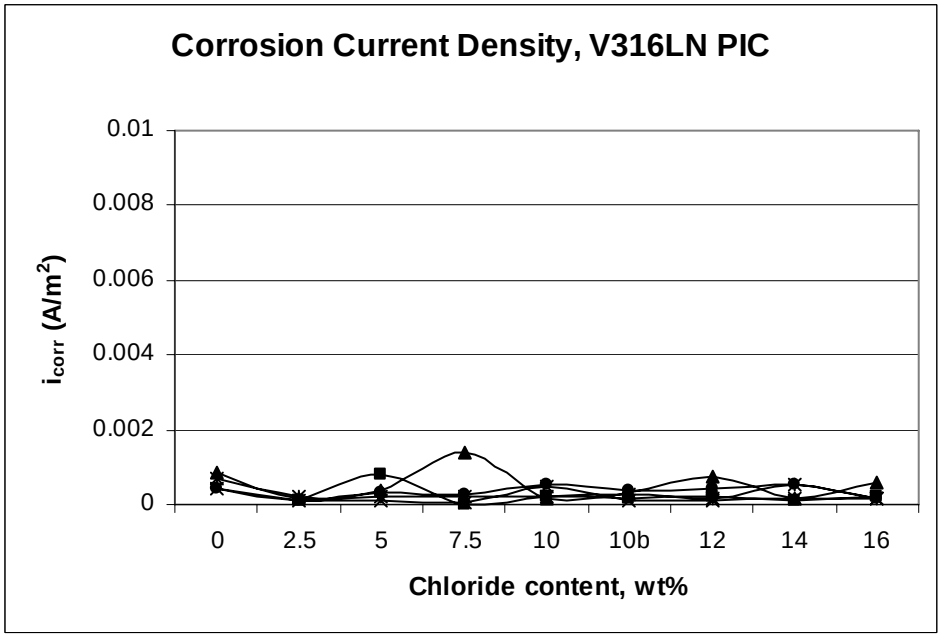
Corrosion Current Density, V316LN PIC
0.01
0.008
0.006
0.004
0.002
0
icorr (A/m2)
0
2.5
5
7.5
10
10b
12
14
16
Chloride content, wt%

Appendix D – Cyclic Polarization Scans of Steels in Pore Solution

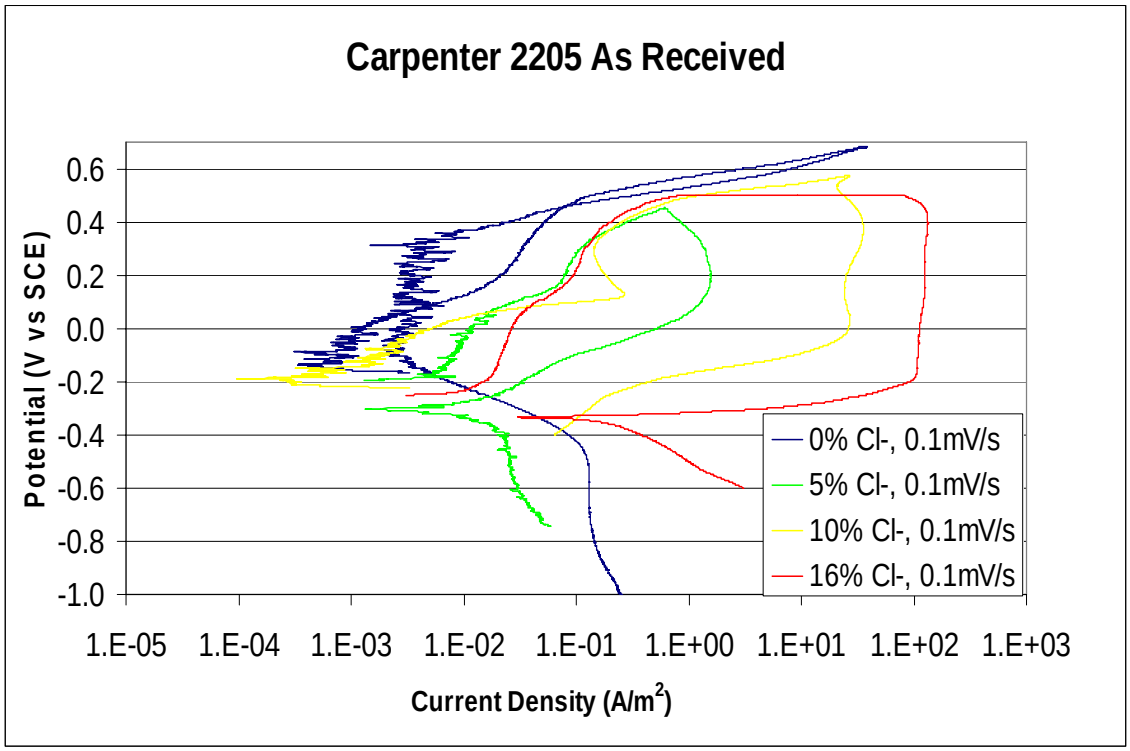
Carpenter 2205 As Received
Potential (V vs SCE)
0.6
0.4
0.2
0.0
-0.2
-0.4
-0.6
-0.8
-1.0
1.E-05
1.E-04
1.E-03
1.E-02
1.E-01
1.E+00
1.E+01
1.E+02
1.E+03
Current Density (A/m2)
0% Cl-, 0.1mV/s
5% Cl-, 0.1mV/s
10% Cl-, 0.1mV/s
16% Cl-, 0.1mV/s

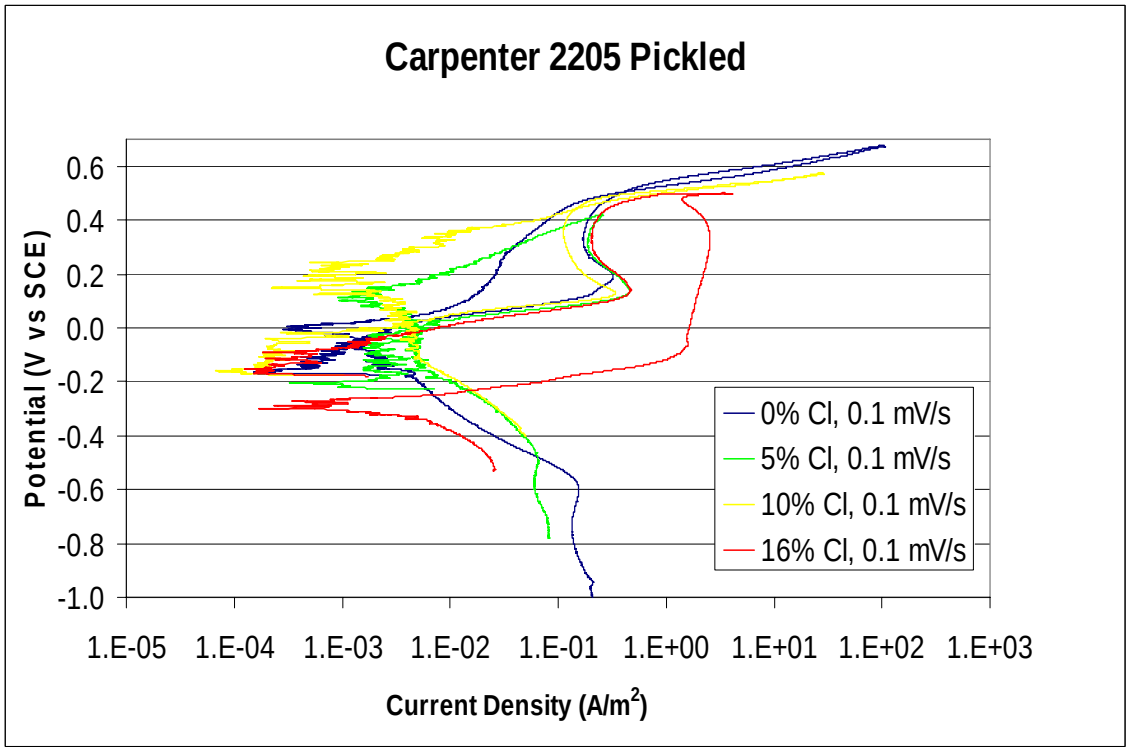
Carpenter 2205 Pickled
Potential (V vs SCE)
0.6
0.4
0.2
0.0
-0.2
-0.4
-0.6
-0.8
-1.0
1.E-05
1.E-04
1.E-03
1.E-02
1.E-01
1.E+00
1.E+01
1.E+02
1.E+03
Current Density (A/m2)
0% Cl, 0.1 mV/s
5% Cl, 0.1 mV/s
10% Cl, 0.1 mV/s
16% Cl, 0.1 mV/s

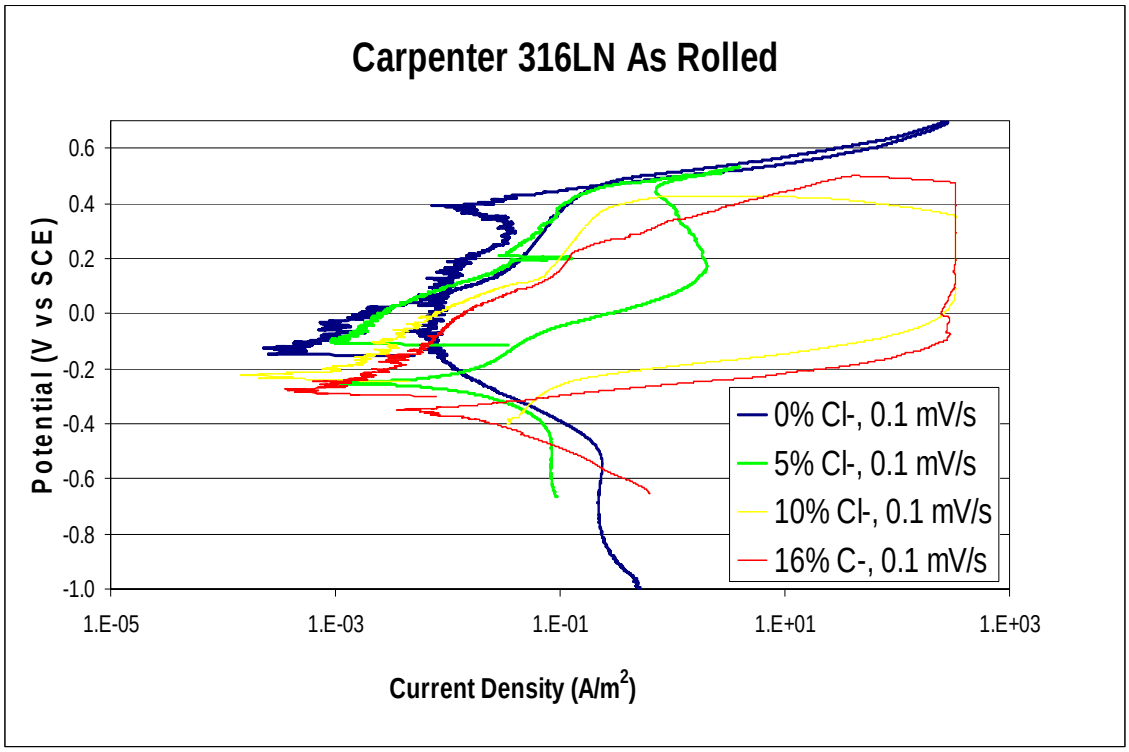
Carpenter 316LN As Rolled
Potential (V vs SCE)
0.6
0.4
0.2
0.0
-0.2
-0.4
-0.6
-0.8
-1.0
1.E-05
1.E-03
1.E-01
1.E+01
1.E+03
Current Density (A/m2)
0% Cl-, 0.1 mV/s
5% Cl-, 0.1 mV/s
10% Cl-, 0.1 mV/s
16% C-, 0.1 mV/s

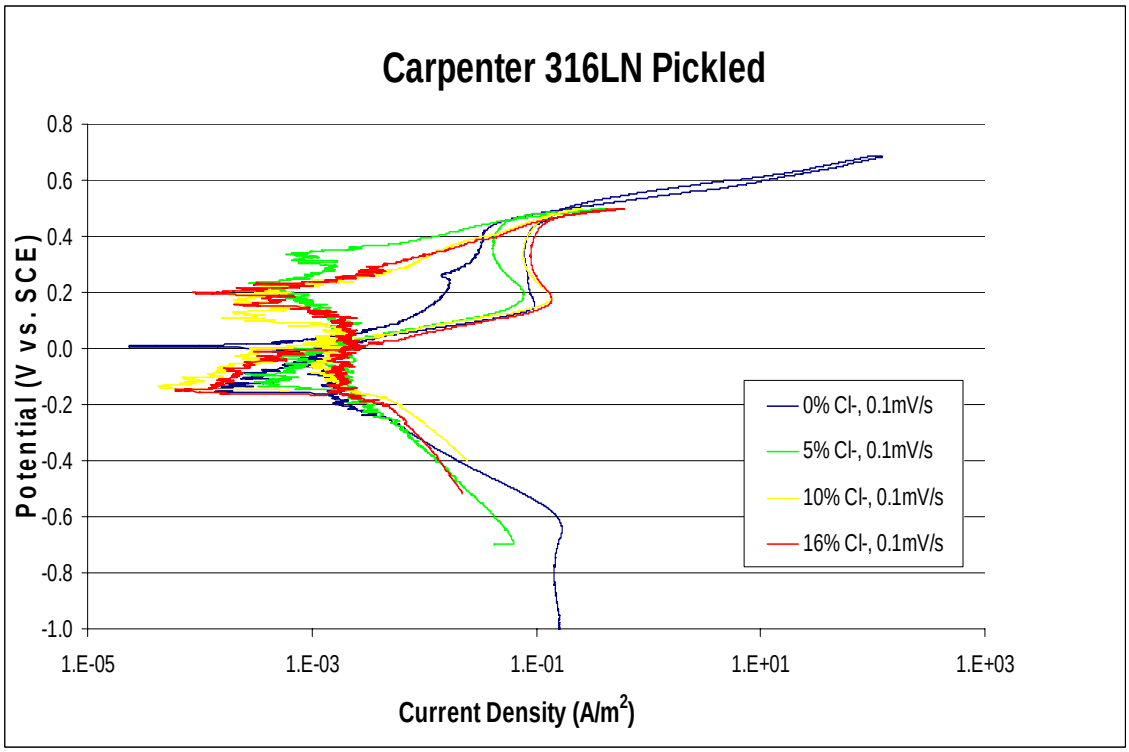
Carpenter 316LN Pickled
Potential (V vs. SCE)
0.8
0.6
0.4
0.2
0.0
-0.2
-0.4
-0.6
-0.8
-1.0
1.E-05
1.E-03
1.E-01
1.E+01
1.E+03
Current Density (A/m2)
0% Cl-, 0.1mV/s
5% Cl-, 0.1mV/s
10% Cl-, 0.1mV/s
16% Cl-, 0.1mV/s

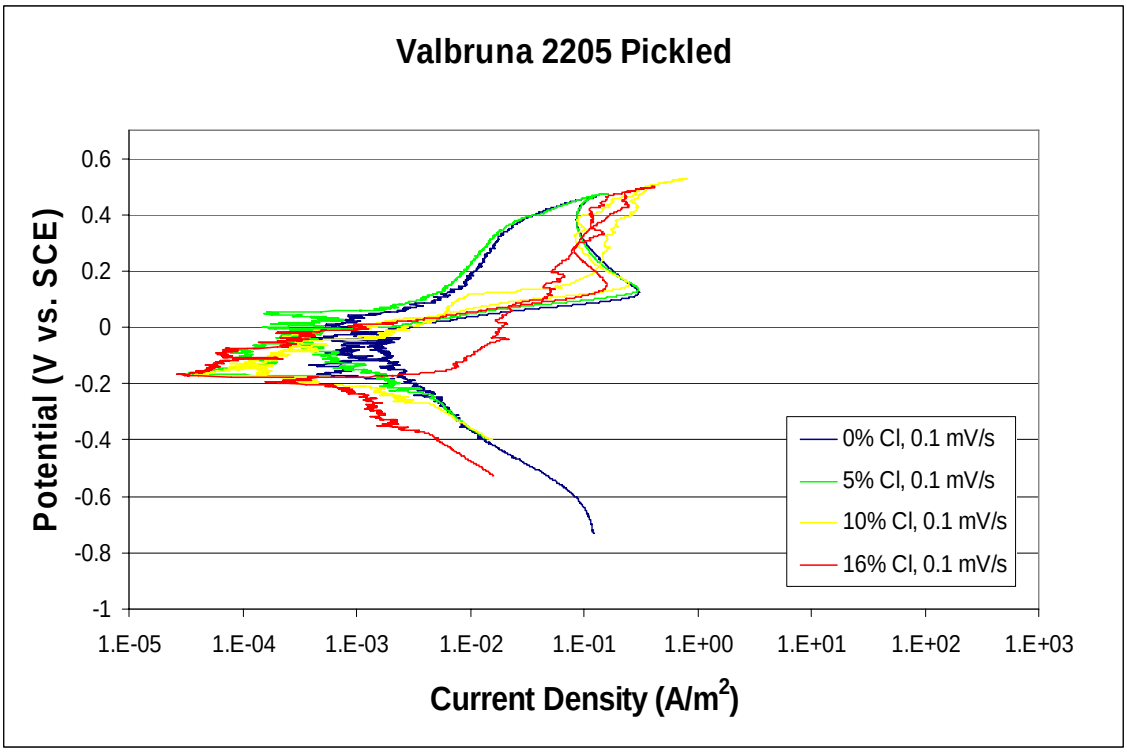
Valbruna 2205 Pickled
Potential (V vs. SCE)
0.6
0.4
0.2
0
-0.2
-0.4
-0.6
-0.8
-1
1.E-05
1.E-04
1.E-03
1.E-02
1.E-01
1.E+00
1.E+01
1.E+02
1.E+03
Current Density (A/m2)
0% Cl, 0.1 mV/s
5% Cl, 0.1 mV/s
10% Cl, 0.1 mV/s
16% Cl, 0.1 mV/s

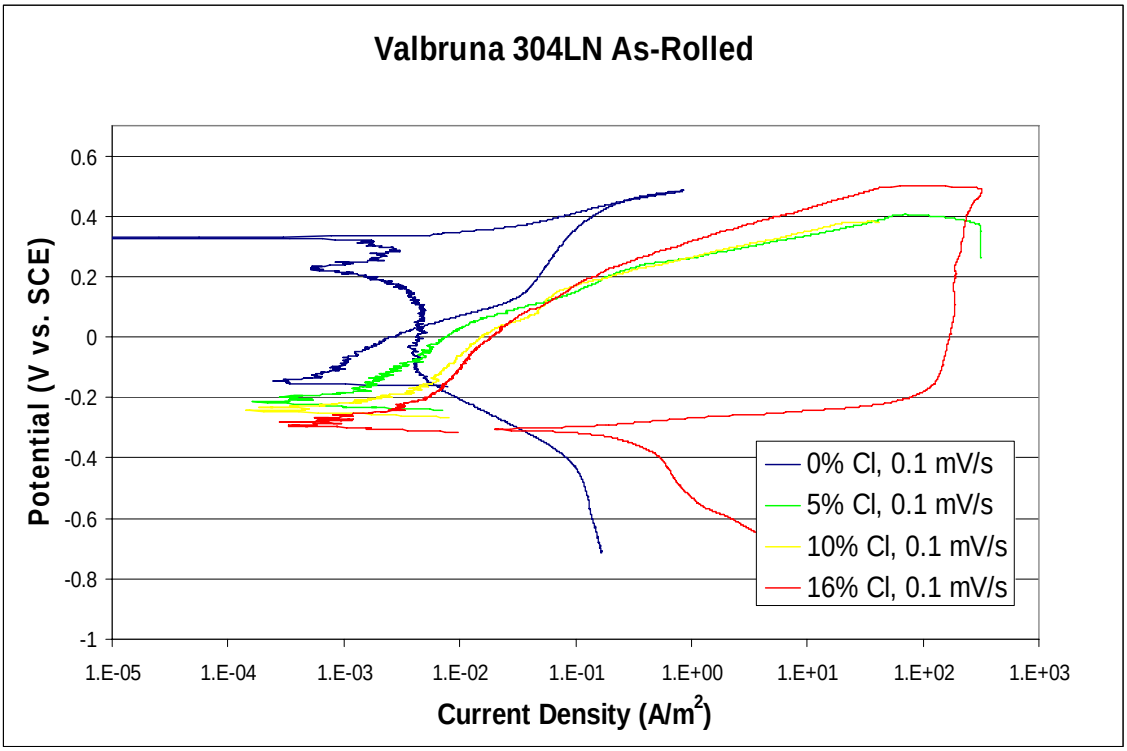
Valbruna 304LN As-Rolled
Potential (V vs. SCE)
0.6
0.4
0.2
0
-0.2
-0.4
-0.6
-0.8
-1
1.E-05
1.E-04
1.E-03
1.E-02
1.E-01
1.E+00
1.E+01
1.E+02
1.E+03
Current Density (A/m2)
0% Cl, 0.1 mV/s
5% Cl, 0.1 mV/s
10% Cl, 0.1 mV/s
16% Cl, 0.1 mV/s

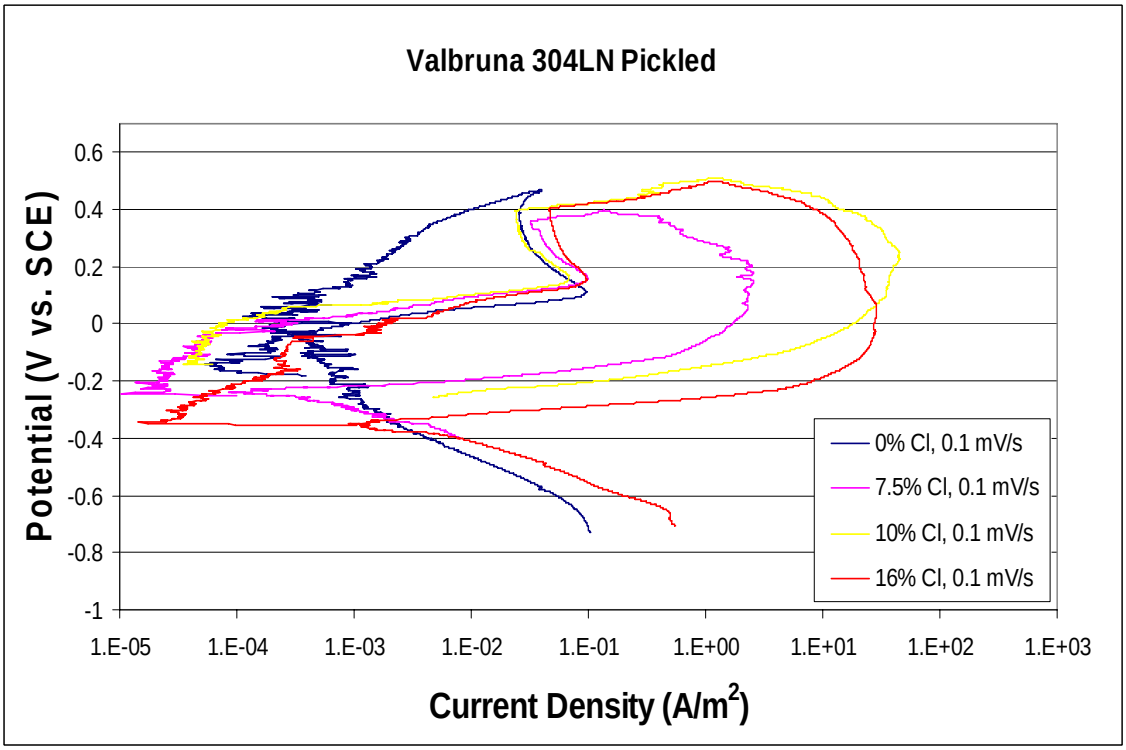
Valbruna 304LN Pickled
Potential (V vs. SCE)
0.6
0.4
0.2
0
-0.2
-0.4
-0.6
-0.8
-1
1.E-05
1.E-04
1.E-03
1.E-02
1.E-01
1.E+00
1.E+01
1.E+02
1.E+03
Current Density (A/m2)
0% Cl, 0.1 mV/s
7.5% Cl, 0.1 mV/s
10% Cl, 0.1 mV/s
16% Cl, 0.1 mV/s

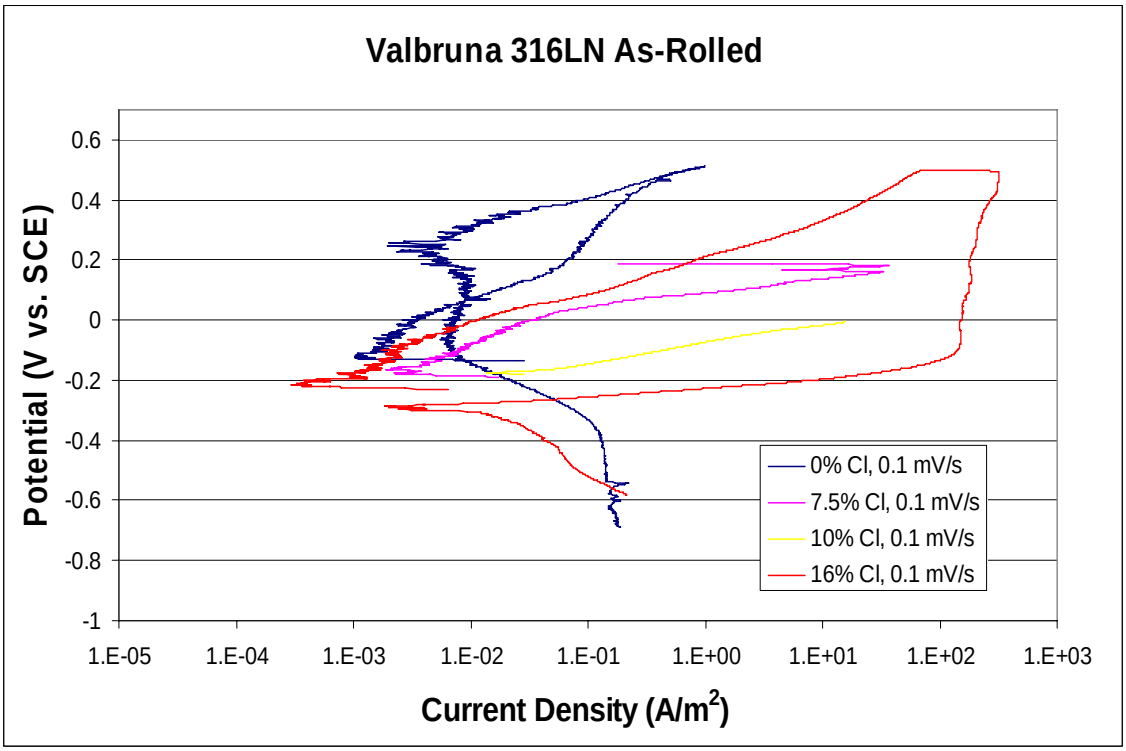
Valbruna 316LN As-Rolled
Potential (V vs. SCE)
0.6
0.4
0.2
0
-0.2
-0.4
-0.6
-0.8
-1
1.E-05
1.E-04
1.E-03
1.E-02
1.E-01
1.E+00
1.E+01
1.E+02
1.E+03
Current Density (A/m2)
0% Cl, 0.1 mV/s
7.5% Cl, 0.1 mV/s
10% Cl, 0.1 mV/s
16% Cl, 0.1 mV/s

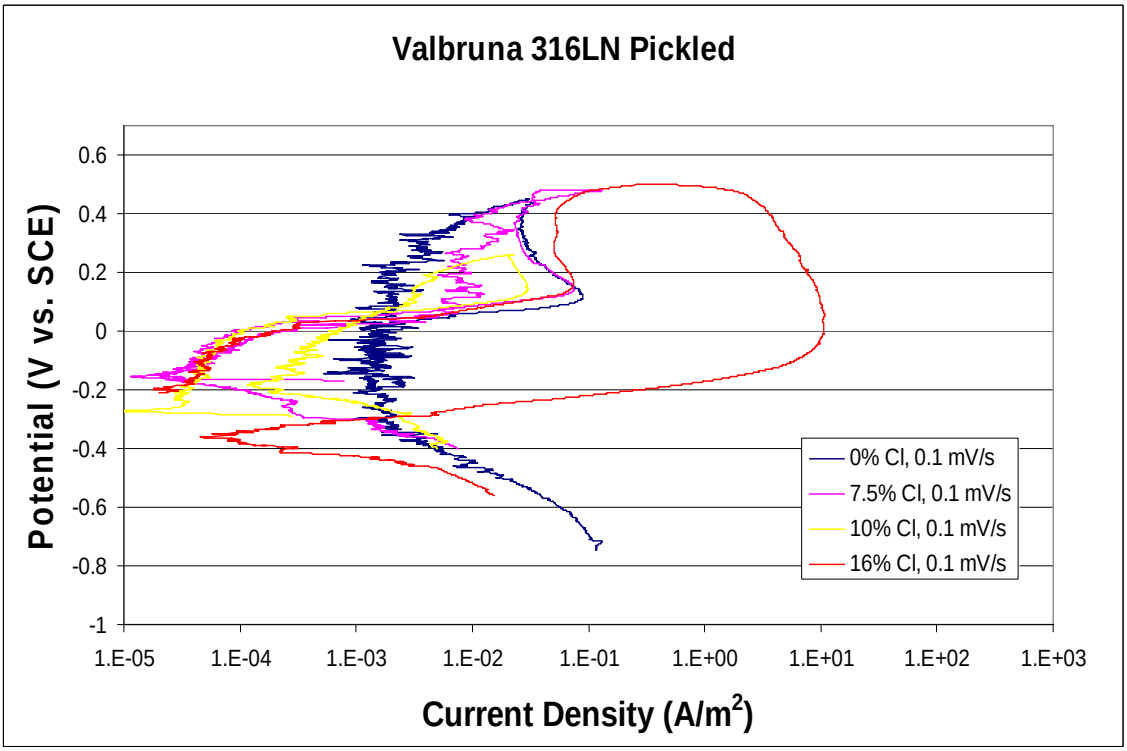
Valbruna 316LN Pickled
Potential (V vs. SCE)
0.6
0.4
0.2
0
-0.2
-0.4
-0.6
-0.8
-1
1.E-05
1.E-04
1.E-03
1.E-02
1.E-01
1.E+00
1.E+01
1.E+02
1.E+03
Current Density (A/m2)
0% Cl, 0.1 mV/s
7.5% Cl, 0.1 mV/s
10% Cl, 0.1 mV/s
16% Cl, 0.1 mV/s

Appendix E – Optical Microscopy of Stainless Steel Rebar

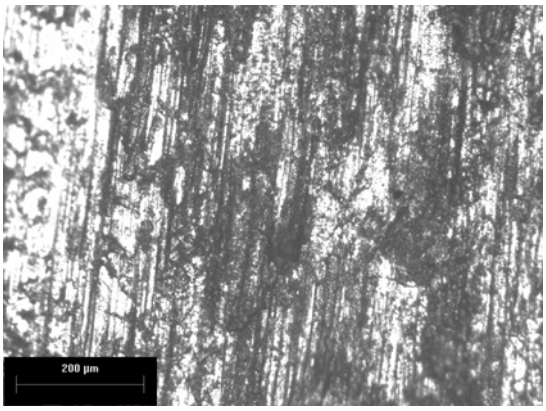

Figure E-1: Carpenter 2205 As-Rolled Surface, 100X

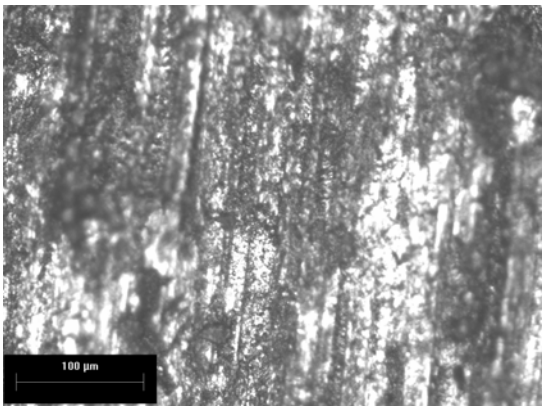

Figure E-2: Carpenter 2205 As-Rolled Surface, 200X

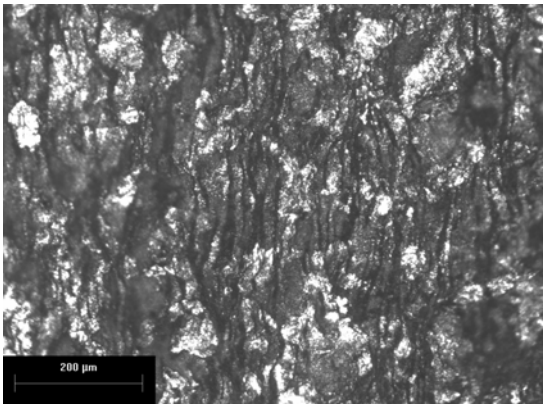

Figure E-3: Carpenter 2205 Pickled Surface, 100X

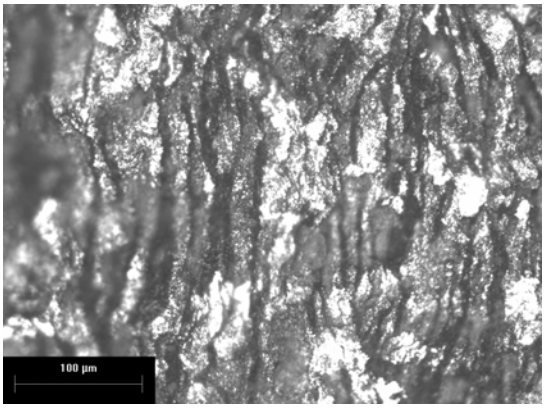

Figure E-4: Carpenter 2205 Pickled Surface, 200X

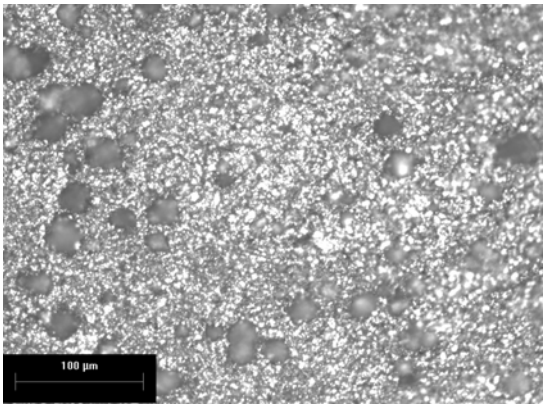

Figure E-5: Carpenter 2205 Cross-Section, Inner Structure, 200X

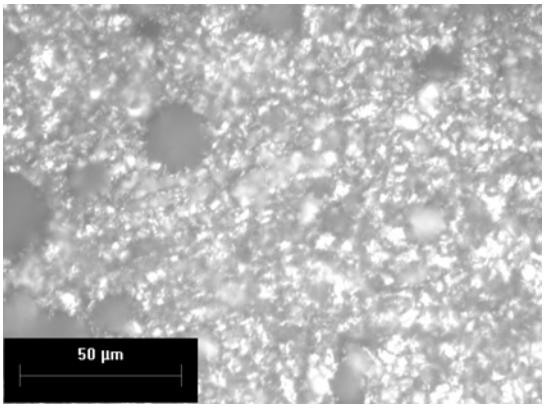

Figure E-6: Carpenter 2205 Cross-Section, Inner Structure, 500X

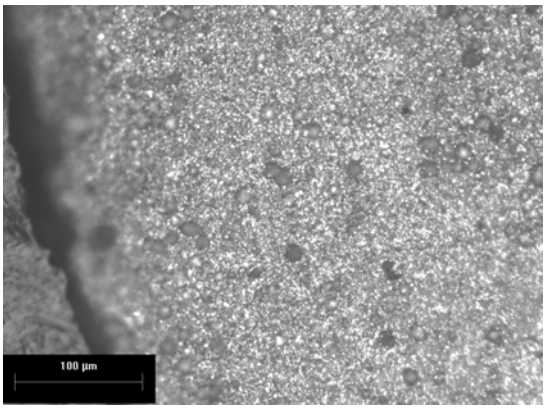

Figure E-7: Carpenter 2205 Cross-Section, Surface Structure, 200X

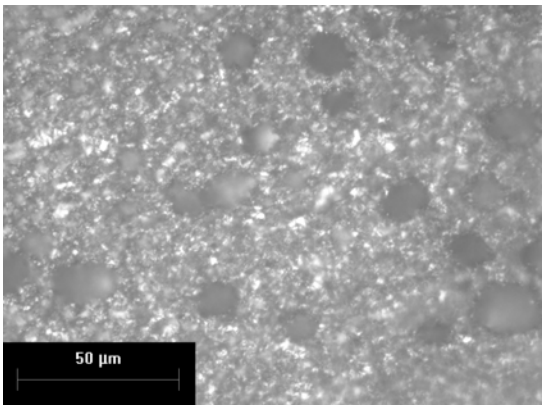

Figure E-8: Carpenter 2205 Cross-Section, Surface Structure, 500X

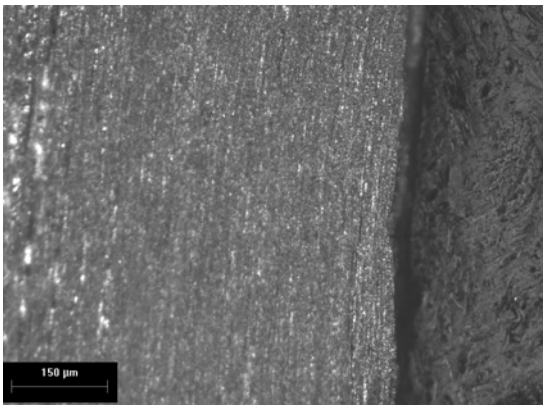

Figure E-9: Carpenter 2205 Longitudinal Section, Surface Structure, 100X

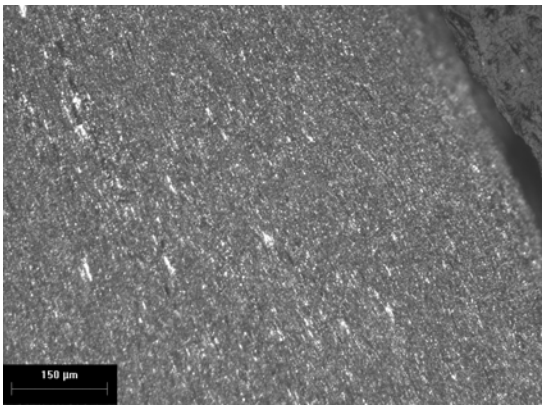

Figure E-10: Carpenter 2205 Longitudinal Section, Rib Structure, 100X

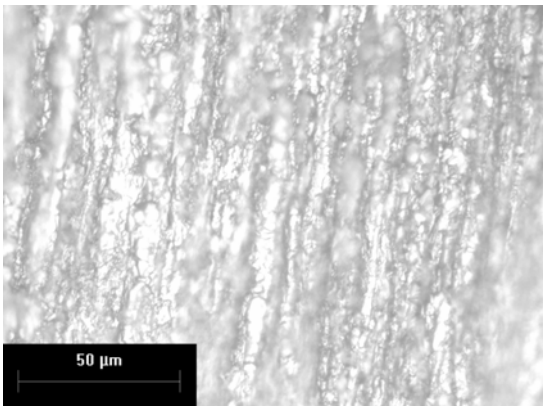

Figure E-11: Carpenter 2205 Longitudinal Section, Inner Structure, 500X

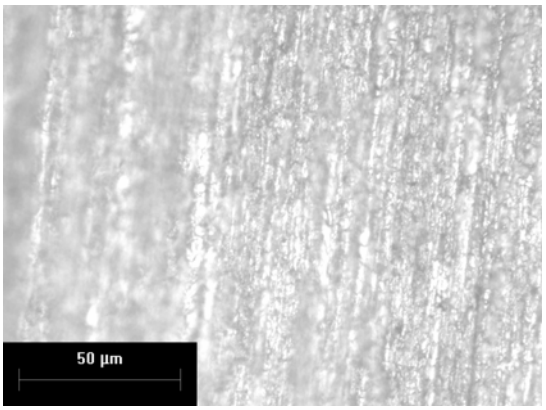

Figure E-12: Carpenter 2205 Longitudinal Section, Surface Structure, 500X

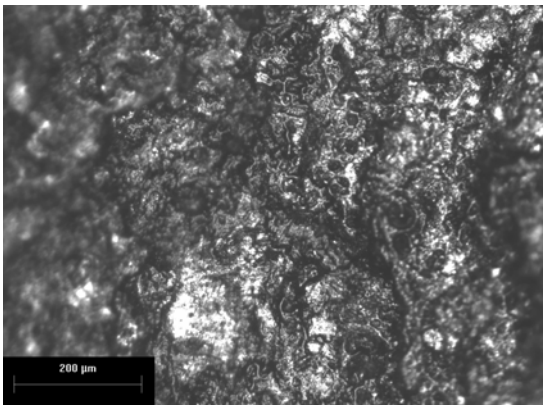

Figure E-13: Carpenter 316LN As-Rolled Surface, 100X

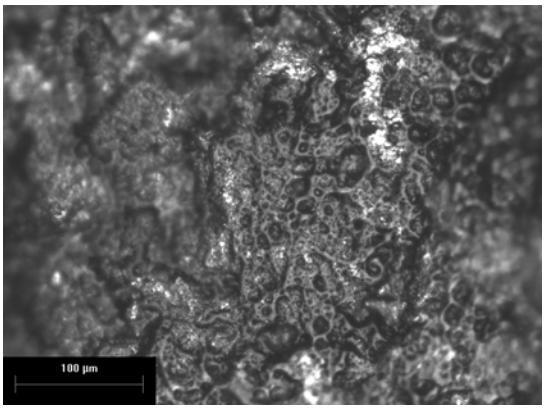

Figure E-14: Carpenter 316LN As-Rolled Surface, 200X

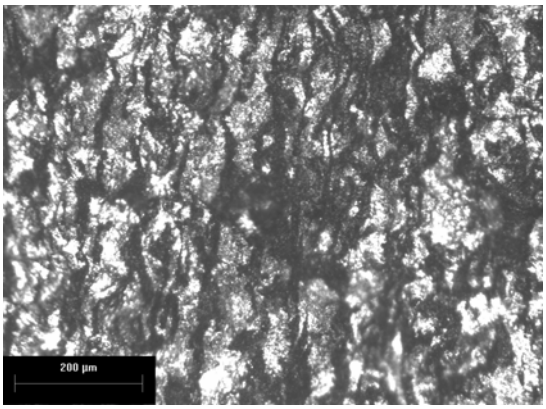

Figure E-15: Carpenter 316LN Pickled Surface, 100X

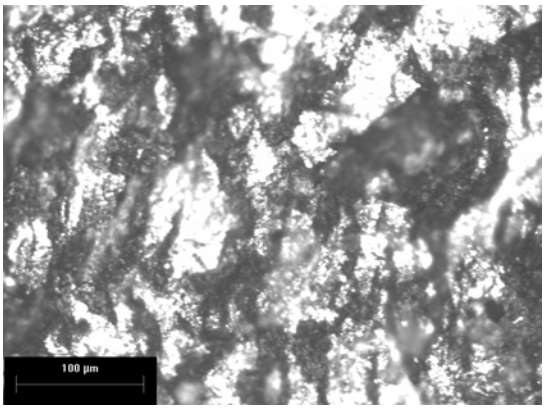

Figure E-16: Carpenter 316LN Pickled Surface, 200X

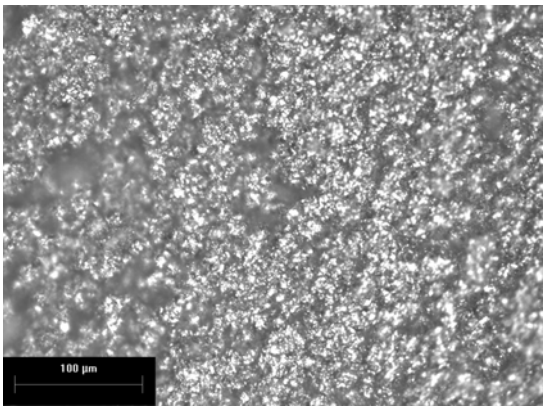

Figure E-17: Carpenter 316LN Cross-Section, Inner Structure, 200X

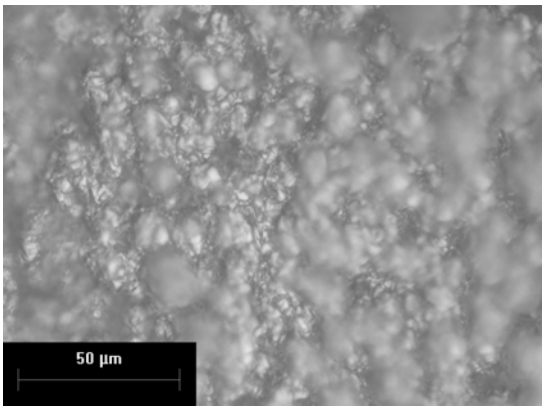

Figure E-18: Carpenter 316LN Cross-Section, Inner Structure, 500X

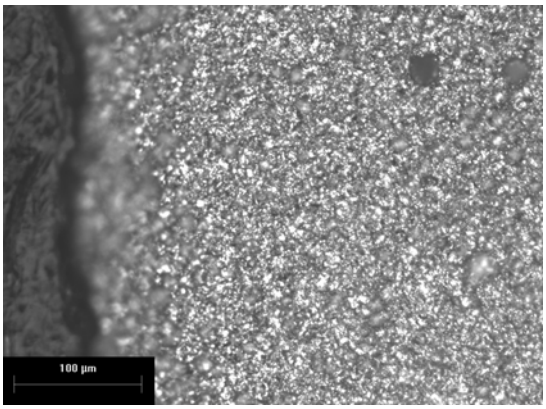

Figure E-19: Carpenter 316LN Cross-Section, Surface Structure, 200X

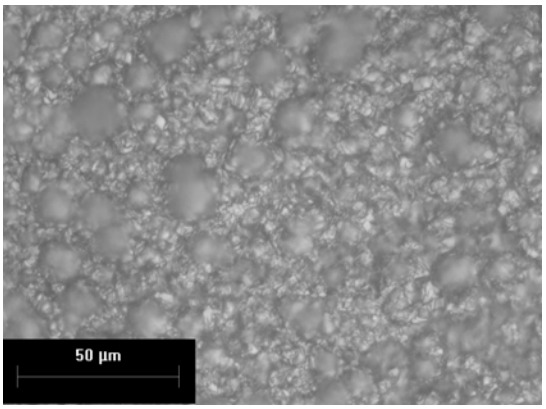

Figure E-20: Carpenter 316LN Cross-Section, Surface Structure, 500X

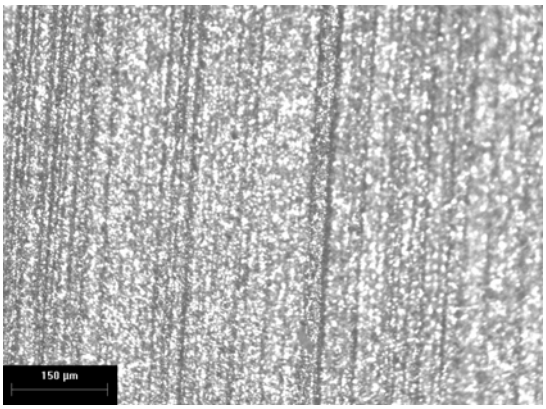

Figure E-21: Carpenter 316LN Longitudinal Section, Inner Structure, 100X

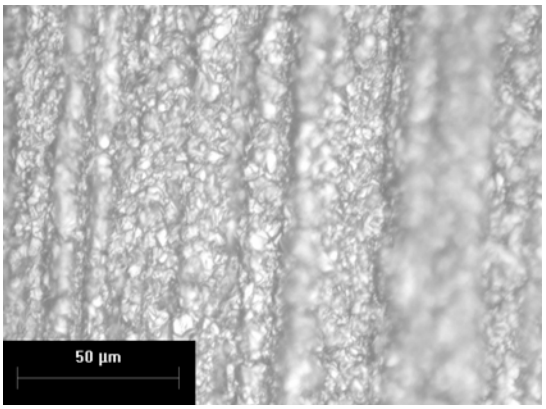

Figure E-22: Carpenter 316LN Longitudinal Section, Inner Structure, 500X

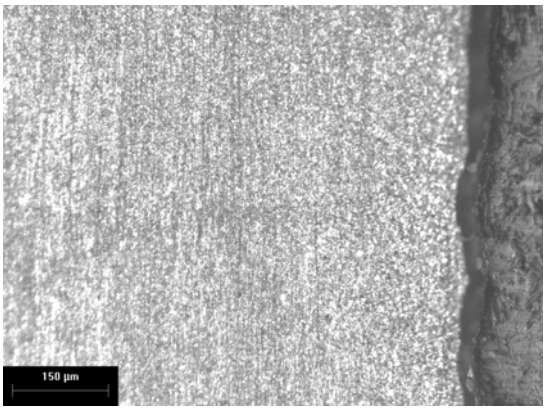

Figure E-23: Carpenter 316LN Longitudinal Section, Surface Structure, 100X

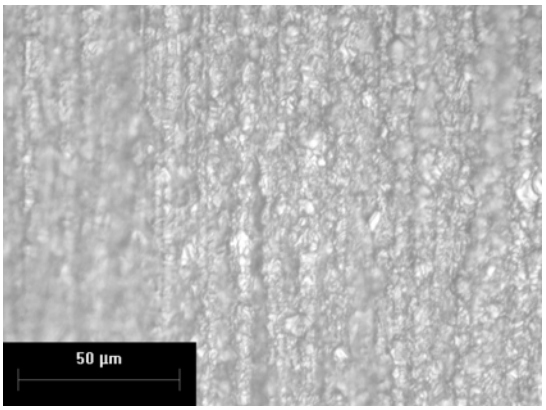

Figure E-24: Carpenter 316LN Longitudinal Section, Surface Structure, 500X

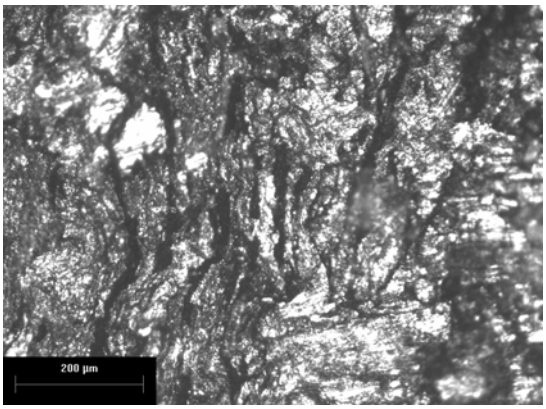

Figure E-25: Valbruna 2205 Pickled Surface, 100X

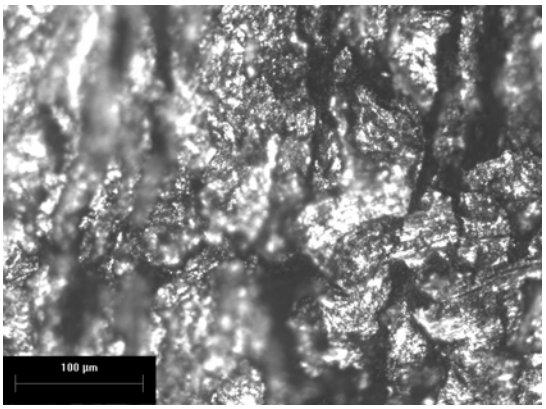

Figure E-26: Valbruna 2205 Pickled Surface, 200X

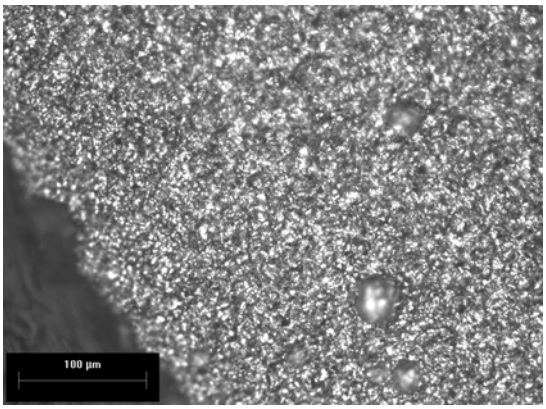

Figure E-27: Valbruna 2205 Pickled Cross-Section, 200X

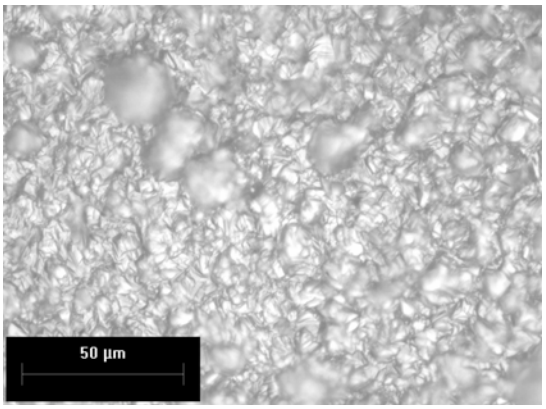

Figure E-28: Valbruna 2205 Pickled Cross-Section, 500X

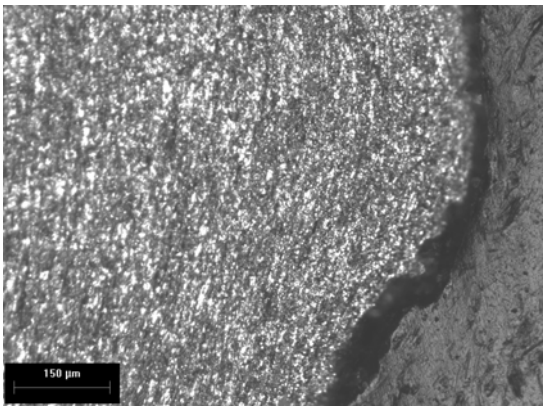

Figure E-29: Valbruna 2205 Pickled Longitudinal Section, 100X

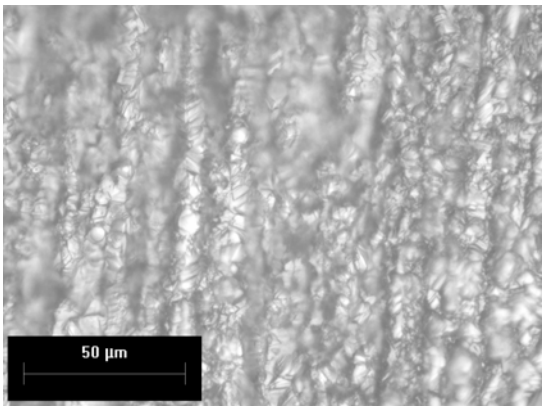

Figure E-30: Valbruna 2205 Pickled Longitudinal Section, 500X

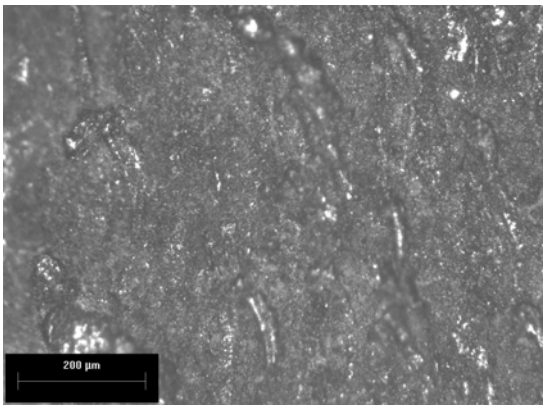

Figure E-31: Valbruna 304LN As-Rolled Surface, 100X

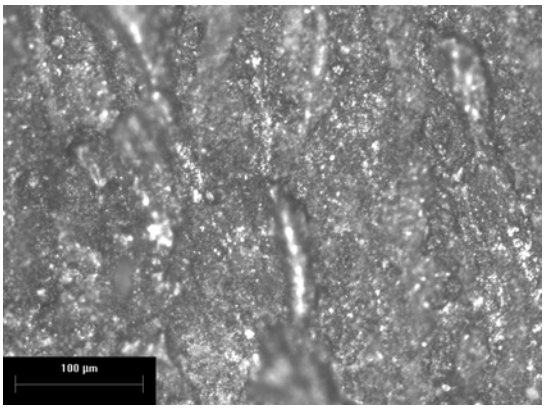

Figure E-32: Valbruna 304LN As-Rolled Surface, 200X

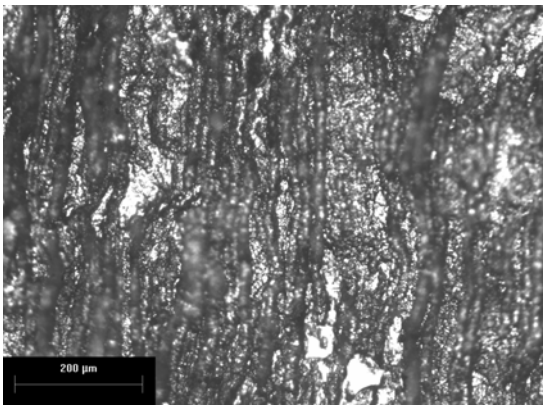

Figure E-33: Valbruna 304LN Pickled Surface, 100X

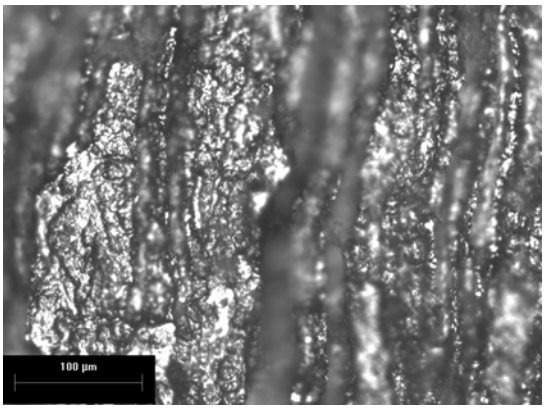

Figure E-34: Valbruna 304LN Pickled Surface, 200X

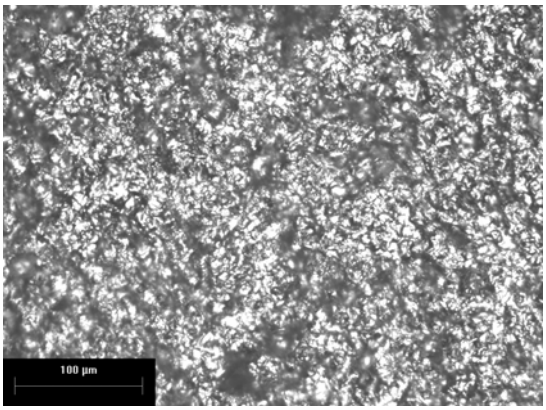

Figure E-35: Valbruna 304LN Cross-Section, Inner Structure, 200X

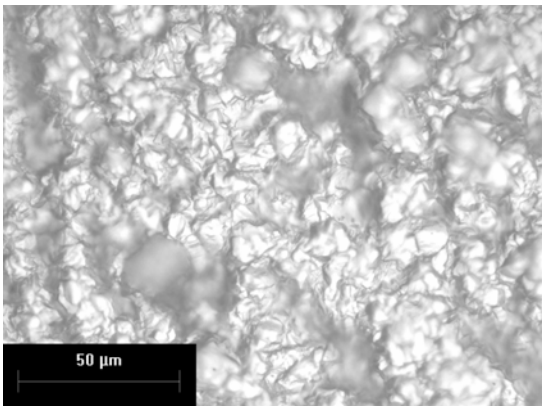

Figure E-36: Valbruna 304LN Cross-Section, Inner Structure, 500X

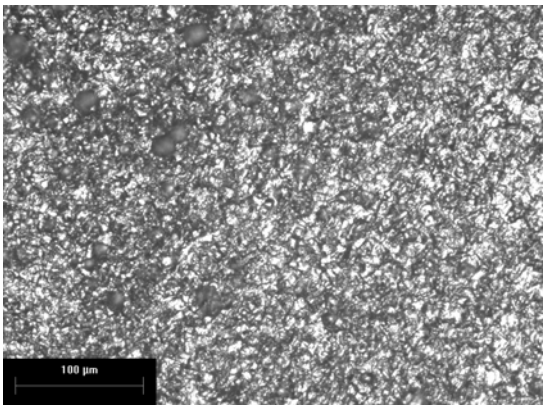

Figure E-37: Valbruna 304LN Cross-Section, Surface Structure, 200X

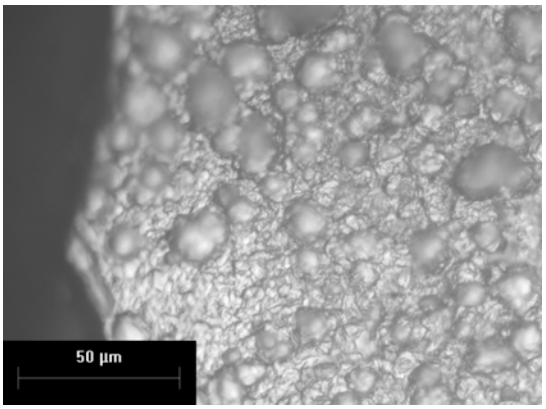

Figure E-38: Valbruna 304LN Cross-Section, Surface Structure, 500X

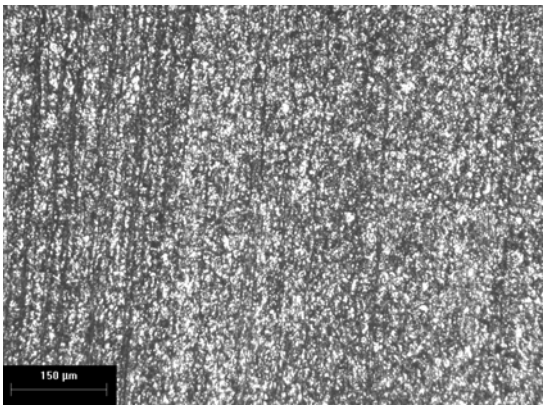

Figure E-39: Valbruna 304LN Longitudinal Section, Inner Structure, 100X

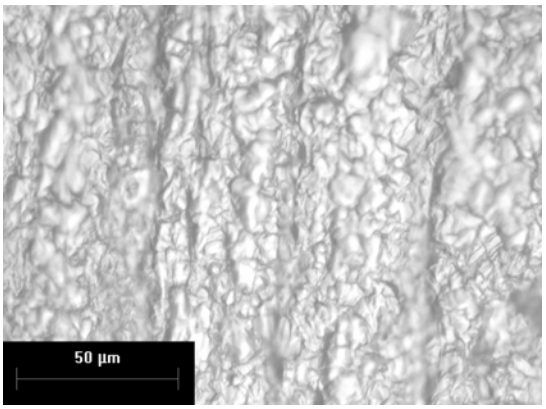

Figure E-40: Valbruna 304LN Longitudinal Section, Inner Structure, 500X

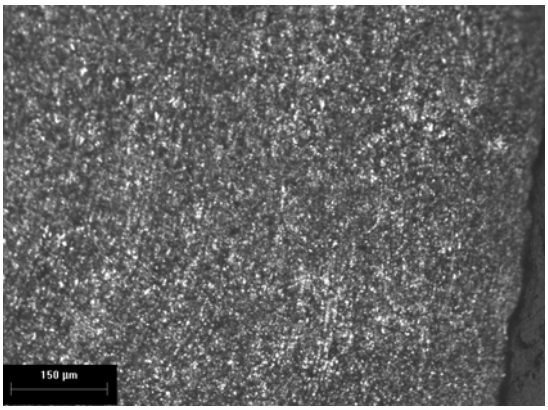

Figure E-41: Valbruna 304LN Longitudinal Section, Surface Structure, 100X

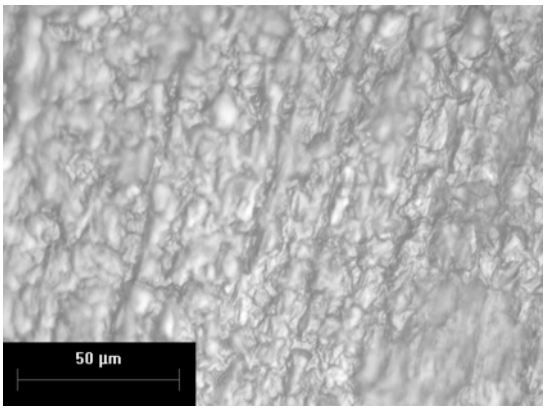

Figure E-42: Valbruna 304LN Longitudinal Section, Surface Structure, 500X

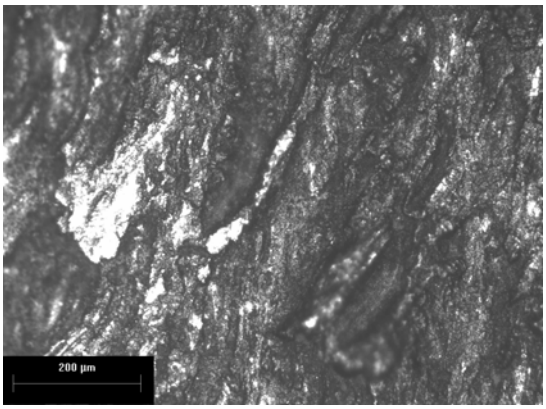

Figure E-43: Valbruna 316LN **20M** As-Rolled Surface, 100X

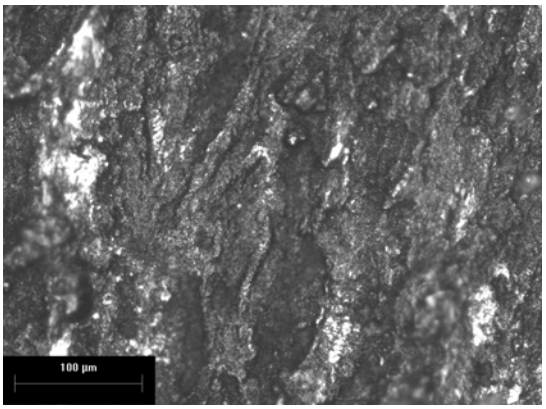

Figure E-44: Valbruna 316LN **20M** As-Rolled Surface, 200X

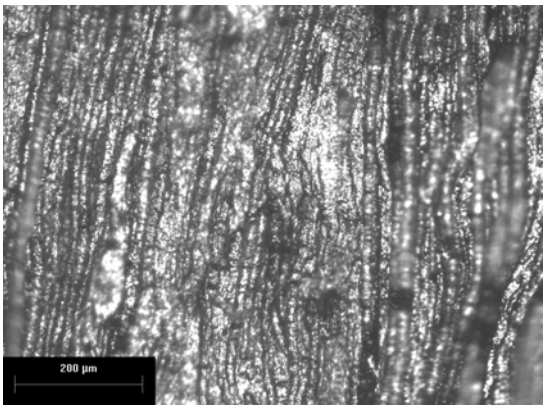

Figure E-45: Valbruna 316LN **15M** Pickled Surface, 100X

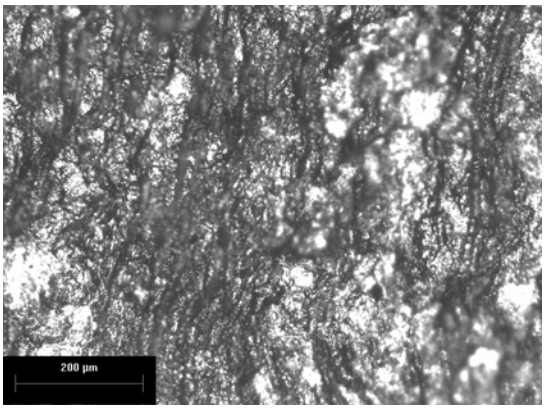

Figure E-46: Valbruna 316LN **20M** Pickled Surface, 100X

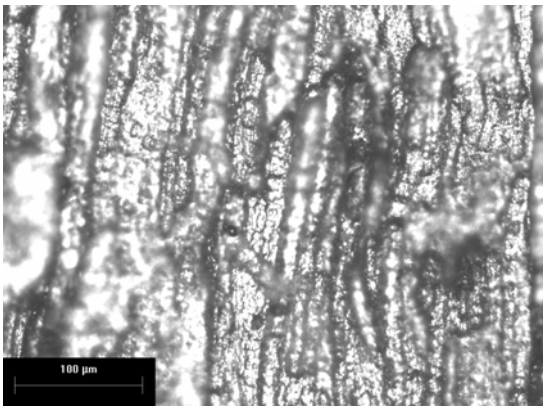

Figure E-47: Valbruna 316LN **15M** Pickled Surface, 200X

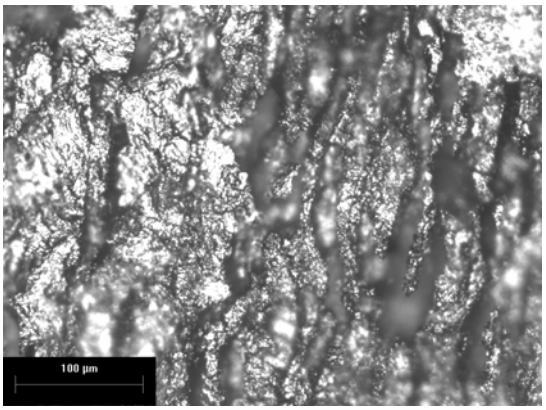

Figure E-48: Valbruna 316LN **20M** Pickled Surface, 200X

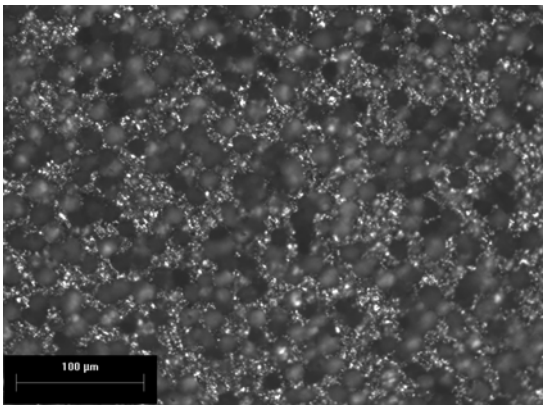

Figure E-49: Valbruna 316LN **15M** Cross-Section, Inner Structure, 200X

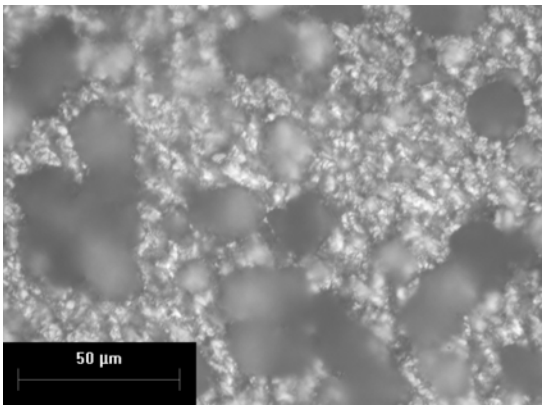

Figure E-50: Valbruna 316LN **15M** Cross-Section, Inner Structure, 500X

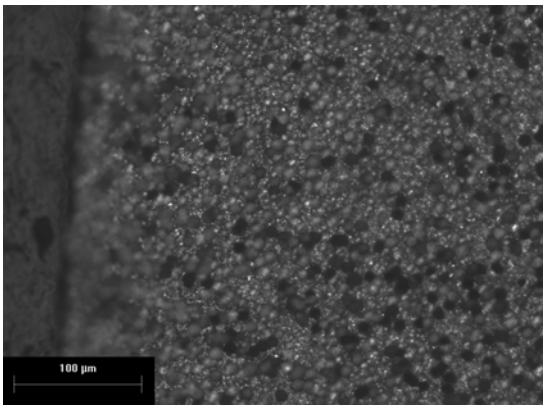

Figure E-51: Valbruna 316LN **15M** Cross-Section, Surface Structure, 200X

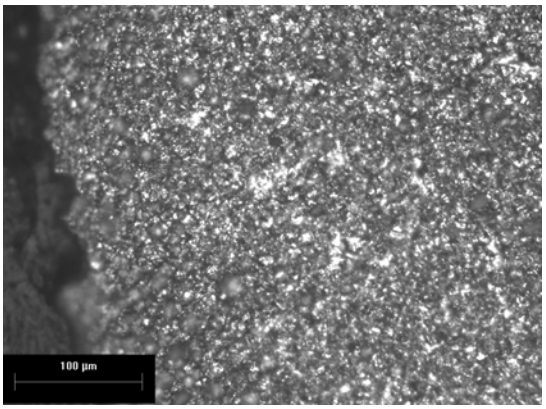

Figure E-52: Valbruna 316LN **20M** Cross-Section, 200X

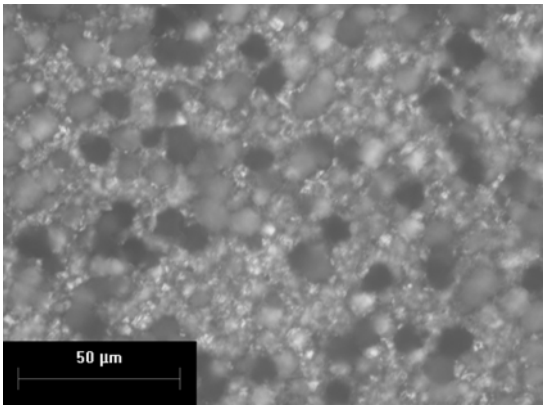

Figure E-53: Valbruna 316LN **15M** Cross-Section, Surface Structure, 500X

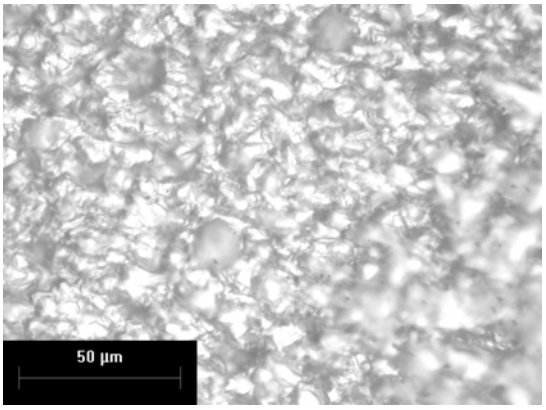

Figure E-54: Valbruna 316LN **20M** Cross-Section, 500X

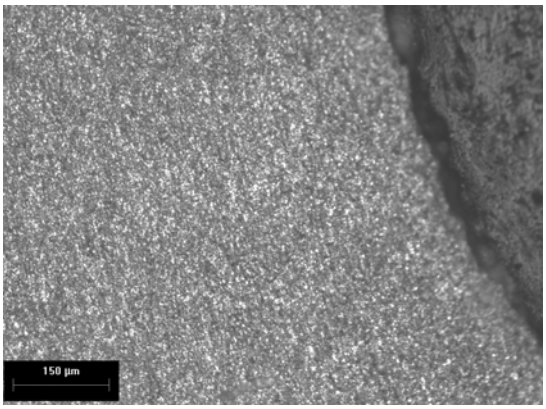

Figure E-55: Valbruna 316LN **15M** Longitudinal Section, Rib Structure, 100X

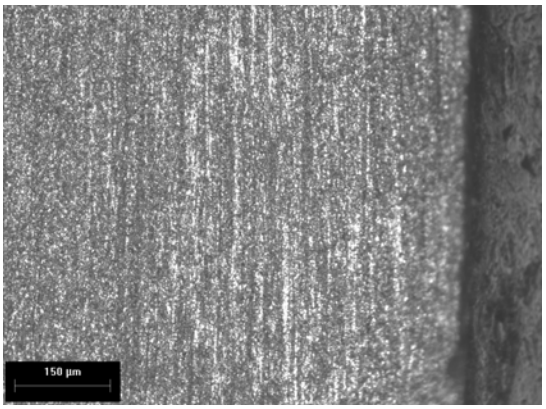

Figure E-56: Valbruna 316LN **15M** Longitudinal Section, Surface Structure, 100X

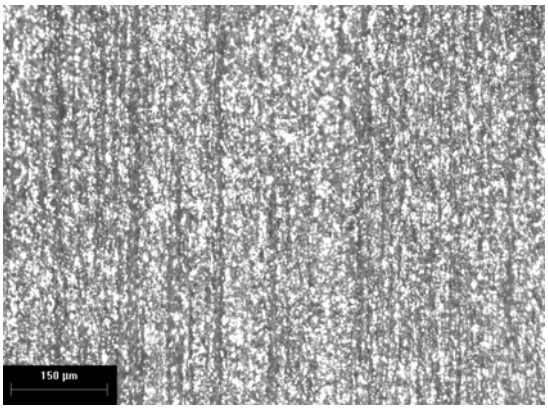

Figure E-57: Valbruna 316LN **20M** Longitudinal Section, Inner Structure, 100X

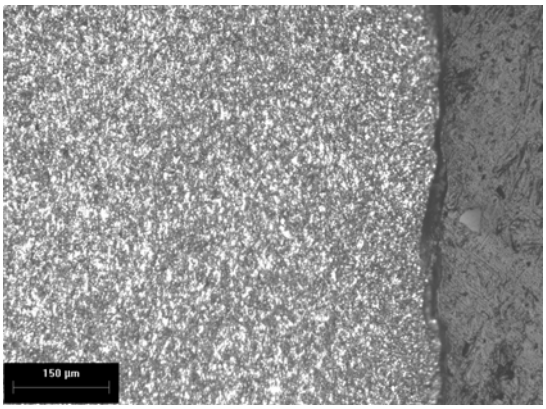

Figure E-58: Valbruna 316LN **20M** Longitudinal Section, Surface Structure, 100X

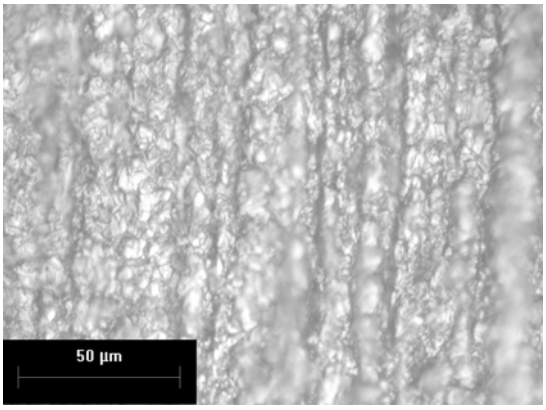

Figure E-59: Valbruna 316LN **15M** Longitudinal Section, Inner Structure, 500X

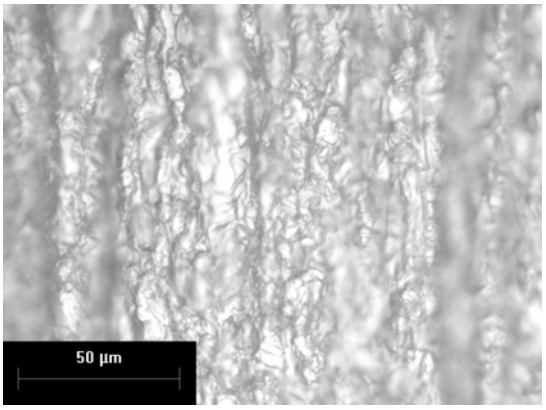

Figure E-60: Valbruna 316LN **20M** Longitudinal Section, Inner Structure, 500X

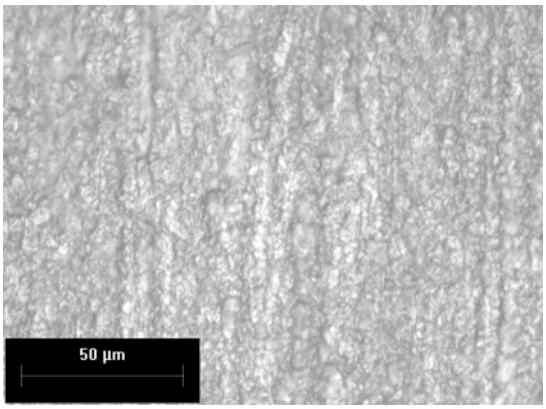

Figure E-61: Valbruna 316LN **15M** Longitudinal Section, Surface Structure, 500X

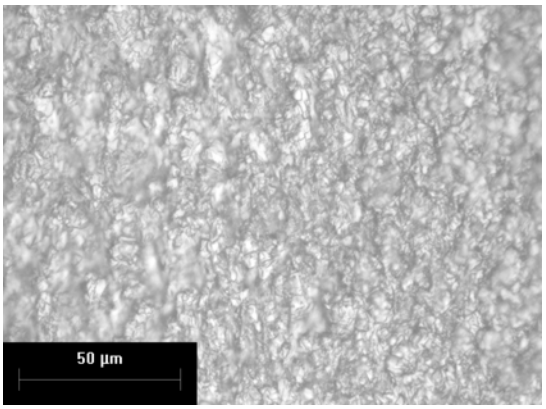

Figure E-62: Valbruna 316LN **20M** Longitudinal Section, Surface Structure, 500X